

**A computational analysis of wind turbine and wind farm aerodynamics with a  
focus on dual rotor wind turbines**

by

**Aaron John Rosenberg**

A dissertation submitted to the graduate faculty  
in partial fulfillment of the requirements for the degree of  
DOCTOR OF PHILOSOPHY

Majors: Aerospace Engineering  
Wind Energy Science, Engineering and Policy

Program of Study Committee:  
Anupam Sharma, Major Professor  
Partha Sarkar  
Eugene Takle  
Hui Hu  
Baskar Ganapathysubramanian

Iowa State University

Ames, Iowa

2016

Copyright © Aaron John Rosenberg, 2016. All rights reserved.

## TABLE OF CONTENTS

<b>LIST OF TABLES</b> . . . . .	<a href="#">v</a>
<b>LIST OF FIGURES</b> . . . . .	<a href="#">v</a>
<b>ACKNOWLEDGEMENTS</b> . . . . .	<a href="#">x</a>
<b>ABSTRACT</b> . . . . .	<a href="#">xi</a>
<b>CHAPTER 1. WIND TURBINE AERODYNAMICS AND PERFORMANCE</b>	<a href="#">1</a>
1.1 Introduction . . . . .	<a href="#">1</a>
1.2 Analytical & Semi-analytical Methods . . . . .	<a href="#">2</a>
1.2.1 1-D Momentum Theory . . . . .	<a href="#">2</a>
1.2.2 Momentum Theory with Swirl . . . . .	<a href="#">5</a>
1.2.3 Blade Element Momentum Theory . . . . .	<a href="#">8</a>
1.2.4 Vortex Lattice Method . . . . .	<a href="#">10</a>
1.3 Computational Methods . . . . .	<a href="#">11</a>
1.3.1 RANS + Actuator Disk . . . . .	<a href="#">12</a>
1.3.2 LES + Actuator Line . . . . .	<a href="#">13</a>
1.3.3 Blade Resolved Simulations . . . . .	<a href="#">15</a>
1.4 Experimental Methods . . . . .	<a href="#">16</a>
1.5 Modern HAWT Performance . . . . .	<a href="#">17</a>
1.5.1 Swirl Loss . . . . .	<a href="#">17</a>
1.5.2 Induction Loss . . . . .	<a href="#">17</a>
1.5.3 Viscous Loss . . . . .	<a href="#">17</a>
1.5.4 Constraints . . . . .	<a href="#">18</a>
1.5.5 Wake Loss . . . . .	<a href="#">18</a>
1.6 Conclusion . . . . .	<a href="#">19</a>

<b>CHAPTER 2. A NOVEL DUAL-ROTOR TURBINE FOR INCREASED</b>	
<b>WIND ENERGY CAPTURE . . . . .</b>	<b>21</b>
2.1 Introduction . . . . .	22
2.2 Numerical Methods . . . . .	25
2.2.1 Rotor Parameterization using Actuator Disk/Line/Surface Models . . . .	26
2.2.2 Reynolds Averaged Navier Stokes (RANS) Simulations . . . . .	26
2.2.3 Large Eddy Simulations . . . . .	27
2.3 Dual-Rotor Simulations . . . . .	28
2.3.1 Rotor Design . . . . .	30
2.3.2 Optimization Study . . . . .	31
2.3.3 Large Eddy Simulations . . . . .	32
2.4 Momentum Entrainment with Atmospheric Boundary Layer . . . . .	35
2.4.1 Computational Setup . . . . .	35
2.4.2 Momentum Entrainment . . . . .	39
2.5 Conclusions . . . . .	41
<b>CHAPTER 3. A PRESCRIBED-WAKE VORTEX LATTICE METHOD</b>	
<b>FOR PRELIMINARY DESIGN OF CO-AXIAL, DUAL-ROTOR WIND</b>	
<b>TURBINES . . . . .</b>	<b>45</b>
3.1 Introduction . . . . .	46
3.2 Vortex Lattice Method . . . . .	46
3.2.1 Algorithm . . . . .	50
3.2.2 Validation . . . . .	51
3.3 Extension to Dual-Rotor Wind Turbines . . . . .	53
3.3.1 Verification with CFD . . . . .	57
3.4 Preliminary Design of a Dual-Rotor Wind Turbine . . . . .	61
3.5 Conclusion . . . . .	62

<b>CHAPTER 4. EXPLORING SURFACE FLOW CONVERGENCE INDUCED BY TIGHTLY-SPACED WIND TURBINES USING LARGE-EDDY SIM- ULATION . . . . .</b>	<b>65</b>
4.1 Introduction . . . . .	66
4.2 Computational Model . . . . .	67
4.2.1 Validation of Actuator Disk Model . . . . .	68
4.3 Wind Farm Simulations . . . . .	70
4.3.1 Finite Wind Farm in Uniform Flow . . . . .	70
4.3.2 Semi-infinite Wind Farm . . . . .	71
4.4 Results . . . . .	72
4.4.1 Finite Wind Farm . . . . .	72
4.4.2 Semi-infinite Wind Farm . . . . .	72
4.5 Conclusion . . . . .	73
4.6 Acknowledgements . . . . .	74
<b>CHAPTER 5. CONCLUSION . . . . .</b>	<b>76</b>
<b>APPENDIX A. COORDINATE SYSTEMS . . . . .</b>	<b>78</b>
<b>APPENDIX B. STREAMWISE TURBULENT MOMENTUM AND EN- ERGY FLUX . . . . .</b>	<b>79</b>
<b>BIBLIOGRAPHY . . . . .</b>	<b>80</b>



## LIST OF FIGURES

Figure 1.1	Illustration of a 1-D Streamtube [1] . . . . .	2
Figure 1.2	$C_P$ and $C_T$ as a function of axial induction factor, $a$ . . . . .	4
Figure 1.3	Illustration of a rotating actuator disk . . . . .	5
Figure 1.4	Flow velocity at a rotating element . . . . .	6
Figure 1.5	Optimum $a$ and $a'$ with respect to $\lambda$ [1] . . . . .	8
Figure 1.6	$C_P$ vs $\lambda$ [1] . . . . .	8
Figure 1.7	Velocity vector diagram . . . . .	9
Figure 1.8	Force vector diagram . . . . .	9
Figure 1.9	Representation of helical vortex sheets from a three-bladed HAWT . .	11
Figure 1.10	RANS simulation results including validation against analytical (b) and experimental (c) data [2] . . . . .	13
Figure 1.11	Contours taken at a horizontal plane at hub height of (a) instantaneous and (b) time-averaged velocity normalized by hub height wind speed, (c) resolved turbulent kinetic energy normalized by hub height wind speed squared, and (d) instantaneous resolved modified pressure normalized by $1/2\rho_0 U_{hub}$ [3]. . . . .	16
Figure 1.12	Modern HAWT performance [1] . . . . .	19
Figure 2.1	Maximum possible $C_P$ with various approximations (Selvaraj et al. [4]).	23
Figure 2.2	A schematic of the proposed dual-rotor concept. . . . .	24
Figure 2.3	RANS simulation results including validation against analytical (b) and experimental (c) data [2] . . . . .	27

Figure 2.4	Comparison of numerically predicted and analytically evaluated (by Newman [5]) $C_P$ . . . . .	29
Figure 2.5	Radial distributions of secondary rotor blade chord and twist. . . . .	30
Figure 2.6	RANS simulation results: (a) pressure contours and streamlines for two secondary rotor sizes, and (b) difference in aerodynamic power coefficient, $\Delta C_P = C_{PDRWT} - C_{PSRWT}$ due to the addition of a secondary rotor. . . . .	32
Figure 2.7	RANS simulation results: (a) pressure contours and streamlines for two axial separation distances, and (b) difference in aerodynamic power coefficient, $\Delta C_P = C_{PDRWT} - C_{PSRWT}$ due to the addition of a secondary rotor. . . . .	33
Figure 2.8	Domain size for the LES runs. . . . .	33
Figure 2.9	A snapshot of iso-surfaces of Q-criterion from the DRWT LES simulation. . . . .	34
Figure 2.10	Radial wake variation comparisons between a single-rotor (HAWT) and a dual-rotor (DRWT) turbine at four downstream distances. . . . .	35
Figure 2.11	Radial turbulence intensity variation comparisons between a single-rotor (SRWT) and a dual-rotor (DRWT) turbine at four downstream distances. . . . .	36
Figure 2.12	A schematic showing the computational domains for the atmospheric boundary layer (precursor) and the main (wind turbine) simulations. The entire box in (a) is the domain for precursor calculations; shaded are shows the smaller domain for wind turbine calculations. In (b), points A-D are lateral midpoints of the rectangular refinement zones. . . . .	42
Figure 2.13	Investigation of turbulent momentum transport into the turbine wake layer: (a) a schematic and (b) cylindrical surface showing the turbine wake layer through which turbulent momentum flux is computed to quantify entrainment in turbine wake. . . . .	43
Figure 2.14	Radial transport of streamwise momentum into the turbine wake layer. Color contours show $\overline{u'_r u'_x} / u_{\infty, h}^2$ on the cylindrical surface of Fig. 2.13 that has been cut at $\theta = \pm 180^\circ$ and unwrapped. . . . .	44

Figure 3.1	A schematic of the DRWT technology by Rosenberg <i>et al.</i> [2] . . . . .	47
Figure 3.2	Functions to obtain axial induction factor, $a$ from $C_P$ and $C_T$ given by 1-D momentum theory, and from $C_T$ given by Eq. 3.1. . . . .	49
Figure 3.3	A correlation derived using wake data from a number of RANS CFD simulations. . . . .	50
Figure 3.4	Non-dimensional chord and twist distributions for the model Tellus T-1995 (Risø) turbine used for validation [6]. . . . .	52
Figure 3.5	Comparisons with experimental data and BEM results for the Tellus T-1995 (Risø) turbine: (a) power variation with wind speed, and (b) the same information presented as characteristic $(C_P - \lambda)$ curves. . . .	53
Figure 3.6	Comparisons of radial variation of force coefficients at $\lambda = 6.0$ against BEM results for the Tellus T-1995 (Risø) turbine . . . . .	54
Figure 3.7	Trailing wake vorticity behind the two rotors of a dual-rotor wind turbine. Each rotor is three bladed. The three colors: red, blue, and black denote the trailing vorticity from each blade of the two rotors. . . . .	55
Figure 3.8	Predicted variation in % $C_P$ of a DRWT with relative angular position between the primary and the secondary rotors. . . . .	56
Figure 3.9	Panel code results for the NACA 0030 airfoil at freestream Mach number of 0.2 and zero angle of attack: (a) contours of percentage difference between local and freestream pressure, and (b) magnitude of difference between local and freestream pressure and flow speed along the dashed line in (a). . . . .	57
Figure 3.10	Computational grid and result of the RANS/AD method applied to a DRWT: (a) axisymmetric grid (every fifth point shown for clarity), and (b) pressure contours and streamlines (zoomed in near the DRWT). . .	59
Figure 3.11	Iso-surfaces of Q-criterion ( $Q = 0.05$ ) computed using the LES/ALM method. The surfaces show the bound and trailing vortices and are colored with the r.m.s. of axial velocity. . . . .	60

Figure 3.12	Comparisons between CFD and VLM of spanwise variations of angle of attack and torque force coefficient for the following parameters of the secondary rotor: $r_{t,s}/r_{t,m} = 0.25$ and $\lambda_s = 8.0$ . . . . .	61
Figure 3.13	Comparisons between CFD and VLM of spanwise variations of angle of attack and torque force coefficient for the following parameters of the secondary rotor: $r_{t,s}/r_{t,m} = 0.40$ and $\lambda_s = 8.0$ . . . . .	62
Figure 3.14	Parametric sweep results - contours of difference in aerodynamic power coefficient, $\Delta C_P = C_{PDRWT} - C_{PSRWT}$ as predicted by (a) RANS and (b) VLM are shown. The parameters are tip radius and tip speed ratio of the secondary rotor. . . . .	63
Figure 3.15	VLM predictions of aerodynamic power coefficients of a DRWT and the corresponding SRWT as a function of the man rotor tip speed ratio, $\lambda_m$ . . . . .	64
Figure 4.1	A schematic showing flow direction change. . . . .	67
Figure 4.2	Experimental data showing flow angle change in a neutrally stratified atmosphere. Courtesy Takle [7]. . . . .	67
Figure 4.3	Subsequent pressure drops from multiple wind turbines. . . . .	67
Figure 4.4	Flow vectors and aerodynamic forces on a rotor blade section. . . . .	69
Figure 4.5	Non-dimensional chord and twist distributions for the model Tellus T-1995 (Risø) turbine used for validation [6]. . . . .	69
Figure 4.6	$C_P$ - $\lambda$ curve for Risø turbine. . . . .	70
Figure 4.7	Radial thrust force coefficient for Risø turbine at $\lambda = 7$ . . . . .	71
Figure 4.8	Radial torque force coefficient for Risø turbine at $\lambda = 7$ . . . . .	72
Figure 4.9	Finite wind farm domain. . . . .	73
Figure 4.10	Periodic wind farm domain. . . . .	74
Figure 4.11	Mean flow contours from a tightly spaced wind farm simulated using LES+ADM. . . . .	74
Figure 4.12	Flow angle change from uniform LES simulation of semi-infinite wind farm. . . . .	75

Figure 4.13	Contour of mean flow deflection from uniform LES simulation of semi-infinite wind farm. . . . .	75
Figure 4.14	Contour of mean pressure from uniform LES simulation of semi-infinite wind farm. . . . .	75
Figure A.1	The three coordinate systems used and their interrelationships. The CFD simulations are performed in $(\hat{e}_{\bar{x}}, \hat{e}_{\bar{y}}, \hat{e}_{\bar{z}})$ ; meanflow is along the $\hat{e}_x$ direction. . . . .	78

## ACKNOWLEDGEMENTS

I would like to take this opportunity to express my gratitude to those who have helped me throughout my career at Iowa State and to my family and friends who have supported me.

First, Dr. Anupam Sharma who has been a source of guidance and knowledge every step of the way. I could not have asked for a more willing and helpful advisor. The research projects were always interesting and challenging.

I would like to thank Dr. Eugene S. Takle and Dr. Partha Sarkar for setting me on the wind energy path while I was still an undergraduate and for encouraging me to continue my education. Their mentorship has always been a huge source of inspiration.

To my committee members, thank you for your technical advice and contributions to this dissertation.

Thanks to Dr. James McCalley for your effort and commitment to the WESEP program. I learned so much about all aspects of wind energy from the various courses and seminars that you organized.

Thanks to my fellow graduate students, especially those in my research group with which I have worked so closely: Behnam Moghadassian, Bharat Agrawal, Suganthi Selveraj, Xingeng Wu, Andrew Bodling, and Vishal Vijay.

Finally, I want to thank my friends and family for supporting me over the last three and a half years. Thanks especially to my parents, Kent and Janice, my brother, Reid, and my grandmother, Virginia. Thanks Kirsten, Andrew N., Brian, Jared, Jeff, Kit, Bennett, Nick, Andrew S., David B. (x2), Reid B., Moses, Matt, Abbey, Jinny, Dillon, Logan, Michael, Charlie, Andy, Abhishek, Kain, and countless others.

## ABSTRACT

This dissertation serves to summarize my research into wind farm and wind turbine aerodynamics. Included in this thesis is a summary of the methods I use as well as the four research problems that I investigated.

Motivation is provided for my research as well as an overview of the computational methods that I use. These methods include analytical methods such as blade element momentum (BEM) theory and the vortex lattice method as well as computational fluid dynamic methods like the Reynolds averaged Navier-Stokes (RANS) equations and large eddy simulation (LES). These methods are used to investigate wind turbine and wind farm aerodynamics. In particular, I use these methods to confront the various forms of loss that wind turbines and wind farms experience. They include the losses that individual turbines experience due to swirl, induction, and viscosity as well as the loss that wind farms experience due to turbine-wake interaction.

Horizontal axis wind turbines (HAWTs) suffer from aerodynamic inefficiencies in the blade root region (near the hub) due to several non-aerodynamic constraints. Aerodynamic interactions between turbines in a wind farm also lead to significant loss of wind farm efficiency. A new dual-rotor wind turbine (DRWT) concept is proposed that aims at mitigating these two losses. A DRWT is designed that uses an existing turbine rotor for the main rotor, while the secondary rotor is designed using a high lift-to-drag ratio airfoil. Reynolds Averaged Navier-Stokes computational fluid dynamics simulations are used to optimize the design. Large eddy simulations confirm the increase energy capture potential of the DRWT. Wake comparisons however do not show enhanced entrainment of axial momentum.

I extend the prescribed wake vortex lattice method (VLM) to perform aerodynamic analysis and optimization of dual-rotor wind turbines. The additional vortex system introduced by the secondary rotor of a DRWT is modeled while taking into account the singularities that occur when the trailing vortices from the secondary (upstream) rotor interact with the bound vortices

of the main (downstream) rotor. Pseudo-steady assumption is invoked and averaging over multiple relative rotor positions is performed to account for the primary and secondary rotors operating at different rotational velocities. This implementation of the VLM is first validated against experiments and blade element momentum theory results for a conventional, single rotor turbine. The solver is then verified against RANS CFD results for two DRWTs. Parametric sweeps are performed using the proposed VLM algorithm to optimize a DRWT design. The problem with the algorithm at high loading conditions is highlighted and a solution is proposed that uses RANS CFD results to calibrate the VLM model.

In addition to wake losses, aerodynamic interaction between turbines in wind farms leads to surface flow convergence . This phenomenon has been observed in field tests with surface flux stations. A hypothesis is proposed to explain this surface flow convergence phenomenon - incomplete pressure recovery behind a turbine leading to successive pressure drops in tightly-spaced turbine arrays leads to drop in overall pressure deep inside a wind plant; this low-pressure acts as an attractor leading to flow convergence. Numerical investigations of the phenomenon of surface flow convergence are carried out that support this hypothesis. An actuator disk model to represent wind turbines in an LES CFD solver is used to simulate hypothetical wind plants. The flow convergence phenomenon reflects as change in flow velocity direction and is more prominent near the ground than at turbine hub height. Numerical simulations of wind plant aerodynamics are conducted with various approximations to investigate and explain the flow convergence phenomenon.



# CHAPTER 1. WIND TURBINE AERODYNAMICS AND PERFORMANCE

## 1.1 Introduction

The United States consumes more electricity than any other country in the world except for China. A significant majority of the energy consumed by the US is generated using fossil fuels. Concerns over climate change and the scarcity of natural resources has led to the rise of renewables, such as wind and solar, as an alternative energy source to carbon based fuels such as natural gas and coal. Several issues prevent wind and other forms of renewable energy from completely replacing fossil fuels. The main roadblock, however, is cost. As high wind sites continue to be developed, operators must find practical and creative means to keep cost low. Research spent improving a typical horizontal axis wind turbine (HAWT) has reached a point of diminishing returns. HAWTs are quickly approaching their theoretical maximum efficiency. Radical design alterations have become necessary to increase the production of wind energy whilst keeping costs low.

A wind turbine is a device that converts kinetic energy from the atmosphere into electrical energy. Modern utility scale HAWTs use a single rotor consisting of three fiberglass blades. These machines typically produce around 1-2 MW of energy onshore but can produce as high as 3-5 MW offshore. The amount of power extracted by a wind turbine is proportional to the cube of the wind speed,  $V$ , and is linearly proportional to the swept area of the rotor,  $A$ .

$$P = \frac{1}{2} \rho V^3 A C_P \quad (1.1)$$

$C_P$ , is a measure of aerodynamic performance for a wind turbine. It represents the fraction of kinetic energy flowing through the swept area of a wind turbine that is converted into mechanical energy. This chapter first describes several ways of evaluating wind turbine performance

including analytical, semi-analytical, computational and experimental methods. It concludes with a summary of modern HAWT performance.

## 1.2 Analytical & Semi-analytical Methods

From an engineering perspective, analytical models represent the simplest method for evaluating the performance of HAWTs. They require little to no computer resources nor experimental equipment. Several methods that fall in this category are described in this section.

### 1.2.1 1-D Momentum Theory

1-D momentum theory can be used to predict the theoretical maximum power coefficient for a single rotor HAWT. It is derived under the assumption that the rotor can be represented as an infinitely thin permeable disk. This rotor is ideal in the sense that there are no losses due to friction and that the wake has no swirl, that is, there is not rotational component of velocity. It is simply a drag device acting in the opposite direction of the wind due to a thrust imposed by the rotor.

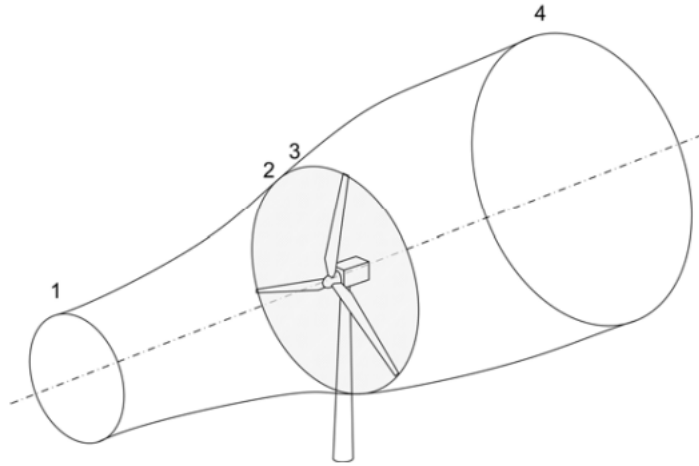


Figure 1.1: Illustration of a 1-D Streamtube [1]

Figure 1.1 represents a streamtube that encompasses the mass flow through the rotor plane. The presence of a thrust force causes the streamlines to diverge as it flows through the wind

turbine. In this representation, the numbers 1-4 represent locations at the entrance of the streamtube, immediately upwind and downwind of the rotor plane, and the exit of the streamtube respectively. Conditions at location 1 are that of the freestream. The thrust acting on the flow is defined as the pressure difference between locations 1 and 2 multiplied by the area of the rotor disk ( $A_2 = A_3 = A_d$ ):

$$T = (P_2 - P_3)A_d \quad (1.2)$$

where,

$$A_d = \pi R^2. \quad (1.3)$$

Assuming that flow is stationary, incompressible, inviscid and that no external forces are acting on it, Bernoulli's equation can be used to derive relationships between velocity and pressure at different locations along the streamtube. Bernoulli's equation is not valid across the rotor plane itself because an external force is acting on the flow. This causes a discontinuous pressure decrease at the location of the rotor,  $P_2 \neq P_3$ . However, the velocity profile across the plane is continuous, therefore  $U_2 = U_3 = U_d$ . The pressure at the entrance and exit of the streamtube is assumed to be that of the freestream,  $P_1 = P_4 = P_\infty$ . Furthermore, the mass flow rate at any cross-section along the streamtube must remain constant. Under these assumptions, conservation equations can be written as follows:

$$\dot{m} = \rho U_\infty A_1 = \rho U_d A_d = \rho U_4 A_4 \quad (\text{mass}) \quad (1.4)$$

$$T = \rho U_d A_d (U_\infty - U_4) = (P_2 - P_3) A_d \quad (\text{momentum}) \quad (1.5)$$

$$P_\infty + \frac{1}{2} \rho U_\infty^2 = P_2 + \frac{1}{2} \rho U_d^2 \quad (\text{energy}) \quad (1.6)$$

$$P_3 + \frac{1}{2} \rho U_d^2 = P_2 + \frac{1}{2} \rho U_4^2 \quad (\text{energy}). \quad (1.7)$$

The axial induction factor,  $a$ , represents the fractional loss of velocity between the freestream and the location of the wind turbine and can be defined as follows:

$$a = \frac{U_\infty - U_d}{U_\infty} \quad (1.8)$$

From these relations, the non-dimensional thrust ( $C_T$ ) and power ( $C_P$ ) coefficients can be found as a function of axial induction factor.

$$C_T = \frac{T}{\frac{1}{2}\rho U_\infty^2 A_d} = 4a(1-a) \quad (1.9)$$

$$C_P = \frac{P}{\frac{1}{2}\rho U_\infty^3 A_d} = 4a(1-a)^2 \quad (1.10)$$

By differentiating  $C_P$  with respect to  $a$ , the maximum power coefficient can be determined.

$$\frac{dC_P}{da} = 4(1-a)(1-3a) \quad (1.11)$$

By solving  $\frac{dC_P}{da} = 0$ , it follows that  $C_{P_{max}} = 16/27$  for  $a = \frac{1}{3}$ . This theoretical maximum power coefficient for a wind turbine is commonly referred to as the *Betz Limit* [9], or sometimes the Lanchester-Betz Limit. The Betz limit is used as a benchmark for modern HAWT performance with the understanding that no single rotor HAWT can exceed a power coefficient of 16/27. It should be noted that certain assumptions taken in the process of deriving Betz limit are not entirely physical. For instance, HAWTs are torque driven devices, meaning that the wake should have some amount of rotation not accounted for in 1-D momentum theory.

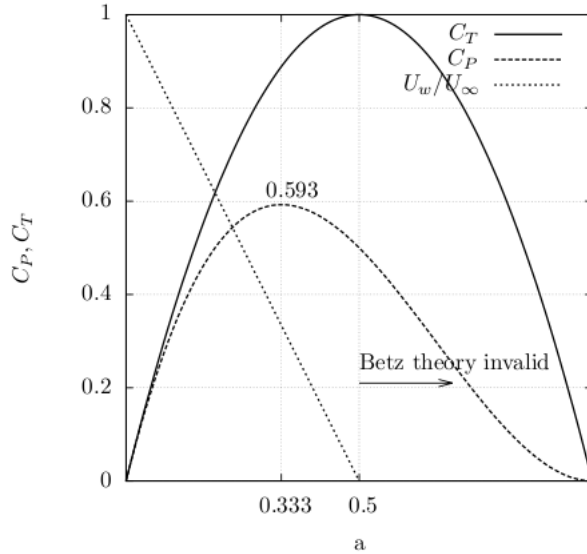


Figure 1.2:  $C_P$  and  $C_T$  as a function of axial induction factor,  $a$

### 1.2.2 Momentum Theory with Swirl

The effects of rotational velocity, or swirl, in the wake is easily accounted for in momentum theory by adding rotation to the actuator disk. By allowing for a change in angular momentum across the rotor plane, the analysis becomes 2-D and therein more accurate than the 1-D theory described in the previous section.

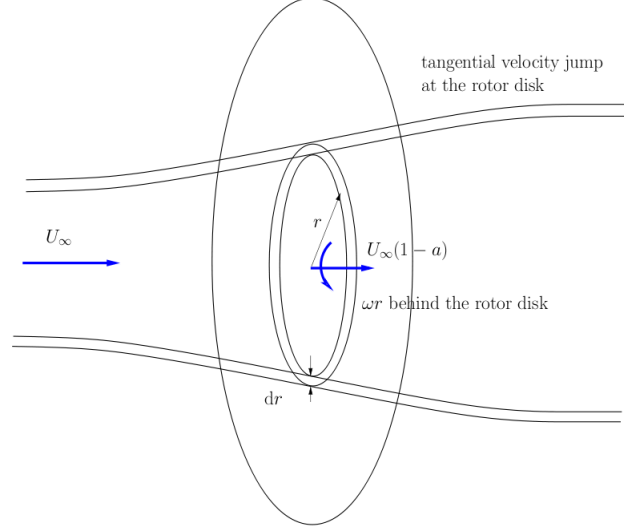


Figure 1.3: Illustration of a rotating actuator disk

First, consider an annular element of the actuator disk at radius  $r$  as seen in Figure 1.3. From the perspective of the disk, the incoming flow has an angular velocity equal to the rate of rotation of the disk,  $\Omega$ . Equation 1.8 can still be used to determine the axial velocity at the location of the disk. The rotating disk introduces a perturbation,  $\omega$ , to the angular velocity of the wind (Figure 1.4). In the frame of reference rotating with the disk, the total pressure remains constant across the disk:

$$P_2 + \frac{1}{2}\rho((U_\infty(1-a))^2 + \Omega^2 r^2) = P_3 + \frac{1}{2}\rho((U_\infty(1-a))^2 + (\Omega + \omega)^2 r^2). \quad (1.12)$$

Which can be reduced to:

$$P_2 - P_3 = \rho(\Omega + \omega/2)\omega r^2. \quad (1.13)$$

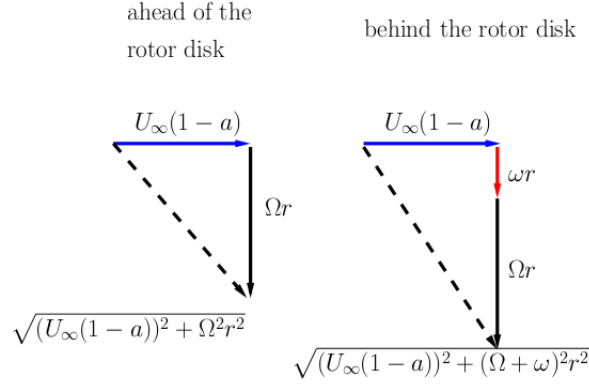


Figure 1.4: Flow velocity at a rotating element

The thrust force acting on a radial strip can be calculated as follows:

$$dT = (P_2 - P_3)dA, \quad \text{where} \quad dA = 2\pi r dr. \quad (1.14)$$

Substituting Equation 1.13:

$$dT = \rho(\Omega + \omega/2)\omega r^2 2\pi r dr. \quad (1.15)$$

The angular induction factor,  $a'$ , is defined as:

$$a' = \frac{\omega}{2\Omega}. \quad (1.16)$$

Therefore it follows:

$$dT = 4a'(1 + a')\frac{\rho\Omega^2 r^2}{2} 2\pi r dr. \quad (1.17)$$

The incremental thrust can also be derived using the conservation of linear momentum similar to Equation 1.5 as:

$$dT = 4a(1 - a)\frac{\rho U_\infty^2}{2} 2\pi r dr. \quad (1.18)$$

Equating 1.17 and 1.18 gives

$$\frac{a(1 - a)}{a'(1 + a')} = \lambda_r^2. \quad (1.19)$$

Where  $\lambda_r = \frac{\Omega r}{U_\infty}$  is the ratio between the velocity of the element and the freestream wind speed. At  $r = r_{tip} = R$ , it is called the tip speed ratio,  $\lambda$ . This is an important non-dimensional quantity. It is used to define the operating condition of a HAWT, specifically, the angular

velocity of the rotor with respect to  $U_\infty$ . Balancing angular momentum across the rotor disk yields the incremental torque,  $d\tau$ , acting on the flow from the annular element:

$$d\tau = r \times d\dot{m}(\omega r - 0) = d\dot{m}\omega r^2 = \rho 2\pi r dr U_\infty (1 - a) \omega r^2. \quad (1.20)$$

Substituting Equation 1.16:

$$d\tau = 2\rho(2\pi r dr)U_\infty(1 - a)a'\Omega r^2. \quad (1.21)$$

The total power can be calculated by integrating the incremental torque multiplied by the angular velocity of the disk:

$$dP = \Omega d\tau = \Omega \times 2\rho(2\pi r dr)U_\infty(1 - a)a'\Omega r^2. \quad (1.22)$$

$$P = \int_0^R dP = 4\pi\Omega^2\rho U_\infty \int_0^R a'(1 - a)r^3 dr \quad (1.23)$$

By changing the integrand from  $r$  to the speed ratio ( $r = \frac{U_\infty}{\Omega}\lambda_r$  and  $dr = \frac{U_\infty}{\Omega}d\lambda_r$ ) the power can be calculated as a function of tip speed ratio,

$$P = 4\pi\Omega^2\rho U_\infty \int_0^\lambda a'(1 - a)\lambda_r^3 \frac{U_\infty^4}{\Omega^4} d\lambda_r. \quad (1.24)$$

Power can be completely by dividing by  $\frac{1}{2}\rho V^2 A_d$  to obtain the following expression for  $C_P$ :

$$C_P = \frac{8}{\lambda^2} \int_0^\lambda a'(1 - a)\lambda_r^3 d\lambda_r \quad (1.25)$$

In order to maximize  $C_P$ , the quantity  $a'(1 - a)$  must be maximized at each radial element. An expression for optimum  $a'$  can be achieved by taking the derivative of the argument with respect to  $a$  and setting it equal to zero:

$$\frac{d}{da}(a'(1 - a)) = \frac{da'}{da} - a' - a\frac{da'}{da} = 0, \quad (1.26)$$

$$\frac{da'}{da} = \frac{a'}{1 - a}. \quad (1.27)$$

Differentiating Equation 1.19 with respect to  $a$ :

$$\frac{d}{da}(a(1 - a)) = \lambda_r^2 \frac{d}{da}(a'(1 + a')), \quad (1.28)$$

$$1 - 2a = \lambda_r^2 \left( \frac{da'}{da} + 2a' \frac{da'}{da} \right), \quad (1.29)$$

$$\frac{da'}{da} = \frac{1-2a}{\lambda_r^2(1+2a')}. \quad (1.30)$$

Solving equations 1.19, 1.27, and 1.30 yields an expression for optimum  $a'$  as a function of  $a$ :

$$a' = \frac{1-3a}{4a-1}. \quad (1.31)$$

Equation 1.31 and 1.19 can be used to calculate the values of  $a'$  and  $\lambda$  for a given  $a$  that yields maximum power coefficient,  $C_{Pmax}$ . It is apparent from Figure 1.6 that the ideal turbine would operate at a high tip speed ratio. That is to say, for a constant wind speed,  $U_\infty$ , the rotor should be spinning as fast as possible. This method, while more accurate than the 1-D momentum theory, still overpredicts power production for HAWTs. By not accounting for the presence of a finite number of blades and viscosity, this method neglects substantial losses.

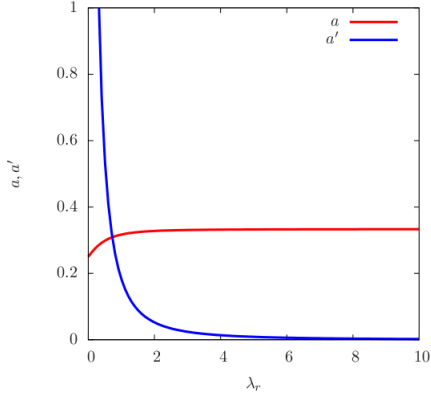


Figure 1.5: Optimum  $a$  and  $a'$  with respect to  $\lambda$  [1]

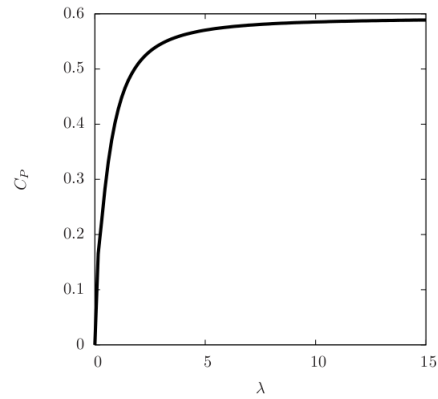


Figure 1.6:  $C_P$  vs  $\lambda$  [1]

### 1.2.3 Blade Element Momentum Theory

In 1.2.1 and 1.2.2, blade geometry is completely ignored. Blade Element Momentum theory (BEM) combines airfoil aerodynamics with momentum theory. BEM takes an iterative approach to predicting HAWT performance. First, a distribution of axial and angular induction factors in rotor plane are initialized. Next, 2-D airfoil polars and knowledge of the blade geometry are used to calculate lift and drag forces acting along the blades. The relative velocity,  $U_r$ , at an arbitrary element of the blade depends on its radius, rotational velocity of the blade, wind speed at the plane of rotation, and twist ( $\theta$ ) of the blade (Figure 1.7).





this factor is implemented in BEM theory, it results in a decrease in power prudction.

$$F = \frac{2}{\pi} \cos^{-1}(\exp(-f)), \quad \text{where } f = \frac{B(r-R)}{2r \sin(\phi)} \quad (1.32)$$

The BEM process is altered as follows:

$$dT = 4\pi r \rho U_\infty^2 a(1-a)F dr, \quad (1.33)$$

$$d\tau = 4\pi r^3 \rho U_\infty^2 \Omega a'(1-a)F dr. \quad (1.34)$$

The induction factors can be derived to yield:

$$a = 1 / \left( \frac{4F \sin^2(\phi)}{\sigma_r C_T} + 1 \right), \quad (1.35)$$

$$a = 1 / \left( \frac{4F \sin(\phi) \cos(\phi)}{\sigma_r C_{\tau F}} - 1 \right). \quad (1.36)$$

where  $\sigma_r$  is the local solidity ratio defined by the ratio of the area of an annular control volume occupied by the blades to the total area of the annulus.  $C_T$  and  $C_\tau$  are the non-dimensionalized thrust and torque forces respectively.

#### 1.2.4 Vortex Lattice Method

Another way to model blades discretely is to use lifting line theory, which states that the lift per unit span from an airfoil is directly proportional to the amount of bound circulation ( $\Gamma$ ) it produces (eq. 1.37). The vortex lattice method (VLM) uses this theory, as well as knowledge of the blade geometry, to predict the performance of a HAWT with a discrete number of blades. As a lift generating blade rotates, it leaves a trailing vortex sheet that convects with the wind. A three-bladed HAWT produces three helical vortex sheets as shown in Fig. 1.9.

$$L' = \rho_\infty U_\infty \Gamma \quad (1.37)$$

To implement VLM, first initial estimates for  $C_P$  and bound vorticity,  $\Gamma(r)$  are made. For example, the Betz optimum value ( $C_P=0.593$ ) and a uniformly distributed  $\Gamma$  over the blade span. Next, the axial induction ( $a$ ) is estimated using the 1-D momentum theory and the initial guess of  $C_P$ . With this knowledge, the pitch of the helices,  $\phi_t$ , can be determined by calculating

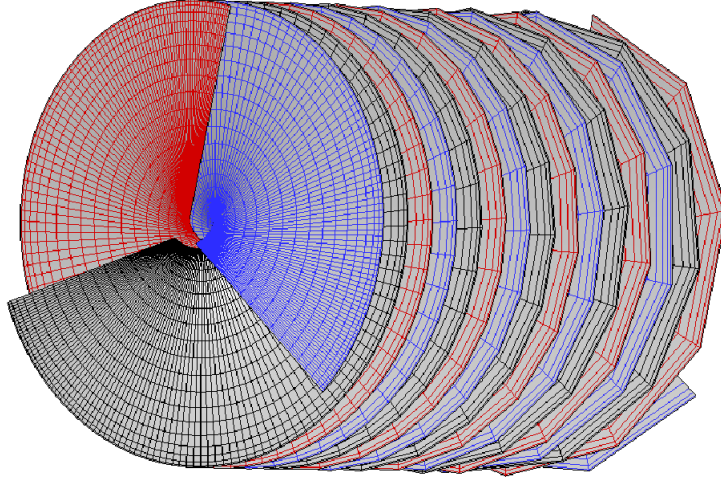


Figure 1.9: Representation of helical vortex sheets from a three-bladed HAWT

the inflow angle at the tip of the blades. Biot-Savart's law is then be used to calculate the induction factors  $a$  and  $a'$  at each point on the blades. Finally, the lift and drag at discrete blade sections can be calculated using airfoil look-up tables and the knowledge of local inflow conditions, after which,  $C_P$  can be recalculated. This process is repeated until  $C_P$  converges. This method is described in detail in Chapter 3.

### 1.3 Computational Methods

The models described in Section 1.2 are simple and therefore very useful in the preliminary stages of HAWT design. In the last couple of decades, advances in computing has led to an increase in the use of computational fluid dynamics (CFD). The wind industry has been quick to adopt CFD to study wind turbine and wind farm aerodynamics.

Similar to the analytical methods discussed in Section 1.2, CFD models have varying degrees of fidelity. Engineers employ a wide range of numerical methods to solve the Navier-Stoker (N-S) equations, which completely describe fluid motion in the form of non-linear partial differential equations. They are based on the universal laws of conservation of mass (1.38), momentum (1.39), and energy (1.40) and can be written in differential form as

$$\frac{\partial \rho}{\partial t} + \nabla \cdot (\rho \vec{V}) = 0, \quad (1.38)$$

$$\rho \frac{D\vec{V}}{Dt} = \rho \vec{f} - \nabla p + \frac{\partial}{\partial x_j} \left[ \mu \left( \frac{\partial u_i}{\partial x_j} + \frac{\partial u_j}{\partial x_i} \right) - \frac{2}{3} \delta_{ij} \mu \frac{\partial u_k}{\partial x_k} \right], \quad (1.39)$$

$$\frac{\partial E_t}{\partial t} + \nabla \cdot E_t \vec{V} = \frac{\partial Q}{\partial t} - \nabla \vec{q} + \rho \vec{f} \cdot \vec{V} + \nabla \cdot (\Pi_{ij} \cdot \vec{V}). \quad (1.40)$$

Resolving the flow features determined by these equations completely in the computational domain is extremely expensive for most engineering problems. Most models simplify the N-S equations by applying certain assumptions. For example, it is valid to assume that air can be considered incompressible for wind turbine/farm analysis because we deal with highly subsonic flow.

The growth in popularity of CFD for wind energy applications has led to the development of a variety of different software packages. Since every application requires different degrees of accuracy, researchers have developed a wide array of algorithms to model wind turbine aerodynamics. Vermeer [10] and Sanders [11] provide great descriptions and reviews of many numerical methods associated with wind farm aerodynamics. This section describes a few of these methods, each of which play different, yet valuable, roles in HAWT and wind farm design and analysis.

### 1.3.1 RANS + Actuator Disk

Reynolds Averaged Navier-Stokes (RANS) simulations offer an accurate means to model wind flow through a HAWT. RANS is useful for modelling turbulent flow at a relatively low cost. Resolving the geometry (e.g. turbine rotor blades) can be computationally expensive. An alternative to resolving the geometry is to mimic the effect its effect on the flow using source terms in the governing equations; these sources replace the blades, for example, in a wind turbine. One can, for example, add a distributed force term,  $f_i$ , to the incompressible

RANS equations in the form of a generalized actuator disk:

$$\frac{\partial \bar{u}_i}{\partial x_i} = 0, \quad \text{and} \quad (1.41)$$

$$\bar{u}_j \frac{\partial \bar{u}_i}{\partial x_j} = -\frac{1}{\rho} \frac{\partial \bar{p}}{\partial x_i} - \nu \frac{\partial^2 \bar{u}_i}{\partial x_j^2} - \frac{\partial \overline{u'_i u'_j}}{\partial x_j} + \frac{f_i}{\rho} \quad (1.42)$$

where the Reynolds stress tensor  $\overline{u'_i u'_j}$  is modeled using eddy (“turbulent”) viscosity as  $\nu_t \partial \bar{u}_j / \partial x_j$ . Turbulent viscosity,  $\nu_t$  is obtained using turbulent kinetic energy,  $k$  and dissipation,  $\epsilon$ , which are themselves obtained by solving a transport equation for each. The term  $f_i$  represents body force per unit volume and is obtained using airfoil polars and local flow velocity. The force,  $f_i$  is distributed over a volume and a Gaussian distribution is applied along the flow direction according to Mikkelsen [12]. This model has been validated against experimental data as well as BEM theory as seen in Figure 1.10.

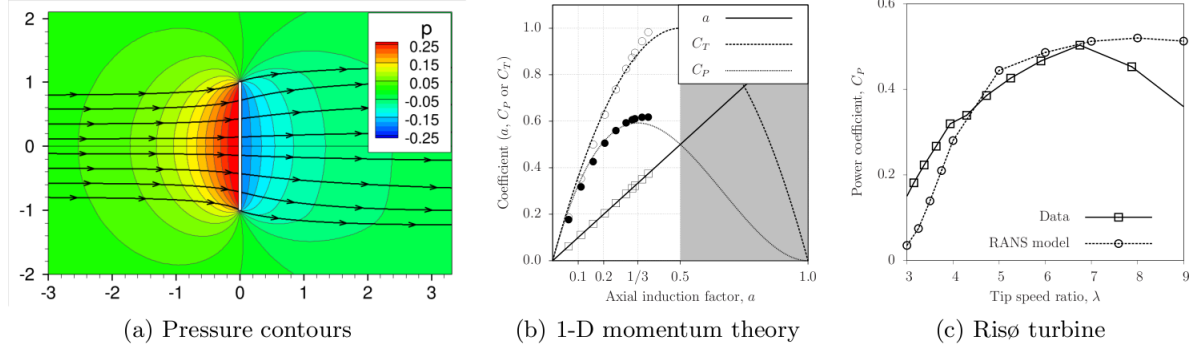


Figure 1.10: RANS simulation results including validation against analytical (b) and experimental (c) data [2]

### 1.3.2 LES + Actuator Line

Large Eddy Simulations (LES) of wind turbines and farms have received a lot of attention recently (see e.g., [13, 14, 15, 16, 17]), partly because computational resources are becoming increasingly more abundant. Most notably, engineers at the National Renewable Energy Lab (NREL) have developed an LES software called Simulator fOr Wind Farm Applications (SOWFA) [3, 18]. Similar to the RANS model detailed in section 1.3.1, SOWFA models the

wind turbine blades with a distributed force per unit volume term,  $f_i$ , in the momentum equation. However, instead of applying the force on a disk, the blades are modeled as discrete actuator lines that rotate with time. Airfoil lookup tables as well as the local velocity are used to calculate the force acting on the flow as a function of space and time. This method is called the Actuator Line Model (ALM). This method allows the capturing of blade tip vortices by resolving the azimuthal variation of  $f_i$ .

In LES, the spatially filtered, incompressible forms of the N-S equations are solved using spatial and temporal discretization. Spatial filtering introduces unresolved, sub-filter scale (also called sub-grid scale or SGS) stresses, which have to be modeled. The width of the spatial filter is taken to be the grid-filter width given by  $\Delta = (\Delta_x \Delta_y \Delta_z)^{1/3}$ . The actuator line model (ALM) is used for rotor parameterization. Denoting spatially-filtered quantities by  $(\sim)$ , the governing fluid flow equations are:

$$\frac{\partial \tilde{u}_i}{\partial x_i} = 0, \quad (1.43)$$

$$\begin{aligned} \frac{\partial \tilde{u}_i}{\partial t} + \tilde{u}_j \left( \frac{\partial \tilde{u}_i}{\partial x_j} - \frac{\partial \tilde{u}_j}{\partial x_i} \right) = & -\frac{\partial \tilde{p}^*}{\partial x_i} - \frac{\partial \tau_{ij}}{\partial x_j} + \nu \frac{\partial^2 \tilde{u}_i}{\partial x_j^2} \\ & \underbrace{-f_i/\rho_0}_{\text{turbine force}} + \underbrace{\delta_{i1} F_P}_{\text{driving pressure}} + \underbrace{\delta_{i3} g_0 (\tilde{\theta} - \langle \tilde{\theta} \rangle) / \theta_0}_{\text{buoyancy force}} + \underbrace{F_c \epsilon_{ij3} \tilde{u}_j}_{\text{coriolis force}} \end{aligned} \quad (1.44)$$

$$\frac{\partial \tilde{\theta}}{\partial t} + \tilde{u}_j \frac{\partial \tilde{\theta}}{\partial x_j} = \frac{\partial q_j}{\partial x_j} + \alpha \frac{\partial^2 \tilde{\theta}}{\partial x_j^2} \quad (1.45)$$

where,  $\tilde{p}^* = \tilde{p}/\rho_0 + \tilde{u}_i \tilde{u}_j / 2$  is the modified kinematic pressure,  $\tau_{ij} = \widetilde{u_i u_j} - \tilde{u}_i \tilde{u}_j$ , is the sub-grid scale (SGS) stress tensor, and  $q_i = \widetilde{u_j \theta} - \tilde{u}_j \tilde{\theta}$  is the SGS heat flux.  $f_i$  is the momentum source from the ALM,  $\delta_{i1} F_P$  is the pressure gradient driving the flow,  $\theta$  is potential temperature and  $\alpha$  is the thermal diffusivity of the fluid. The deviatoric part of the SGS stress tensor,  $\tau_{ij}$ , is typically modeled using an eddy-viscosity model  $\tau_{ij} - 1/3 \delta_{ij} \tau_{kk} = -2\nu_{sgs} \widetilde{S_{ij}}$  and the SGS heat flux with an eddy-diffusivity model  $q_j = \widetilde{u_j \theta} - \tilde{u}_j \tilde{\theta} = -(\nu_{sgs}/Pr_{sgs}) \partial \tilde{\theta} / \partial x_j$ , where,

$\widetilde{S}_{ij} = 1/2 (\partial \widetilde{u}_i / \partial x_j + \partial \widetilde{u}_j / \partial x_i)$  is the resolved strain-rate tensor and  $Pr_{sgs}$  is the SGS Prandtl number. The mixing-length model by Smagorinsky,  $\nu_{SGS} = (C_S \Delta)^2 |\widetilde{S}|$  is used to model  $\nu_{SGS}$ .

The numerical scheme in SOWFA uses a finite-volume formulation and the discretization is second order in space (central) and time (backward). A two-step solution procedure is used when atmospheric boundary layer-turbine interaction is important. First, turbulent flow is generated without the presence of the turbines. Once this domain reaches a quasi-equilibrium state, boundary data from this domain is used as boundary conditions for a wind farm, driving fully turbulent flow through an array of turbines (modeled as actuator lines).

LES is especially useful for turbulent boundary layer simulations. The inflow experience by a HAWT in a wind plant is turbulent and contains a large vertical shear. The hub height of most HAWTs is around 80 meters, well within the atmospheric boundary layer (ABL). ABL effects can be accounted for in LES with a potential temperature ( $\theta$ ) profile and a wall model. A comprehensive study of HAWT aerodynamics should include the unsteady nature of the ABL. Turbulence from the atmosphere and upstream HAWTs cause inefficiencies in wind plants as well as contribute to high fatigue loading. Chuchfield *et al.* used an early version of SOWFA to simulate the flow at Lillgrund Wind Farm off the Southern coast of Sweden with mixed results (see Figure 1.11) [3].

### 1.3.3 Blade Resolved Simulations

In LES and RANS simulations that use a actuator disk or actuator line models wind turbines are represented with momentum sources in the momentum equation,  $f_i$ . With sufficient resources, however, it is possible to resolve the full geometry of the blades in simulations. This is required when the relevant length scale of a problem is less than or equal to the chord of a blade, for example, in near wake or fatigue calculations. Vijaykumar et al. [19] and Lavelly et al. [20] investigate wind turbine aerodynamics with hybrid URANS-LES calculations by fully resolving the turbine blades. The topics covered in this dissertation do not require this level of fidelity.

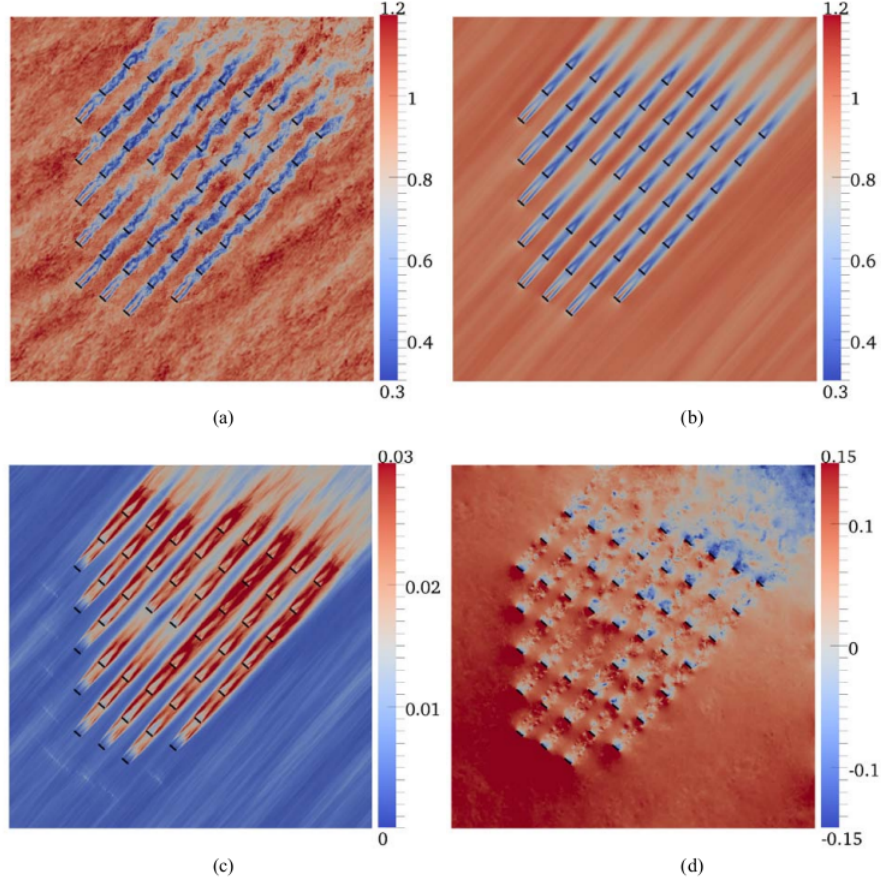


Figure 1.11: Contours taken at a horizontal plane at hub height of (a) instantaneous and (b) time-averaged velocity normalized by hub height wind speed, (c) resolved turbulent kinetic energy normalized by hub height wind speed squared, and (d) instantaneous resolved modified pressure normalized by  $1/2\rho_0 U_{hub}$  [3].

## 1.4 Experimental Methods

Unlike the methods described in Sections 1.2 and 1.3, experimental methods do not involve making simplifying assumptions of the physics of fluid flow. Instead, the accuracy is limited by the setup of the experiment which may be limited by the resources available to the researcher. Experiments range from laboratory scale (see e.g., [21, 22, 23, 24]) to field measurements (see e.g., [25, 26]) and can be used to study isolated HAWT and wind farm aerodynamics alike.



## 1.5 Modern HAWT Performance

Betz limit states that the theoretical maximum power coefficient for a HAWT is  $C_{P_{max}} = 16/27 \approx 0.593$ . In reality, modern HAWTs operate well below this limit. The physical assumptions made in 1-D momentum theory result in a gross overprediction of  $C_{P_{max}}$ . This section investigates these assumptions and presents a more reasonable limit for single rotor HAWT performance.

### 1.5.1 Swirl Loss

1-D momentum theory assumes no wake rotation. Since HAWTs are torque driven devices, this assumption introduces a considerable amount of error. Section 1.2.2 attempts to correct this error by allowing the wake to rotate, or swirl. In doing so, some of the energy extracted by the actuator disk in the 1-D momentum theory is lost due to the introduction of angular momentum in the wake; the associated rotational K.E. is wasted. Furthermore, the maximum achievable power extraction becomes a function of tip-speed ratio,  $\lambda$ , as seen in Figure 1.12.

### 1.5.2 Induction Loss

Momentum theory provides an elegantly simple expression for  $C_{P_{max}}$ , but it neglects the fact that HAWTs have a finite number of blades. This leads to a circumferential variant inflow at the rotor plane generating induction losses as seen in Figure 1.12. Attempts have been made to correct this using hub and tip loss factors. These expressions serve to mimic the loss of lift due to the three-dimensional nature of the flow. Trailing vortices cause a decrease in lift along the blade, especially near the root and tip regions. VLM accounts for this by directly modeling the vorticity trailing the blade and calculating induction in the plane of the rotor caused by these trailing vortex sheets using Biot-Savart's law.

### 1.5.3 Viscous Loss

The analytical methods discussed in this chapter all assume an inviscid flow and therefore ignore the impacts of profile drag. Viscous forces result in diminishing  $C_P$ , especially at high  $\lambda$

(see Fig. 1.12. Over the lifetime of a HAWT, viscous losses increase as blades collect debris such as bugs and dirt. For this reason, it is common practice to coat blades with protective surfaces to prevent the buildup of debris. It is also common for wind farm operators to routinely clean their blades.

#### 1.5.4 Constraints

While the Betz limit states that the maximum attainable  $C_P$  is  $16/27$ , unavoidable losses including swirl, induction, and viscosity leads to a more reasonable  $C_{P_{max}}$  closer to that seen in Figure 1.12. However, this assumes an ideal HAWT designed using an inverse BEM method. It is impossible to manufacture a perfect rotor. Manufacturing constraints limit the twist distribution from an ideal design. Utility scale HAWT blades are almost always fiberglass composites. The manufacturing process consists of laying fiberglass sheets in separate molds before joining the two halves. If the walls of the mold are too steep, as they would be with an ideal twist distribution, the sheets will sag and wrinkle. In practice, linear twist distributions are easier to manufacture.

Furthermore, blades cannot have excessive chord lengths due to transportation constraints. Most blades are fabricated off site, sometimes hundreds of miles from where the HAWT is being constructed. The most practical means of transportation is by truck on major roadways. Not only do trucks have to be capable of carrying the large blade, but it must do so without blocking more than one lane of traffic.

Finally, the blade must be strong enough to withstand high loads, especially near the root region (inner 25% of the rotor). For this reason, blades are designed with thick airfoils near the root that are aerodynamically poor. Flow separation in the root region causes span-wise flow, which deteriorates the aerodynamic performance of the outboard blade sections as well.

#### 1.5.5 Wake Loss

Utility scale turbines are usually deployed en masse in wind farms. It is recognized by the wind energy community that these turbines cannot be studied and/or optimized as if they were operating in isolation. Aerodynamic interactions between turbines in a farm result in

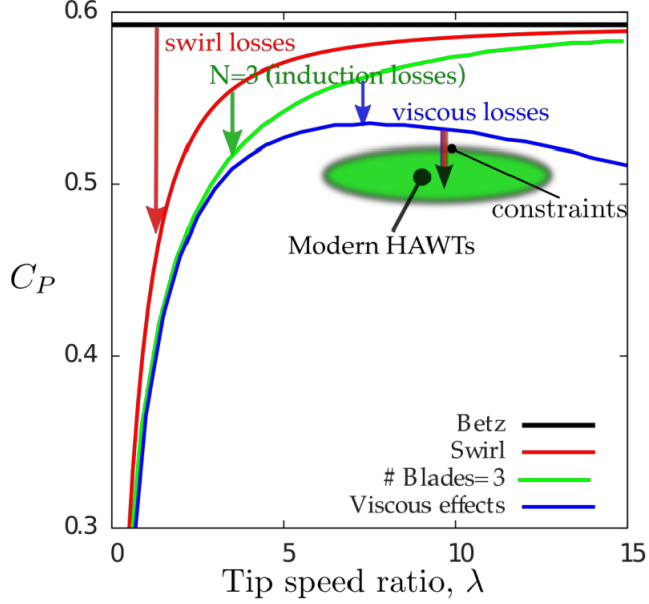


Figure 1.12: Modern HAWT performance [1]

significant energy loss that can range anywhere between 8-40% [27]. The primary mechanism of this energy loss is ingestion (by downstream turbines) of reduced-momentum air present in the wakes of the upstream turbines. The range of this loss is exceptionally wide because of its strong dependence on farm (micro-siting), and atmospheric stability. Highest losses have been observed in offshore turbines when turbine rows are aligned with wind direction, are closely spaced, and when atmospheric flow is stably stratified [28, 29]. In comparison to the large body of work devoted to measuring and predicting wake losses, relatively little research has focused on reducing wake losses. For HAWTs, Corten and Lindenburg [30] have developed a method of farm control in which windward turbines are deliberately yawed (skewed) with respect to wind direction. The concept is to use the lateral force (generated by deliberate yawing of windward turbines) to divert the flow away from downstream turbines. The degree of yaw is determined based on wind and turbine row alignment.

## 1.6 Conclusion

This chapter serves as the groundwork for the rest of the dissertation. Henceforth, methods and concepts from this chapter will be used to confront wind turbine inefficiencies through

the design and implementation of a dual rotor wind turbine. This thesis, in part, serves as an entitlement study to determine the aerodynamic advantages of adding a secondary rotor. It also includes new methods for the analysis and design multi-rotor wind turbines. Finally, this thesis investigates numerically a phenomenon that is not exclusive to DRWTs called surface flow convergence.

In Chapter 2, a dual rotor wind turbine is proposed to mitigate blade root loss and wake losses. Using RANS and an actuator disk model, a parametric sweep is carried out to determine a good configuration for the DRWT. LES and an actuator line model is used to determine how the configuration performs in a uniform boundary layer.

Chapter 3 extends the vortex lattice method for use in analysis of conventional single rotor wind turbines to turbines with multiple rotors. This method is useful to predict the performance of DRWTs at relatively low cost and can be used in the preliminary design stages of DRWTs.

Chapter 4 explores the phenomenon of surface flow convergence using LES and an actuator disk model. Surface flow convergence occurs due to compounding pressure drops in large wind farms that create pressure gradients over the entire farm. This pressure gradient could be responsible for flow convergence which might have microclimatological consequences.

## CHAPTER 2. A NOVEL DUAL-ROTOR TURBINE FOR INCREASED WIND ENERGY CAPTURE

This chapter was published in the [Journal of Physics: Conference Series](#) in 2014.[2]

A Rosenberg, Suganthi Selvaraj, and Anupam Sharma. A novel dual-rotor turbine for increased wind energy capture. In *Journal of Physics: Conference Series*, volume 524, page 012078. IOP Publishing, 2014.

### Abstract

Horizontal axis wind turbines suffer from aerodynamic inefficiencies in the blade root region (near the hub) due to several non-aerodynamic constraints. Aerodynamic interactions between turbines in a wind farm also lead to significant loss of wind farm efficiency. A new dual-rotor wind turbine (DRWT) concept is proposed that aims at mitigating these two losses. A DRWT is designed that uses an existing turbine rotor for the main rotor, while the secondary rotor is designed using a high lift-to-drag ratio airfoil. Reynolds Averaged Navier-Stokes computational fluid dynamics simulations are used to optimize the design. Large eddy simulations confirm the increase energy capture potential of the DRWT. Wake comparisons however do not show enhanced entrainment of axial momentum.

## 2.1 Introduction

A single-rotor horizontal axis wind turbine (HAWT) can capture a maximum of 59.3% of the flow energy passing through the turbine rotor disk. This remarkable result can be derived by applying mass, momentum, and energy conservations laws across a rotor disk assuming the flow to be one-dimensional, steady, and incompressible. This limit was found at around the same time by Albert Betz, Frederick Lanchester, and Nikolay Zhukovsky, but is now referred to simply as the Betz limit. It should be emphasized that this limit assumes the turbine to have a single, un-ducted rotor. On one hand, this limit can be easily surpassed if multiple rotors, or ducted rotors are employed. On the other hand, the Betz limit of achieving 59.3% aerodynamic efficiency is not realizable by any real single-rotor, finite-bladed, un-ducted HAWT. Physical laws and other constraints limit the efficiency to be no greater than around 53% (see Fig. 2.1). Figure 2.1 postulates an alternate, more practical limit on the maximum aerodynamic efficiency potential of modern HAWTs. Based on a representative (some form of weighted average) lift-to-drag ratio ( $C_l/C_d$ ) for entire turbine rotor, this practical limit is drawn as a  $C_P - \lambda$  curve (shown in blue for  $C_l/C_d = 100$ ) in Fig. 2.1.  $C_P$  is the non-dimensional power (Betz limit is  $C_P = 0.593$ ) and  $\lambda$  is the ratio of blade tip speed to freestream wind speed.

Maximum  $C_P$  of modern utility-scale HAWT's is only a few percentage points short of this practical limit. A good portion of this shortfall is due to aerodynamic losses in blade root region. Rotor blades in the root region (approximately bottom 25% of a rotor) is designed to withstand blade root bending moments. For structural integrity, relatively thick (high thickness-to-chord ratio) airfoils are chosen in the root region, which are aerodynamically poor. Flow separation in the root region causes span-wise (cross) flow, which deteriorates the aerodynamic performance of the outboard blade sections as well. Blade thickness, twist, and chord in the root region are limited by structural, manufacturing, and transportation limitations. A systematic diagnostic study by Sharma [31] has revealed that these constraints reduce turbine aerodynamic efficiency by about 5%. In this paper, we present a novel turbine concept to mitigate these root losses.

Utility scale turbines are deployed in clusters called wind farms. It is now recognized by the wind energy community that these turbines cannot be studied and/or optimized as

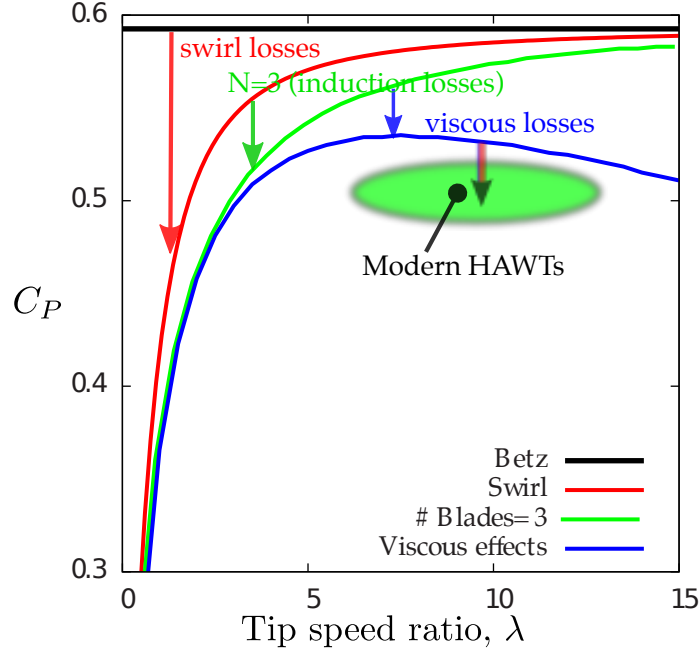


Figure 2.1: Maximum possible  $C_P$  with various approximations (Selvaraj et al. [4]).

if operating in isolation. Aerodynamic interaction between turbines in wind farms results in significant energy loss that ranges anywhere between 8-40% [32]. The primary mechanism of this energy loss is ingestion (by downstream turbines) of reduced-momentum air present in the wakes of upstream turbines. The range of this loss is exceptionally wide because of its strong dependence on farm location, layout (micro-siting), and atmospheric stability. Highest losses have been observed in offshore turbines when turbine rows are aligned with wind direction, are closely spaced, and when atmospheric flow is stably stratified [28, 29]). In comparison to the large body of work devoted to measuring and predicting wake losses, relatively little research has focused on reducing wake losses. For HAWTs, Corten and Lindenburg [30] have developed a method of farm control in which windward turbines are deliberately yawed (skewed) with respect to wind direction. The concept is to use the lateral force (generated by deliberate yawing of windward turbines) to divert the flow away from downstream turbines. The degree of yaw is determined based on wind and turbine row alignment.

With the wind energy industry fixated on single-rotor HAWT designs, primarily from cost considerations, multi-stage designs (e.g., dual-rotor turbines, DRWTs) have received little at-

tention. Multi-stage turbomachines are widely used in the gas turbine industry, where fuel has a price and hence, efficiency is prime. “Fuel” in wind turbines is supposedly free. Therefore, cost of electricity production, rather than efficiency, drives current turbine designs. As we approach the inevitability of having to produce most of our energy sustainably, with wind playing a substantial role in this quest, we will run out of sites (land or sea) where we can realistically install turbines [33]. The focus has to therefore shift towards efficient turbine and farm designs that extract highest power per square meter of surface area.

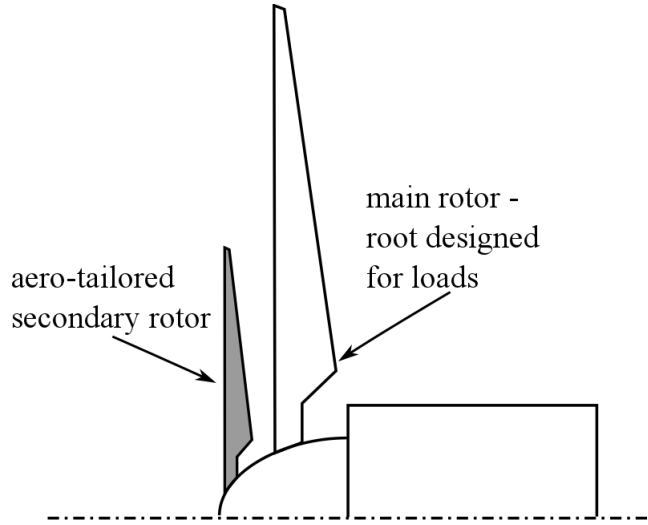


Figure 2.2: A schematic of the proposed dual-rotor concept.

Multi-rotor turbines can surpass the Betz limit (applicable only for single rotor wind turbines, SRWTs). The Rankine-Froude momentum theory, used to compute the Betz limit, was extended to study multi-rotor turbines by Newman [5]. Newman [5] calculated the maximum  $C_P$  of an equal-size DRWT to be 0.64, an 8% improvement over the Betz limit. Further addition of rotor stages gives diminishing returns. It is because of the added cost (rotor blades are the costliest part of a turbine) and the complexity (additional drivetrain, gearbox, etc.) that multi-rotor turbines are not widely used.

Jung et al. [34] numerically investigated the performance of a 30 kW counter-rotating DRWT and calculated optimum values for axial separation between primary and secondary rotors, and secondary rotor size. Lee et al. [35, 36] investigated effects of design parameters such as combination of pitch angles, rotating speed ratio, and radius ratio (between primary and



secondary rotors) on a DRWT. They found that maximum  $C_P$  occurs when front rotor size was chosen to be 80% of the second rotor. Kumar et al. [37] compared aerodynamic performances of DRWT against conventional, single-rotor HAWTs using CFD. A few DRWT prototypes have also been built and tested. Windpower Engineering & Development has developed a co-axial, twin-rotor turbine with the objective of harvesting more energy at lower wind speeds. They use two identical rotors connected by one shaft to a variable-speed generator. Enercon also has a patent [38] on a dual-rotor concept similar to the one proposed here, however it is focused on growing rotor radius rather than reducing losses.

A dual-rotor turbine concept (see Fig. 2.2) is proposed and investigated here. In this dual-rotor concept, a smaller, aerodynamically tailored, secondary co-axial rotor is placed ahead of the main rotor. None of the DRWT articles referenced above focus on what we are targeting with the proposed DRWT concept. Our goals are: (1) reduce root losses, and (2) reduce wake losses in a wind farm through enhanced wake mixing. The first goal targets improving isolated turbine efficiency through the use of aerodynamically optimized secondary rotor. The second goal targets efficiency improvement at wind-farm scale by (a) tailoring rotor wake shear, and (b) by exploiting dynamic interaction between vortices from main and secondary rotors of a DRWT.

## 2.2 Numerical Methods

Wind turbine and wind farm aerodynamics can be modeled with a spectrum of tools that vary considerably in fidelity and computational complexity (cost). Analytical [9, 39] and semi-analytical models [40], parabolic wake models [41], Reynolds Averaged Navier-Stokes (RANS) simulations [42], and Large Eddy Simulations (LES), all play different, yet necessary roles in turbine/farm analysis and design. Vermeer [10] and Sanderse [11] provide excellent reviews of various numerical methods available to study wind turbine and wind farm aerodynamics.

Two numerical models are used to analyze aerodynamics of DRWTs. Reynolds Averaged Navier Stokes (RANS) simulations with a generalized actuator disk parameterization of turbine rotors are performed to carry out preliminary design iterations towards optimizing aerodynamic performance. The optimized DRWT turbine is analyzed with a Large Eddy Simulations (LES)

model to investigate turbine wake evolution and compare it with that of a SRWT.

### 2.2.1 Rotor Parameterization using Actuator Disk/Line/Surface Models

Numerical modeling of wind turbine/farm aerodynamics can be classified into two categories based on whether or not rotor geometry is resolved. When the relevant length scale in the problem is smaller or comparable to blade chord (e.g., in dynamic load computations, or very near wake calculations), resolving blade geometry is essential. Vijaykumar et al. [19] and Lavelly et al. [20] present recent results from the Cyber wind facility at Penn State. They insist that resolving the flow near the blades is necessary for evaluating fatigue loads. They promote the use of blade-resolved URANS-LES calculations. However, in investigations of turbine wake evolution or wind farm aerodynamics, resolving rotor blades is arguably unnecessary. The effect of rotors on wake flows in such simulations is represented through sources in the momentum equation. This source representation can be in the form of disk (actuator disk), line (actuator line), or surface (actuator surface). Sørensen [43] and Mikkelsen [12] nicely summarize these methods. Porté-Agel et al. [15] and Wu and Porté-Agel [44] evaluated relative accuracy of three different actuator representations of turbine rotors in CFD and demonstrated the importance of including in-plane rotor forces with these models.

### 2.2.2 Reynolds Averaged Navier Stokes (RANS) Simulations

A generalized actuator disk model is implemented in OpenFOAM to analyze HAWT aerodynamics. OpenFOAM is essentially a group of C++ libraries used to create solvers. The SimpleFOAM solver (a part of OpenFOAM software suite) is used in the present study. SimpleFOAM solves the incompressible RANS equations,

$$\frac{\partial \bar{u}_i}{\partial x_i} = 0, \text{ and,} \quad (2.1)$$

$$\bar{u}_j \frac{\partial \bar{u}_i}{\partial x_j} = -\frac{1}{\rho} \frac{\partial \bar{p}}{\partial x_i} + \nu \frac{\partial^2 \bar{u}_i}{\partial x_j^2} - \frac{\partial \overline{u'_i u'_j}}{\partial x_j} + \frac{f_i}{\rho}, \quad (2.2)$$

where the Reynolds stress tensor,  $\overline{u'_i u'_j}$  is modeled using eddy (“turbulent”) viscosity as  $\nu_t \partial \bar{u}_i / \partial x_j$ . Turbulent viscosity,  $\nu_t$  is obtained using turbulent kinetic energy,  $k$  and dissipation,  $\epsilon$ , which are themselves obtained by solving a transport equation for each. The term  $f_i$  represents body

force per unit volume and is obtained using airfoil polars and local flow velocity. The force,  $f_i$  is distributed over a volume and a Gaussian distribution is applied along the flow direction following Mikkelsen [12]. This model has been previously validated against experimental data as well as the Blade Element Momentum (BEM) theory solutions for single-rotor turbines [4]; sample validation results are shown in Fig. 2.3.

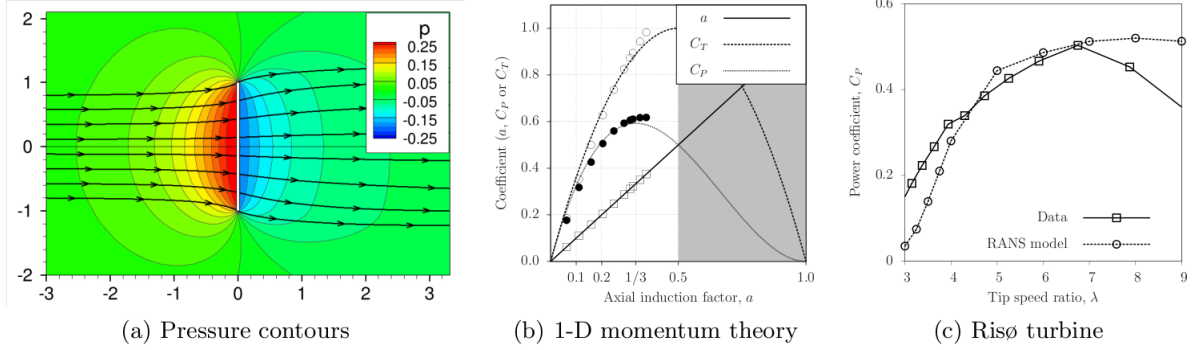


Figure 2.3: RANS simulation results including validation against analytical (b) and experimental (c) data [2]

### 2.2.3 Large Eddy Simulations

Modeling wind turbine and wind farm aerodynamics using LES has received a lot of research attention in recent years (see e.g., [15, 44, 13, 14, 16]). The Simulator for Offshore Wind Farm Application (SOWFA) [18, 3] software is used here. In this LES model, spatially filtered, incompressible forms of continuity and Navier-Stokes equations are solved using spatial and temporal discretization. Spatial filtering introduces unresolved, sub-filter scale (also called sub-grid scale or SGS) stresses, which have to be modeled. The width of the spatial filter is taken to be the grid-filter width given by  $\Delta = (\Delta_x \Delta_y \Delta_z)^{1/3}$ . The actuator line model (ALM) is used for rotor parameterization. Denoting spatially-filtered quantities by  $(\sim)$ , the governing

fluid flow equations are

$$\begin{aligned}
\frac{\partial \tilde{u}_i}{\partial x_i} &= 0, \\
\frac{\partial \tilde{u}_i}{\partial t} + \tilde{u}_j \left( \frac{\partial \tilde{u}_i}{\partial x_j} - \frac{\partial \tilde{u}_j}{\partial x_i} \right) &= - \underbrace{\frac{\partial \tilde{p}^*}{\partial x_i}}_{\text{turbine force}} - \underbrace{\frac{\partial \tau_{ij}}{\partial x_j}}_{\text{driving pressure}} + \nu \frac{\partial^2 \tilde{u}_i}{\partial x_j^2} \\
&\quad + \underbrace{\delta_{i3} g_0 (\tilde{\theta} - \langle \tilde{\theta} \rangle) / \theta_0}_{\text{buoyancy force}} + \underbrace{F_c \epsilon_{ij3} \tilde{u}_j}_{\text{coriolis force}}, \\
\frac{\partial \tilde{\theta}}{\partial t} + \tilde{u}_j \frac{\partial \tilde{\theta}}{\partial x_j} &= - \frac{\partial q_j}{\partial x_j} + \alpha \frac{\partial^2 \tilde{\theta}}{\partial x_j^2},
\end{aligned}$$

where,  $\tilde{p}^* = \tilde{p}/\rho_0 + \tilde{u}_i \tilde{u}_j / 2$  is the modified kinematic pressure,  $\tau_{ij} = \widetilde{u_i u_j} - \tilde{u}_i \tilde{u}_j$ , is sub-grid scale (SGS) stress tensor, and  $q_j = \widetilde{u_j \theta} - \tilde{u}_j \tilde{\theta}$  is SGS heat flux.  $f_i$  is momentum source to model forces exerted by turbine blades,  $\delta_{i1} F_P$  is pressure gradient to drive flow,  $\theta$  is potential temperature and  $\alpha$  is thermal diffusivity of the fluid. The deviatoric part of the SGS stress tensor,  $\tau_{ij}$  is typically modeled using an eddy-viscosity model,  $\tau_{ij} - 1/3 \delta_{ij} \tau_{kk} = -2\nu_{sgs} \widetilde{S}_{ij}$  and the SGS heat flux with an eddy-diffusivity model  $q_j = \widetilde{u_j \theta} - \tilde{u}_j \tilde{\theta} = -(\nu_{sgs} / Pr_{sgs}) \partial \tilde{\theta} / \partial x_j$ , where,  $\widetilde{S}_{ij} = 1/2 (\partial \tilde{u}_i / \partial x_j + \partial \tilde{u}_j / \partial x_i)$  is the resolved strain-rate tensor and  $Pr_{sgs}$  is the SGS Prandtl number. The mixing-length model by Smagorinsky [45],  $\nu_{sgs} = (C_S \Delta)^2 |\tilde{S}|$  is used to model  $\nu_{sgs}$ .

### 2.3 Dual-Rotor Simulations

The RANS method described in the previous section can be directly used to simulate dual-rotor wind turbine aerodynamics. The two rotors of a DRWT are modeled as two different, independent single-rotor turbines. It should be borne in mind that the two rotors of a DRWT are in close proximity, with a consequence that the potential field (due to finite blade thickness) of one rotor can affect the other. Stagnation pressure created near the leading and trailing edges of the main rotor, for example, can influence the aerodynamics of the secondary rotor. Such potential field interaction is not modeled here due to parameterization of rotors by actuator disk/line methods. While the potential field interaction cannot be completely ignored, we believe that a conceptual evaluation of the DRWT concept, such as proposed here, can be conducted with this simplification. Also, hub/nacelle geometry as well as turbine tower are

not modeled in these simulations. The effect of hub/nacelle on flow in the root region is not negligible, but is ignored in the present simulations to avoid confounding effects. The simulations assume axisymmetric flow and the CFD domain is therefore only 1 cell thick in the circumferential direction. The domain extends 10 rotor radii upstream and downstream as well as in the radial direction. The average number of cells for these simulations is 22 K.

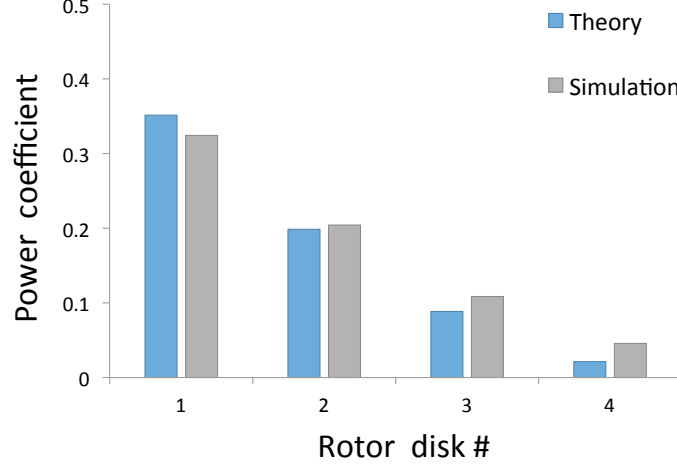


Figure 2.4: Comparison of numerically predicted and analytically evaluated (by Newman [5])  $C_P$ .

The ability of the RANS model to simulate multiple rotors is first verified for a canonical case by comparing against analytical results for a four, equal-size and uniformly loaded rotors (disks) by Newman [5]. The simulation is run by specifying the thrust coefficient for each rotor disk for maximum  $C_P$  for the entire turbine. Figure 2.4 compares CFD predicted  $C_P$  with analytical results. Fair agreement is observed between theory and simulations although the simulations in general predict higher power for downstream disks (#3 & #4) and lower power for upstream disks (#1 & #2). This is perhaps because of the turbulent mixing present in the simulations which reduces the wake deficit into the downstream turbines. The analytical results ignore wake mixing. Comparisons were also made for two-disk and three-disk turbines with similar accuracy.

### 2.3.1 Rotor Design

Preliminary design of the secondary rotor of a DRWT is carried out using an inverse design approach based on the blade element momentum theory. This approach is similar to one of the approaches used in PROPID [46, 47]. For design purpose, the secondary rotor is assumed to be operating in isolation (i.e., the effect of the primary rotor is ignored). The secondary rotor blades are designed with the DU96 airfoil, which is a high lift-to-drag ratio airfoil typically used for designing tip sections of main rotor blades. An aerodynamically optimum (for an isolated rotor) design is sought. Therefore, uniform axial induction,  $a = 1/3$  and uniform lift coefficient,  $C_l = 0.81$  (corresponding to the  $C_l$  value where maximum lift-to-drag ratio,  $C_l/C_d$  occurs) are prescribed. The inverse design approach then yields radial distributions of blade chord and twist (see Fig. 2.5). The lengths are normalized by the secondary rotor tip radius in the figure.

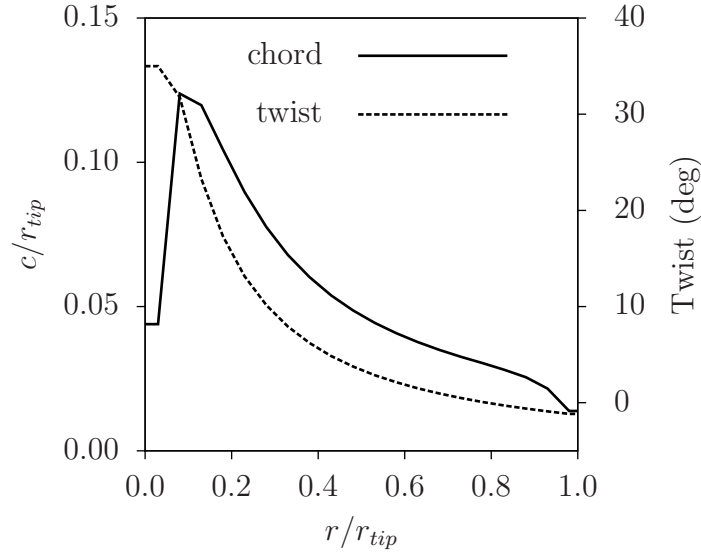


Figure 2.5: Radial distributions of secondary rotor blade chord and twist.

The main rotor is chosen to be that of the conceptual 5 MW offshore NREL turbine [48]. These blade designs remain non-dimensionally unchanged and the optimization study, described in the next section, focuses on identifying the aerodynamically optimum physical size of the secondary rotor and the separation distance between the two rotors.

### 2.3.2 Optimization Study

The RANS modeling approach with an actuator disk representation of a turbine rotor (see Sec. 2.2) is used to carry out parametric sweeps as part of an optimization study. The objective is to identify a design that gives highest  $C_P$  at one operating point (defined by specifying the tip speed ratios of the two rotors). The results presented here focus on a counter-rotating design (i.e., the two rotors rotate in opposite directions). Simulations with co-rotating turbine designs gave similar but slightly less efficient designs. The tip speed ratio of the main rotor is kept fixed at 7.55 and blade pitch of 0.0, which correspond to the maximum efficiency point of the main rotor. Three parameters are varied; these are: (1) the secondary rotor diameter, (2) the axial spacing between the main and secondary rotors, and (3) the tip speed ratio of the secondary rotor. Two 2-D parametric sweeps are carried out.

In the first parametric sweep, the secondary rotor size and tip speed ratio are varied while holding fixed the axial spacing between the main and secondary rotors (at  $0.5 \times$  main rotor tip radius). Figure 2.6 shows some results from this study. Since the design of the main rotor is held fixed,  $C_P$  does not monotonically increase with increasing secondary rotor size. In fact, the DRWT design shows a penalty for several combinations of secondary rotor size and tip speed ratio. High penalty at large secondary rotor size and tip speed ratios is because of the secondary rotor operating too far off from its design tip speed ratio. An island of relatively large increase in  $C_P$  is found centered approximated around secondary rotor tip radius of  $0.25 (\times$  main rotor tip radius) and tip speed ratio of 6.

In the second parametric sweep, the axial spacing and the secondary rotor tip speed ratio are varied while holding the secondary rotor tip radius at the optimum value of  $0.25 (\times$  main rotor tip radius) found in the first parametric sweep. Results from this parametric study are shown in Fig. 2.7. A net benefit is observed for a wide range of parametric values. Figure 2.7 (b) suggests that a separation distance of around  $0.2 \times$  main rotor radius would give the largest improvement in  $C_P$  over a single-rotor HAWT.

The RANS based optimization study suggest that an increase in  $C_P$  of about 0.035, which is about a 7% increase in aerodynamic efficiency, is attainable with the DRWT concept. This

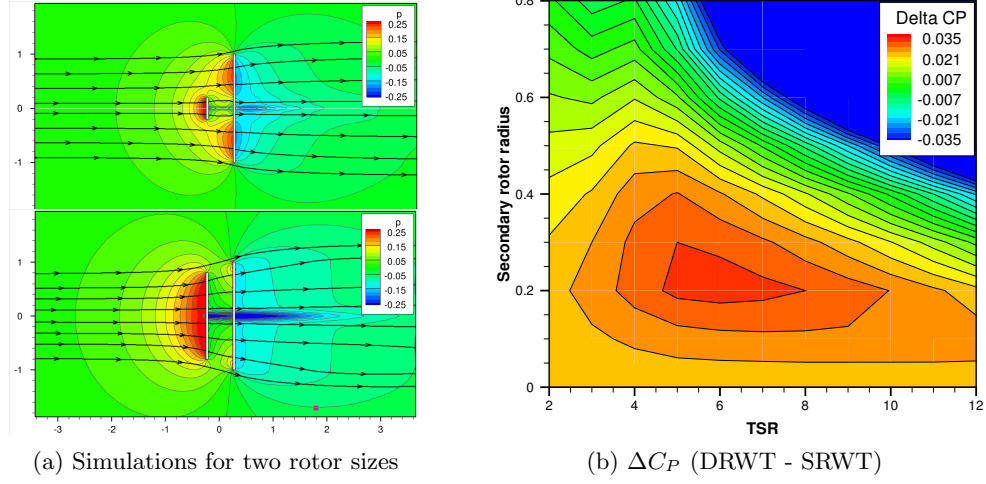


Figure 2.6: RANS simulation results: (a) pressure contours and streamlines for two secondary rotor sizes, and (b) difference in aerodynamic power coefficient,  $\Delta C_P = C_{P\text{DRWT}} - C_{P\text{SRWT}}$  due to the addition of a secondary rotor.

improvement is primarily due to efficient extraction of energy flowing near the hub of the main rotor, but in part also due to the addition of another energy extracting device. Note also that this improvement is solely on isolated rotor basis. We anticipate that the DRWT concept can also be used to mitigate wake losses, which can improve wind farm efficiency. To investigate DRWT wake behaviour, we use the LES methodology described in Sec. 2.2. For the LES simulations a nearly optimal secondary rotor design: tip radius =  $0.3 \times$  main rotor tip radius, axial separation =  $0.2 \times$  main rotor tip radius, and tip speed ratio,  $\lambda = 6$  is selected.

### 2.3.3 Large Eddy Simulations

Large eddy simulations are carried out for the optimum DRWT configuration identified through the optimization study described in the previous section. A SRWT simulation with only the main rotor of the optimized DRWT configuration is also performed to enable a comparative study. Simulations are carried out in a computational domain that is 6D long, 4D wide and 4D tall, where D is the main rotor diameter. Figure 2.8 shows the computational domain dimensions and the relative placement of the turbine. Only the rotors of the turbine are simulated; the hub/nacelle and the tower were ignored in these simulations. OpenFOAM's blockMesh utility is used to create a structured mesh with  $600 \times 200 \times 200$  cells. The mesh is



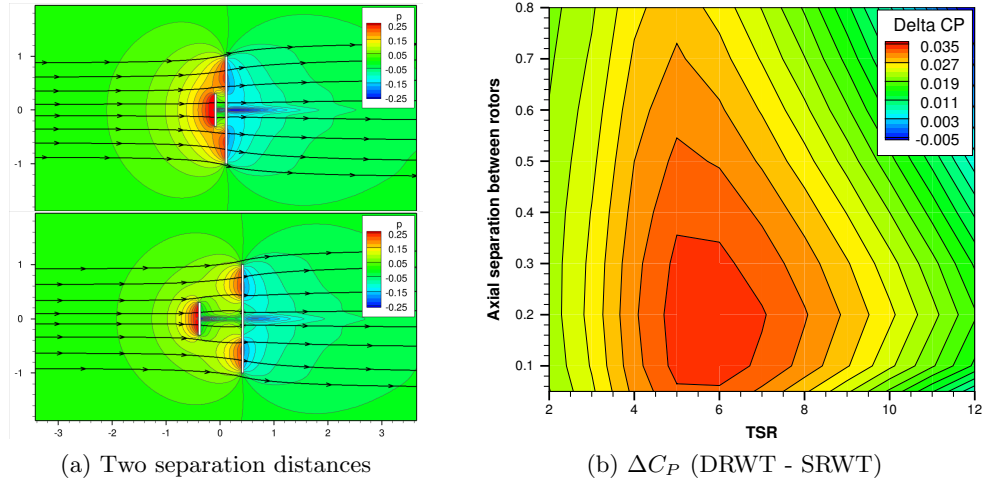


Figure 2.7: RANS simulation results: (a) pressure contours and streamlines for two axial separation distances, and (b) difference in aerodynamic power coefficient,  $\Delta C_P = C_{P\text{DRWT}} - C_{P\text{SRWT}}$  due to the addition of a secondary rotor.

clustered near the turbine rotors and the grid gradually stretched in the axial direction away from the rotors.

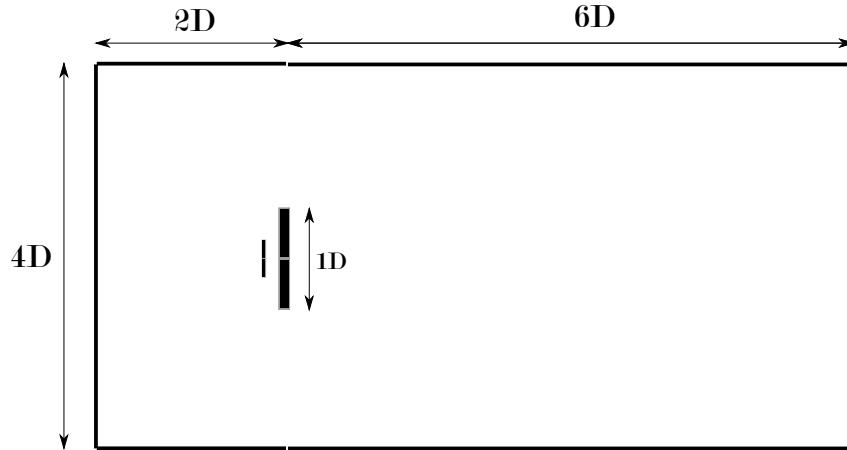


Figure 2.8: Domain size for the LES runs.

Periodic boundary conditions are used on all side boundaries, essentially simulating an infinite planar array of turbines rather than a single turbine. This should be borne in mind because far downstream from the array, the neighboring turbines will influence the wake evolution. Inflow and outflow boundary conditions are applied at the inlet and outlet boundaries.

The domain is decomposed spatially using the *scotch* algorithm and simulations are performed in parallel using SOWFA. Each simulation is run for a total of 200 seconds of physical time with a constant inflow wind speed of 8 m/s. Approximating the average axial induction factor to be 0.33, the turbine wake convects downstream a distance of about 8.5 main rotor diameters in 200 seconds, so it would completely sweep the computational domain. Each simulations takes about 750 CPU hours running in parallel on 32 Intel Xeon E5-2680 processors. The E5-2680 is a 64 bit processor with 8 cores and has a clock speed of 2.7 GHz.

Figure 2.9 shows a snapshot in time of iso-surfaces of Q-criterion. The tip vortices from both the primary and secondary rotors are clearly visible in Fig. 2.9. The DRWT produces about 4.55% additional power compared to the SRWT. The secondary rotor of the DRWT produces about 6.4% of the total power. Since the main rotor operates in partial wake of the secondary rotor, it produces slightly less (98.26%) power in the DRWT configuration than in the SRWT configuration.

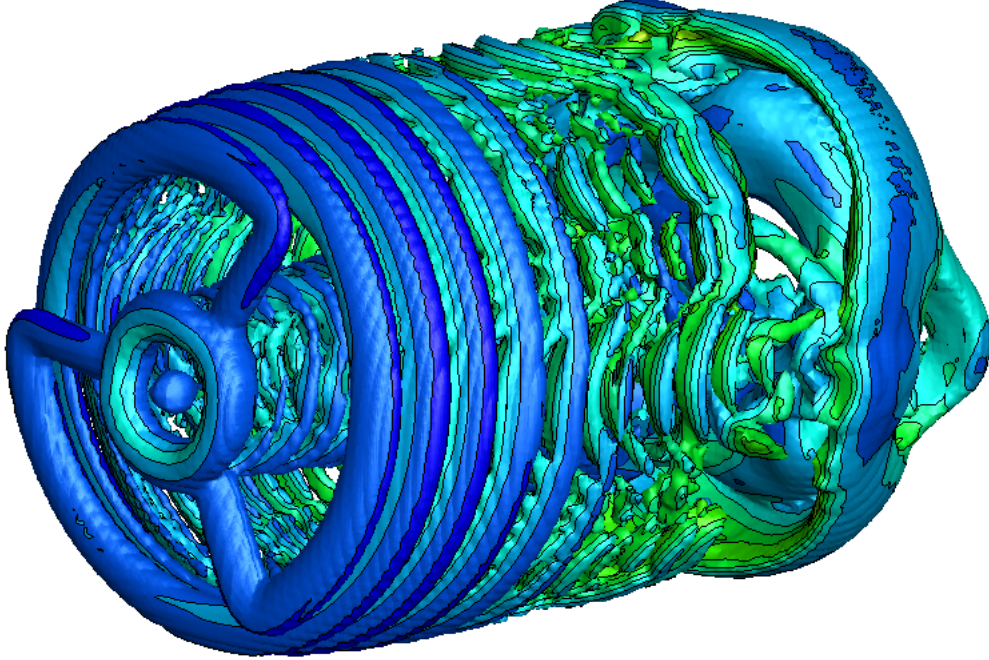


Figure 2.9: A snapshot of iso-surfaces of Q-criterion from the DRWT LES simulation.

To compare DRWT and SRWT wake evolution, the field variables are averaged over 50 secondary from  $t = 150$  to 200 seconds. Since the turbine is abruptly started at  $t = 0$ , the

initial data contains transients which are allowed to pass through the domain before starting data averaging. Since the incoming flow is uniform, the results can be azimuthally averaged and analyzed as functions of radius and downstream distance. Figure 2.10 compares the time and space (around the azimuth) averaged axial component of wind speed in the wakes of the DRWT and SRWT turbines. The velocities are compared at four different distances downstream of the turbines: 1-, 2-, 3-, and 4-main rotor diameters. The larger velocity deficit near the hub ( $r/r_{tip} < 0.4$ ) in the case of the DRWT is due to the secondary rotor of the DRWT efficiently extracting energy from the air flowing through that region. The DRWT results also show high radial mixing in the secondary rotor slipstream. However, little-to-no evidence of enhanced radial momentum transport is observed near  $r = r_{tip}$  in these results. Figure 2.11 compares radial variation of azimuthally averaged turbulence intensity at four downstream distances. Higher turbulence intensity near the hub for the DRWT is consistent with the observed higher velocity deficit. Further analyses and comparisons will be carried out in the near future for turbines operating in an atmospheric boundary layer, which has a strong influence on evolution of turbine wakes.

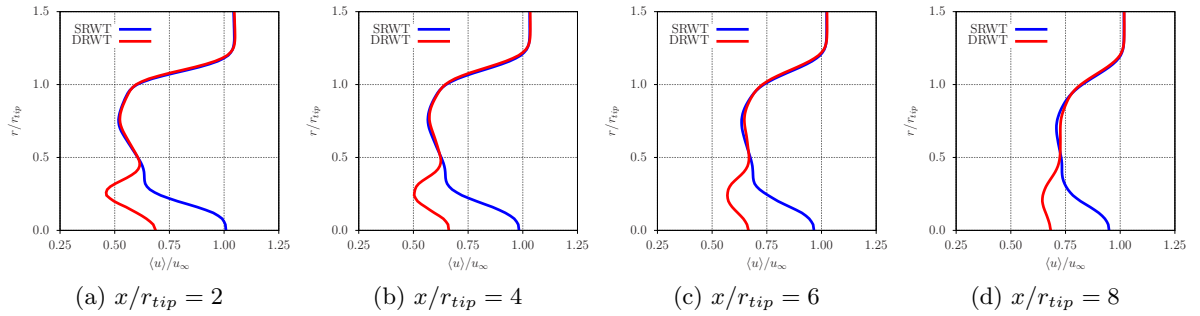


Figure 2.10: Radial wake variation comparisons between a single-rotor (HAWT) and a dual-rotor (DRWT) turbine at four downstream distances.

## 2.4 Momentum Entrainment with Atmospheric Boundary Layer

### 2.4.1 Computational Setup

This section was adapted from a paper published in the journal [Energies](#) in July 2016. [49]

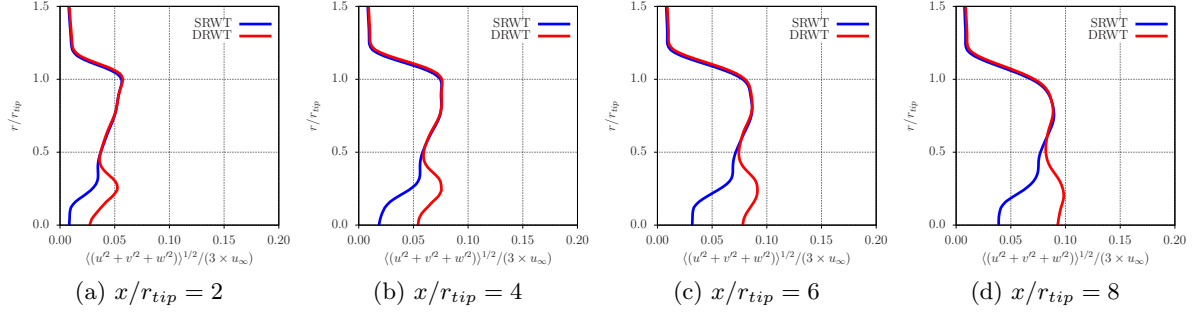


Figure 2.11: Radial turbulence intensity variation comparisons between a single-rotor (SRWT) and a dual-rotor (DRWT) turbine at four downstream distances.

A two-step approach is used for the numerical predictions. The atmospheric boundary layer (ABL) flow is computed first on one grid and then the flow around the wind turbine is computed on another, more refined grid. Investigations are conducted for uniform inflow and two atmospheric stability conditions: (1) neutral, and (2) stable. In the simulations presented here, the wind blows from the South-West; the wind direction is 240 degrees (measured clockwise) from the North such that the West and the South boundaries of the computational domains are inlet while the East and the North boundaries are outlet (see Fig. 2.12).

Three coordinate systems are utilized in this study. A frame of reference attached to the ground, described by unit vectors  $\hat{e}_{\tilde{x}}, \hat{e}_{\tilde{y}}, \hat{e}_{\tilde{z}}$ , is utilized for the CFD calculations. The freestream wind blows at an angle  $\phi = 30^\circ$  to  $\hat{e}_{\tilde{x}}$ . A new coordinate system with its  $x$ -axis aligned with the flow direction is therefore defined by the unit vectors  $\hat{e}_x, \hat{e}_y, \hat{e}_z$ , where  $\hat{e}_{\tilde{x}} \cdot \hat{e}_x = \cos(30^\circ)$ . Lastly, a cylindrical coordinate system, with its axis aligned with  $\hat{e}_x$  is used to compute momentum and energy entrainment into the turbine wake layer (see Section 2.4.2). This coordinate system is defined by the unit vectors  $\hat{e}_r, \hat{e}_\theta, \hat{e}_x$ . The details are provided in Appendix A.

The atmospheric boundary layer (ABL) is developed in a computational domain by performing “precursor” simulations. A precursor calculation simulates an infinitely long domain in the horizontal directions (the Earth surface) by using cyclic boundary conditions. The intent here is to create steady state ABLs under different stability conditions and not to capture the transient effect caused by the diurnal or seasonal variation of the ABL. Wall models by

Moeng [50] are used to estimate the surface stresses (viscous and SGS) and temperature flux at the bottom boundary. The aerodynamic surface roughness is  $h_0 = 0.1$  m, which is a typical value for a terrain with low crops and occasional large obstacles [51]. The top boundary is at 1 km, which is many diameters away from the turbine. The velocity normal to the boundary is set to zero. The pressure boundary condition is zero-gradient and temperature gradient is specified to be 0.003 K/m at the top boundary. Temperature inversion is applied in the domain with the width of 100 m. The temperature at the bottom of the inversion layer is 300 K and at its top is 308 K. Above the inversion layer, the temperature gradient is 0.003 K/m. The inlet is on the South and the West boundaries and a zero pressure gradient boundary condition to simulate outlet conditions is applied on the North and the East boundaries.

Since the objective of the precursor simulations is to establish a fully-developed atmospheric boundary layer flow, wind turbines are excluded from these simulations. The flow is driven by a pressure gradient which is adjusted to achieve the desired flow speed at the turbine hub height. Random perturbations are applied to the flow initially to trip the boundary layer. Precursor simulations are carried out for a long enough time (5 hours of simulation time) to achieve statistical stationarity. With the mean flow speed at the turbine hub height set at 8 m/s, it takes about 9 minutes of simulation time for the flow to cross the computational domain from the inlet to the exit. In 5 hours of simulation time, the flow cycles the domain approximately 34 times, which is sufficient to achieve a fully developed ABL.

Time accurate flow data sampling is initiated at the inlet boundaries after reaching a statistical stationary state (at  $t = 5.0$  hours). Sampling is performed for 1,000 seconds of simulation time, which is the total simulation time for the wind turbine calculations. This time-accurate flow data is prescribed as an inflow boundary condition in the wind turbine simulation. This is one approach to prescribe time-accurate inflow boundary conditions. Another approach is to use synthesized turbulence, where the time-accurate flow information can be constructed using analytical models of turbulence spectra (e.g., Kaimal, von Karman, etc.) [52]. Once statistical stationarity is reached (at  $t = 5.0$  hours), the entire flow field from the precursor simulation is also stored and used to initialize the flow in the wind turbine simulations.

Each wind turbine simulation starts at  $t = 5.0$  hours and a total of 1,000 seconds of

flow is simulated. The initial and inlet boundary conditions are prescribed using the precursor simulation data as described above. The computational domains for precursor and wind turbine simulations need not be identical. On the contrary, it is desirable to make the domain of the precursor calculation considerably larger than the domain for the wind turbine simulation to account for the length scale disparity between the physical phenomena of interest in these simulations. In the precursor simulations, the energy containing turbulent eddy size can be of the order of a kilometer (planetary boundary layer height), while in the wind turbine simulation, the flow physics of interest is turbine wake for which the relevant length scale is of the order of the turbine diameter ( $\sim 100$  m for utility scale turbines).

A shorter domain is used for wind turbine simulations in comparison with precursor simulations to allow for higher spatial resolution of the turbine wakes. As seen in Fig. 2.12, the precursor runs are performed on a computational domain with dimensions  $3 \text{ km} \times 3 \text{ km} \times 1 \text{ km}$ . The domain is discretized into  $288 \times 288 \times 100$  hexahedral cells. The precursor simulations are performed in parallel on 128 cores and each run takes about 50 hours of wall-clock time. The wind turbine runs are performed on a domain of size  $2.2 \text{ km} \times 1.5 \text{ km} \times 1 \text{ km}$  that is discretized into  $220 \times 150 \times 100$  hexahedral cells. Two levels of mesh refinement are used in the vicinity of- and downstream of the wind turbine. Each grid cell in a refinement block is split into half along each direction (i.e., it is divided into 8 cells). In the refined block, the cell size is 2.5 m in each direction. The final mesh has a total of about 14 M cells. The *blockMesh* utility in OpenFoam is used to generate the computational meshes. It takes approximately 120 hours of wall-clock time to simulate 1,000 seconds of flow in each wind turbine simulation using 128 cores in parallel. Figure 2.12 (b) shows the turbine location in the computational domain as well as the topology of the refinement zones.

LES simulations are carried out using the optimum DRWT identified in Rosenberg *et al.* [2]. The non-dimensional chord and twist distributions of the main and secondary rotors of the DRWT are shown in Fig. 2.5. The blade chord ( $c$ ) and radius ( $r$ ) are nondimensionalized by the respective rotor tip radii. To enable direct comparisons, simulations are also performed for a conventional single rotor wind turbine (SRWT), which is the conceptual NREL 5MW offshore reference turbine [48]. The NREL 5 MW turbine is used as the primary rotor of the DRWT.

### 2.4.2 Momentum Entrainment

Utility scale turbines in windfarms are typically installed in systematic arrangements (arrays). Wake losses in a windfarm are most severe when the wind direction is aligned with the turbine rows. In such extreme cases, it is meaningful to look into entrainment of high-momentum fluid into the turbine wake layer. For a very large, closely-packed turbine array, the turbine wake layer would be horizontal, stretching vertically from  $H - r_{tip}$  to  $H + r_{tip}$ , where  $H$  is the turbine hub height and  $r_{tip}$  is the rotor tip radius. For an isolated turbine analysis however, the turbine wake layer is cylindrical, co-axial with the rotor, and has the same diameter as that of the turbine rotor (see Fig. 2.13).

Turbulent transport of momentum from outside the turbine layer has been identified to be the dominant mechanism for re-energizing the flow in large wind turbine arrays [53]. Turbulent momentum flux through the cylindrical turbine wake layer (see Fig. 2.13), is analyzed to compute turbulent momentum and energy transport and investigate wake recharging. The present analysis is performed for a turbine wake layer that extends from the turbine rotor location to  $8D$  downstream. Time averaged velocity and Reynolds stress tensor ( $\overline{u'_i u'_j}$ ) are interpolated onto this cylindrical surface using the Tecplot 360 software ([www.tecplot.com](http://www.tecplot.com)).

Entrainment of high momentum fluid into this cylinder is induced by turbulent stresses, particularly the stress term  $\overline{u'_r u'_x}$ , where the subscript ‘ $r$ ’ denotes the radial component, the prime denotes a perturbation quantity, and the overline denotes a time-averaged quantity. A cylindrical coordinate system ( $\hat{e}_r, \hat{e}_\theta, \hat{e}_x$ ) with its axis aligned with the freestream flow direction  $\hat{e}_x$  is used (see Appendix A). Equation B.2 relates  $\overline{u'_r u'_x}$  to the Reynolds stress tensor computed in the ground frame of reference ( $\hat{e}_{\tilde{x}}, \hat{e}_{\tilde{y}}, \hat{e}_{\tilde{z}}$ ). Since  $\hat{e}_r$  points radially outward, a negative value of  $\overline{u'_r u'_x}$  implies transport *into* the cylinder (turbine wake layer).

Figure 2.14 (a-f) plot the Reynolds stress term  $\overline{u'_r u'_x}$  normalized by  $u_{\infty,h}^2$  on the unwrapped cylindrical surface that defines the turbine layer. The colormap in the figure is reversed to make intuitive sense - negative values indicate net flux into the cylinder. In the figure,  $\theta = 0^\circ$  corresponds to the 12 o’clock position and  $\pm 180^\circ$  correspond to the 6 o’clock position. It can be noticed that the highest value of  $-\overline{u'_r u'_x}$  is not at the 12 o’clock position but skewed about it.

This behavior has been noted previously by Wu and Porté Agel [54] although for the stress term  $\overline{u'_x u'_z}$ . A clear trend of increasing momentum entrainment with increasing ABL turbulence is seen in the figure for both SRWT and DRWT. The  $x$ -location where peak entrainment occurs varies both with atmospheric turbulence intensity and azimuthal location. The peak values occur closer to the turbine as inflow turbulence intensity increases (compare subplot ‘a’ with ‘b’ & ‘c’ of Fig. 2.14). This is because the incoming turbulence disintegrates the tip vortex system quickly. For ABL cases, peak  $-\overline{u'_r u'_x}$  occurs around 1 rotor diameter downstream of the turbine near the ground ( $\theta = \pm 180^\circ$ ), while near the 12 o’clock position, the peak values occur further downstream.

While there is a significant difference in the spatial distribution and magnitudes of  $\overline{u'_r u'_x}$  between the three inflow conditions considered, the differences between the SRWT and DRWT are subtle. The DRWT shows a higher level of momentum entrainment, especially for  $x > 5D$ . To calculate net entrainment from all around the cylinder,  $\overline{u'_r u'_x}$  is further averaged azimuthally. The azimuthal averaging operation is denoted by angle brackets, thus the quantity  $\langle \overline{u'_r u'_x} \rangle$  represents temporally and spatially averaged value of  $u'_r u'_x$ .  $\langle \overline{u'_r u'_x} \rangle$  multiplied by the circumference of the cylinder ( $2\pi r_{tip}$ ) is the turbulent momentum entrainment per unit length into the cylinder. Subplots (g-i) in Fig. 2.14 show the variation of  $\langle \overline{u'_r u'_x} \rangle$  (normalized by  $u_{\infty,h}^2$ ) with distance from the turbine rotor location. The  $y$ -axis is reversed in the plots as negative values imply positive entrainment. Variation is plotted on the same scale to contrast the mixing rates between the different inflow conditions. The neutral ABL case shows highest entrainment while the uniform inflow case shows the lowest entrainment. The increase in entrainment for the DRWT over the SRWT is also highest for the neutral ABL case and lowest (indeed there is a slight reduction) for the uniform inflow case. The plots for turbulent flux of kinetic energy ( $\overline{u_x} \times \overline{u'_r u'_x}$ ) are very similar to those for momentum flux and hence are not shown. The overall percentage change in turbulent flux of axial momentum and kinetic energy due to the DRWT are provided in Table 2.1.

A modest 3.29% increase in momentum entrainment is observed. The reader is reminded that in these simulations, the secondary rotor is operated at the tip speed ratio that gives maximum aerodynamic performance for *isolated* turbine operation in uniform inflow conditions.



No attempt is made here to optimize the secondary rotor design/operation to enhance wake mixing. Notwithstanding the sub-optimal design/operation, the DRWT still shows higher levels of entrainment than the SRWT for the two ABL cases. These results demonstrate that in a windfarm, the turbines operating in wake flow can benefit from enhanced entrainment provided by the DRWT. Additionally, the fact that the turbine operation and the geometry of the secondary rotor, can be optimized to actively target wake mixing, leaves potential for further improvement in windfarm efficiency from the DRWT technology.

Table 2.1: Percent change (DRWT-SRWT) in cumulative streamwise momentum and kinetic energy for the three inflow conditions.

Inflow condition	$\% \Delta(\overline{u'_r u'_x})$	$\% \Delta(\overline{u_x} \times \overline{u'_r u'_x})$
Uniform	-1.17%	-2.30%
Stable	+1.78%	+1.63%
Neutral	+3.29%	+2.54%

## 2.5 Conclusions

A new dual-rotor wind turbine (DRWT) concept is presented. The secondary rotor is smaller, axially aligned with the main rotor, and designed with high lift-to-drag ratio airfoils. A DRWT is designed using the NREL 5 MW turbine as the main rotor and the secondary rotor made out of the DU96 airfoil. Parametric sweeps using RANS simulations show that secondary rotor turbine size should be 25% of the main rotor and it should be axially separated from the main rotor by a distance of 0.2 times the main rotor radius. A net benefit of 7% in  $C_P$  is predicted by RANS calculations for the optimized DRWT design. Large eddy simulations for the optimized DRWT operating in uniform flow show a net increase in power generation of about 4.6%. Wake comparisons confirm efficient extraction of energy in the root region by the DRWT. However, increase in vertical entrainment of energy, which would reduce turbine wake losses, is not clearly observed in the simulations.

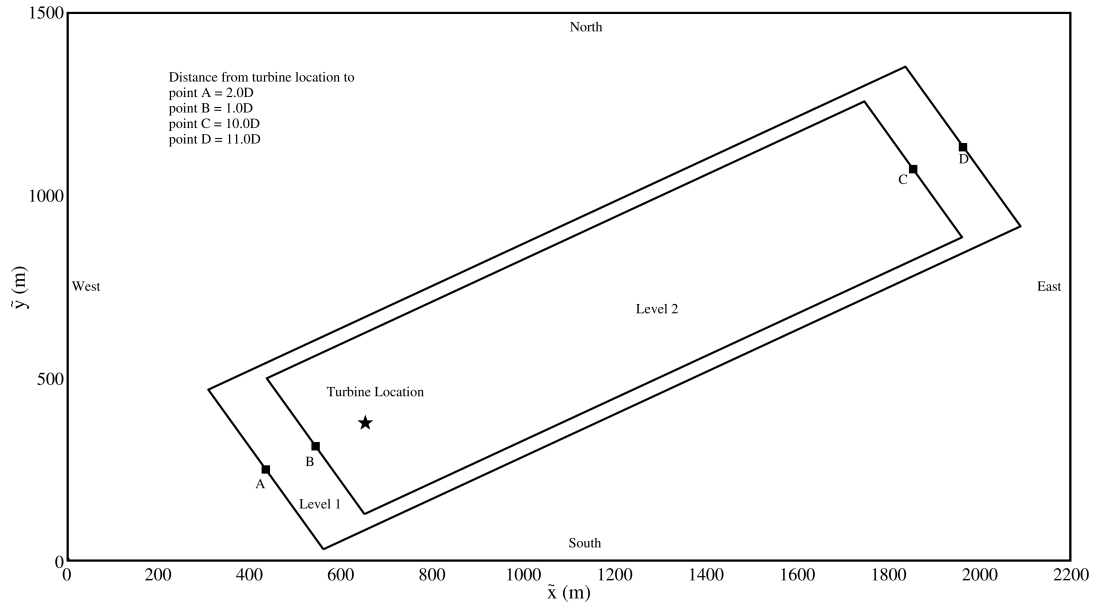
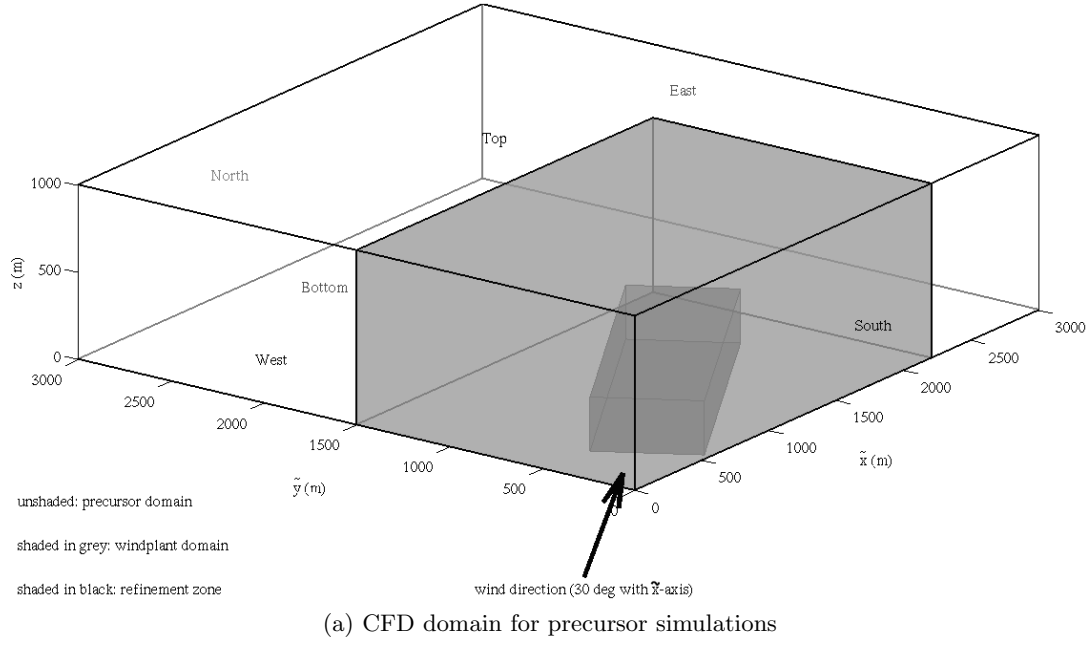


Figure 2.12: A schematic showing the computational domains for the atmospheric boundary layer (precursor) and the main (wind turbine) simulations. The entire box in (a) is the domain for precursor calculations; shaded are shows the smaller domain for wind turbine calculations. In (b), points A-D are lateral midpoints of the rectangular refinement zones.

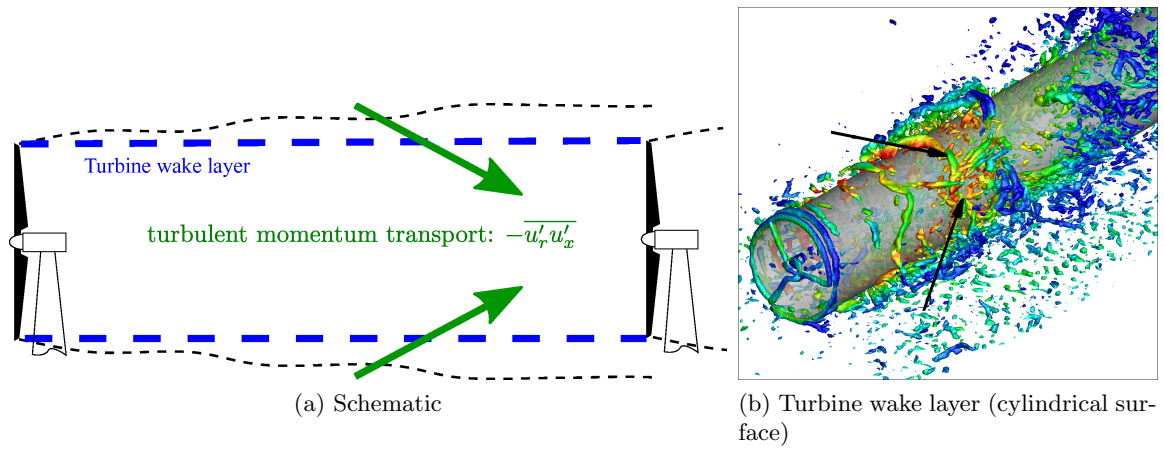


Figure 2.13: Investigation of turbulent momentum transport into the turbine wake layer: (a) a schematic and (b) cylindrical surface showing the turbine wake layer through which turbulent momentum flux is computed to quantify entrainment in turbine wake.

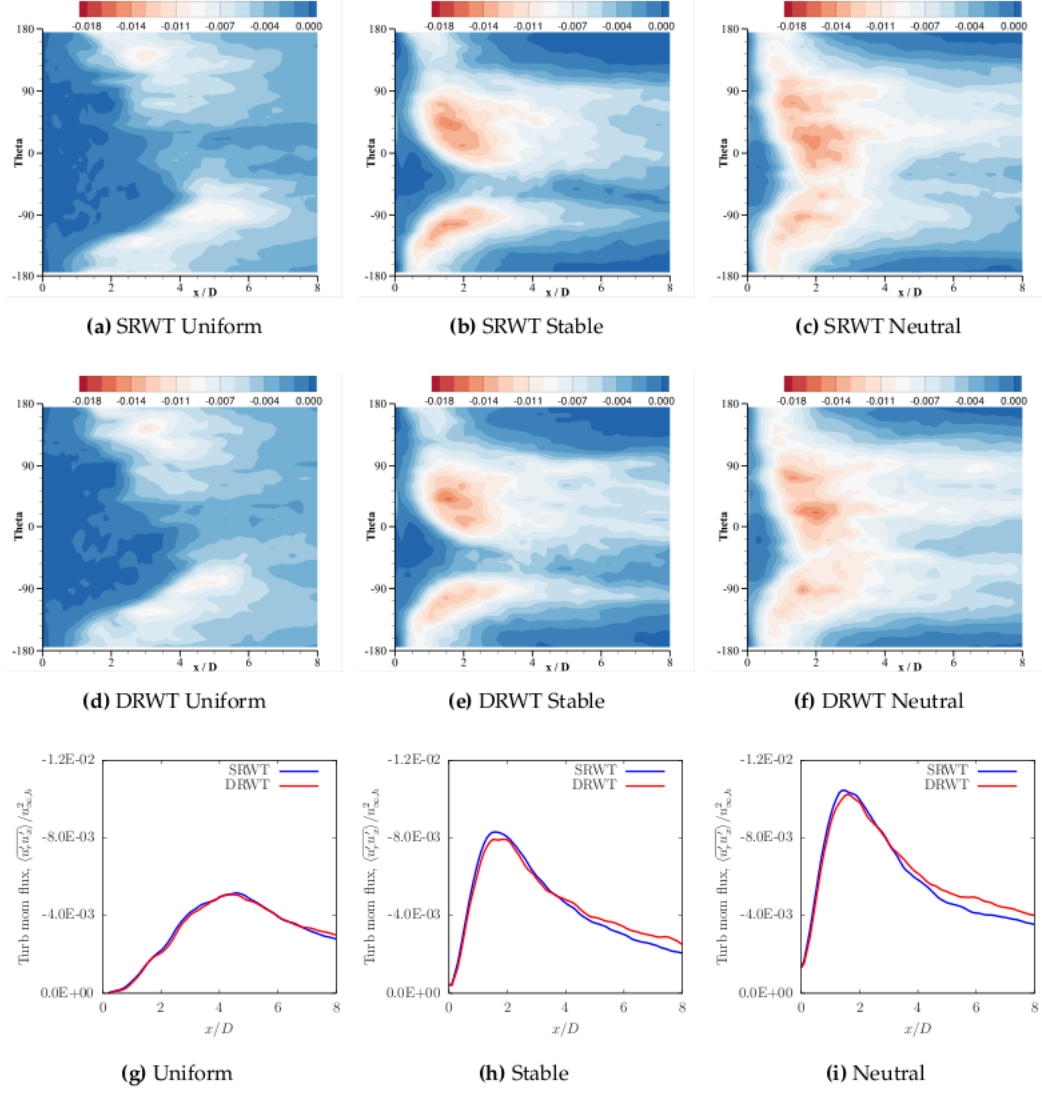


Figure 2.14: Radial transport of streamwise momentum into the turbine wake layer. Color contours show  $\overline{u'_r u'_x} / u_{\infty,h}^2$  on the cylindrical surface of Fig. 2.13 that has been cut at  $\theta = \pm 180^\circ$  and unwrapped.

### CHAPTER 3. A PRESCRIBED-WAKE VORTEX LATTICE METHOD FOR PRELIMINARY DESIGN OF CO-AXIAL, DUAL-ROTOR WIND TURBINES

This chapter was published in the [Journal of Solar Energy Engineering](#) in September 2016.[55]

Aaron Rosenberg and Anupam Sharma. A prescribed-wake vortex lattice method for preliminary design of co-axial, dual-rotor wind turbines. *Journal of Solar Energy Engineering*, 138(6):061002, 2016.

#### Abstract

This paper extends the prescribed wake vortex lattice/line method (VLM) to perform aerodynamic analysis and optimization of dual-rotor wind turbines (DRWTs). A DRWT turbine consists of a large, primary rotor placed coaxially behind a smaller, secondary rotor. The additional vortex system introduced by the secondary rotor of a DRWT is modeled while taking into account the singularities that occur when the trailing vortices from the secondary (upstream) rotor interact with the bound vortices of the main (downstream) rotor. Pseudo-steady assumption is invoked and averaging over multiple relative rotor positions is performed to account for the primary and secondary rotors operating at different rotational velocities. Our implementation of the VLM is first validated against experiments and blade element momentum theory results for a conventional, single rotor turbine. The solver is then verified against Reynolds Averaged Navier Stokes (RANS) CFD results for two DRWTs. Parametric sweeps are performed using the proposed VLM algorithm to optimize a DRWT design. The problem with the algorithm at high loading conditions is highlighted and a solution is proposed that uses RANS CFD results to calibrate the VLM model.

### 3.1 Introduction

Dual-rotor wind turbine (DRWT) technology (see Fig. 3.1) has recently been investigated [2, 49, 56, 34, 57] as a higher efficiency alternative to conventional, single-rotor wind turbines (SRWTs). The technology uses two coaxial rotors to harness energy from wind. The two rotors can have different or same diameters, and can rotate with the same rotational speed (e.g., if they are on the same shaft) or independent of each other. DRWTs have additional parameters compared to SRWTs, such as relative rotor sizes, rotation speeds, axial separation, etc. These parameters must be carefully selected to optimize the aerodynamic performance of a DRWT. Due to the large parametric space that needs to be explored, it is desirable to have a computationally inexpensive analysis method to provide preliminary design guidance.

Blade element momentum (BEM) theory based methods and vortex lattice/line methods have been used extensively in design and analysis of SRWTs. These methods have been modified to investigate DRWTs. Lee *et al.* [58] uses a modified BEM method to study the effects of design parameters on a counter-rotating wind turbine. This method assumes that second rotor operates completely inside the developed wake of the primary (main) rotor. Jung *et al.* [34] also uses a modified BEM method in which the wake from the front rotor is prescribed using experimental data. This allows for the second rotor to operate in the partial wake of the front rotor. A free-wake vortex lattice method has also been used successfully to study multi-rotor wind turbines [8, 59]. This has proven to be a relatively high fidelity method for simulating multi-rotor wind turbines, but it can be computationally expensive especially for design use where a large parametric space is required to be explored.

In this paper, we present a methodology to extend the prescribed-wake vortex lattice method to carry out preliminary aerodynamic analysis of DRWTs. This proposed method allows for a general analysis of DRWTs at a relatively low computational cost.

### 3.2 Vortex Lattice Method

The vortex lattice method is based on Prandtl's lifting line theory, which utilizes the laws of kinematics (Helmholtz vortex theorems) and dynamics (Kelvin's circulation theorem) of vortex

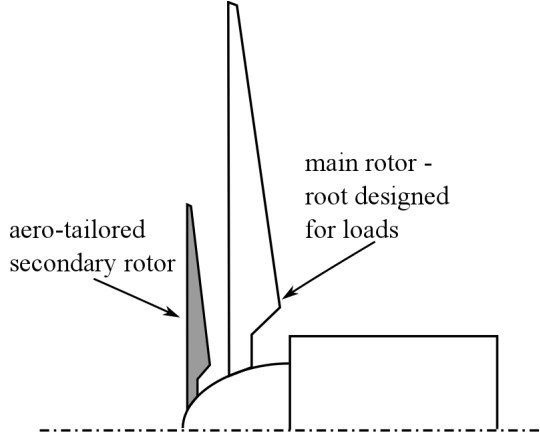


Figure 3.1: A schematic of the DRWT technology by Rosenberg *et al.* [2]

lines. Potential flow is assumed and rotor blades are replaced by blade-bound vorticity (lifting lines). The bound vorticity for a blade section (airfoil) can be concentrated at a point or distributed along the airfoil chord/camber line; vorticity and circulation are related by Stokes' theorem. Helmholtz vortex theorems necessitate the existence of a single free-trailing vortex sheet per blade. They also define the distribution of the trailing vorticity; the strength of each trailing vortex is equal to the change in circulation along the lifting line.

Velocity “induced” by vorticity is described by the Biot-Savart law. In an aircraft, the velocity induced on the wing by the trailing vortex sheet is referred to as “downwash”. This downwash is responsible for induced drag in finite-span wings. The same concept can be applied to wind turbine rotor blades (or propeller blades), where the trailing vortex sheet becomes helical due to blade rotation. Induction determines the local flow velocity and, given blade geometry and operation specifications, the local blade-relative flow velocity and angle of attack. With prior knowledge of sectional lift and drag polars ( $c_l - \alpha$  and  $c_d - \alpha$  curves), the local lift and drag can be computed. Finally, the Kutta-Jukowski theorem links the sectional lift to the bound circulation around a blade section. Using these theorems, an iterative procedure can be obtained to compute spanwise distribution of circulation (or blade-bound vorticity) on turbine rotor blades (see e.g., Refs. [60, 61]).

Based on the treatment of trailing vorticity, the vortex lattice method can be classified as either *free wake* or *prescribed (fixed) wake* [62]. In the free-wake approach, mutual induc-

tion between trailing vortex elements is permitted and hence the wake evolves with time; the wake structure can deform substantially over time. In the prescribed-wake approach, mutual induction is ignored and the prescribed trailing vortex structure stays intact. Subtle changes to the wake structure that do not change the wake helix topology, such as the helix pitch, Trefftz plane location, etc. are permitted in the prescribed-wake approach until convergence is reached. These changes are specified as functions of some overall integrated quantity such as rotor thrust or power coefficient.

While the free-wake approach is of higher fidelity, it is computationally expensive [62] and can suffer from robustness issues. The prescribed-wake approach, on the other hand, is relatively quick and robust, but can be inaccurate if the fixed wake structure is poorly specified. We choose the prescribed-wake approach here as the objective is to explore a large design space during preliminary design of DRWTs. For our purpose, efficiency and robustness are more important than fidelity as long as the methodology predicts correct design trends. The particular implementation presented in Refs. [61, 63, 64] is adopted in our prescribed-wake vortex lattice method solver with two major changes that are described below.

Chattot [64] assumes ‘wake equilibrium’ to relate computed turbine power coefficient,  $C_P$  with that given by the 1-D momentum theory to obtain axial induction factor,  $a$  using the relation  $C_P = 4a(1 - a)^2$ . This axial induction factor is then used to update the pitch of the trailing vortex helix in an iterative procedure until convergence is achieved. The problem with this approach is that axial induction is a multi-valued function of  $C_P$  (see Fig. 3.2). Typically, the solution corresponding to smaller axial induction factor is selected to set the helix pitch. While this strategy works for low-loading conditions, it is evident from Fig. 3.2 that this approach is incorrect for cases with high rotor disk loading. An alternative is to choose the turbine thrust force coefficient,  $C_T$  to calculate  $a$ . However, if the 1-D momentum theory formula for  $C_T$  is chosen (i.e.,  $C_T = 4a(1 - a)$ ), then the non-uniqueness problem still persists (see Fig. 3.2) although the range of application is increased to  $0 < a < 0.5$ . We get around this non-uniqueness problem by using the empirical formula for  $C_T$  by Buhl [65] which incorporates corrections for high disk (rotor) loading. The formula (Eq. 3.1, with  $F = 0.9$ ) provides a one-to-one mapping between  $a$  and  $C_T$  as can be seen in Fig. 3.2.



$$C_T(a) = \begin{cases} 4aF(1-a) & \text{if } 0 \leq a \leq 0.4 \\ \frac{8}{9} + \left(4F - \frac{40}{9}\right)a + \left(\frac{50}{9} - 4F\right)a^2 & \text{if } 0.4 < a \leq 1 \end{cases} \quad (3.1)$$

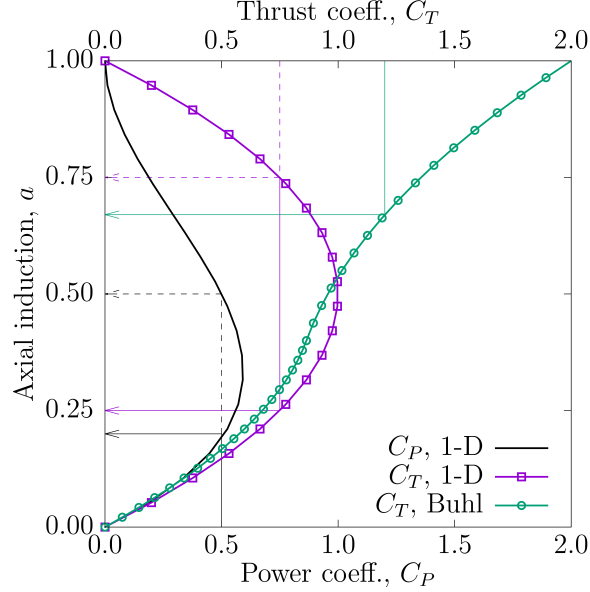


Figure 3.2: Functions to obtain axial induction factor,  $a$  from  $C_P$  and  $C_T$  given by 1-D momentum theory, and from  $C_T$  given by Eq. 3.1.

The second major change from Chattot's implementation [64] is in prescribing turbine wake structure. The wake behind a turbine expands and its convection velocity reduces from the rotor plane to the Trefftz plane. In previous works [61, 63, 64], the Trefftz plane was assumed to be located at the axial location where the wake completes three rotor revolutions, making it dependent on the tip speed ratio. The local axial induction,  $a_w(x)$  was assumed to vary linearly with downstream distance between the rotor plane and the Trefftz plane. We conducted a number of CFD runs varying rotor tip speed ratio (to vary rotor thrust) to understand the wake structure behind a wind turbine. The CFD methodology is described later in Section 3.3.1.1. Based on the CFD results we find that: (1) axial induction does not vary linearly with downstream distance, (2) it correlates well with thrust coefficient,  $C_T$  and (3) is independent of tip speed ratio when scaled appropriately. A reasonable collapse for a

wide range of data is obtained with the correlation -

$$\frac{a_w(x)}{a} = 1.85 - 0.85 \exp\left(-\frac{2}{3\sqrt{C_T}} \times \frac{x}{r_t}\right), \quad (3.2)$$

where  $r_t$  is the rotor tip radius and  $a_w(x)$  is the area-averaged axial induction in the rotor wake at a distance  $x$  from the rotor plane;  $a = a_w(0)$  is the induction at the rotor plane. Equation 3.2 and Fig. 3.3 suggest that the axial induction goes only up to  $1.85 \times a_w(0)$  at

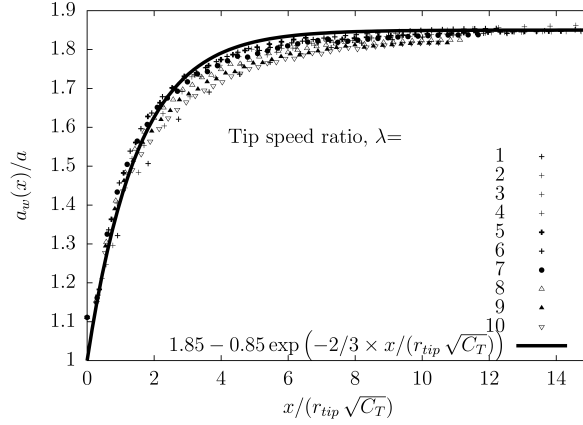


Figure 3.3: A correlation derived using wake data from a number of RANS CFD simulations.

the Trefftz plane. Note that the 1-D momentum theory requires the axial induction to reach  $2 \times a_w(0)$  at the Trefftz plane. This difference in CFD is likely due to diffusion of the wake with the freestream, which is physical. Numerical dissipation in CFD can also be the cause; the authors have performed a grid independence study [66] to rule out the grid resolution issue. We use Eq. 3.2 to prescribe the wake structure in our VLM implementation as opposed to the linear variation used in earlier works. Also, the wake expands radially as it convects downstream. The radial expansion is determined using mass conservation as  $r(x) = r(0) \times \sqrt{(1-a)/(1-a_w(x))}$ . The following section summarizes the prescribed-wake VLM algorithm for conventional, single-rotor turbines with the proposed changes.

### 3.2.1 Algorithm

Turbine information such as turbine rotor size, airfoil polars etc. are first read from user-specified input files. A value of  $C_T$  is assumed to compute the induction at the rotor plane,  $a$ .

Equation 3.2 then gives the distribution of axial induction  $a_w(x)$ , which along with the rotor tip speed ratio defines the initial wake helix structure. Induction coefficients for each point in the wake helix at each point on the blade are computed and stored. Since these coefficients only depend on the geometry, they stay constant as long as the wake helix shape remains the same.

An initial approximation of the blade bound circulation,  $\Gamma$  is computed using the Kutta-Jukowski theorem while assuming the local induction at the rotor plane to be  $a$  (computed earlier). Given the  $\Gamma$  distribution along the blade, the strengths of the trailing vortices at each radial location is determined by conserving circulation. Induction, and consequently the angle of attack at each radial location on the blade, are then calculated using the pre-computed induction coefficients. Airfoil polars then give the sectional lift and drag forces which are decomposed into the rotor-plane and out-of-rotor-plane components and integrated over the entire blade span to get the turbine thrust force and power coefficients. The Kutta-Jukowski theorem then gives a new approximation of sectional circulation,  $\Gamma_{new}$ . Iterations on  $\Gamma$  are performed with a fixed wake helix until it converges to within a specified tolerance. A new value of  $a$  is computed with the relation given in Eq. 3.1 using the last-computed value of  $C_T$ . The pitch of the wake helix is adjusted using Eq. 3.2 and the entire process is repeated until  $C_P$  converges.

### 3.2.2 Validation

Our implementation of the vortex lattice method, with the proposed modifications, is validated against experimental data and blade element momentum (BEM) theory predictions. The three-bladed, stall controlled, 95 kW Tellus T-1995 wind turbine is used for validation (measurement data from Ref. [6]). In the report [6], this turbine is referred to as Risø turbine. The turbine rotor diameter is 19 m. The turbine rotor blade chord and twist distributions are plotted in Fig. 3.4. Other details about the turbine, such as the airfoils used along the span, and the lift and drag polars are available in Ref. [6].

Figure 3.5 (a) compares turbine power variation with wind speed as predicted by the prescribed wake vortex lattice method solver against measured data as well as BEM theory pre-

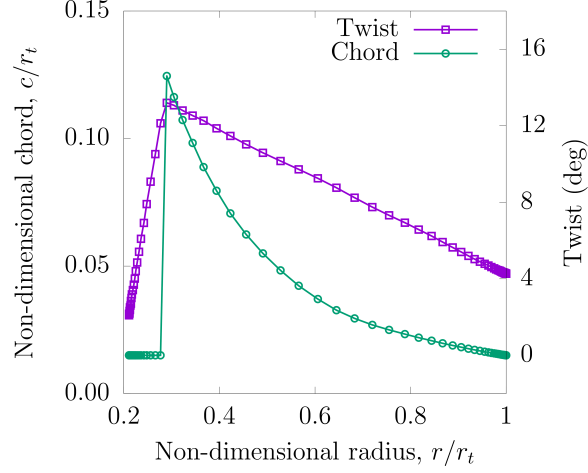


Figure 3.4: Non-dimensional chord and twist distributions for the model Tellus T-1995 (Risø) turbine used for validation [6].

dictions. The agreement with data by both prediction methods is good in the low-speed range, with the VLM showing a slightly better agreement. As the wind speed increases beyond about 12 m/s, the turbine starts to stall and 3D, spanwise flow becomes increasingly important. It is well known that such spanwise flow alleviates stall in 3D blades and allows them to operate at higher angles of attack than a corresponding 2-D airfoil. This 3D flow effect cannot be captured by strip-theory based methods such as the VLM and BEM. Therefore, the predictions fall short of the experimentally-measured turbine power in the region marked as “3-D stall effects” in the figure. Figure 3.5 (b) plots the same data as in Fig. 3.5 (a), but in the form of characteristic  $C_P - \lambda$  curves, where  $\lambda$  is the rotor tip speed ratio. The agreement with data is good outside the stall region.

Code-to-code comparisons (between vortex lattice method and BEM) of spanwise variations of sectional torque force coefficient,  $c_{\tau F}$  and sectional thrust force coefficient,  $c_T$  are presented at the tip speed ratio,  $\lambda = 6.0$  in Fig. 3.6. These coefficients are defined as

$$c_{\tau F} = c_l \sin(\phi) - c_d \cos(\phi), \text{ and}$$

$$c_T = c_l \cos(\phi) + c_d \sin(\phi),$$

where  $\phi$  is the angle that the local blade-relative velocity vector makes with the plane of rotation, and  $c_l$  and  $c_d$  are the blade section lift and drag coefficients. The agreement between

the two methods is very good. This verifies the solver capability for single rotor wind turbines. In the following section we present our approach to extend the vortex lattice method to DRWTs.

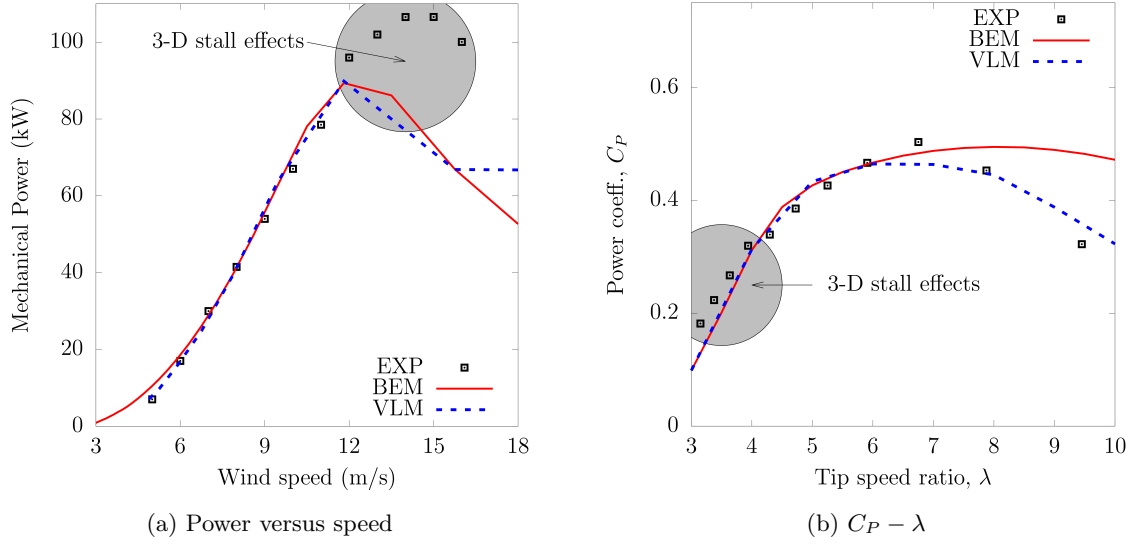


Figure 3.5: Comparisons with experimental data and BEM results for the Tellus T-1995 (Risø) turbine: (a) power variation with wind speed, and (b) the same information presented as characteristic ( $C_P - \lambda$ ) curves.

### 3.3 Extension to Dual-Rotor Wind Turbines

Several aspects need to be considered when evaluating the aerodynamic performance of dual-rotor wind turbines using a vortex lattice method:

1. Both rotors have trailing vortex sheets which have to be accounted for when calculating induction using the Biot-Savart law. Also, blade bound vorticity on the rotors mutually influence the induction on each other.
2. If the two rotors rotate independently, then the problem becomes inherently unsteady. Approximations need to be made to solve it as a steady problem.
3. If the two rotors are physically very close to each other then potential flow effects due to finite blade thickness also come into play.

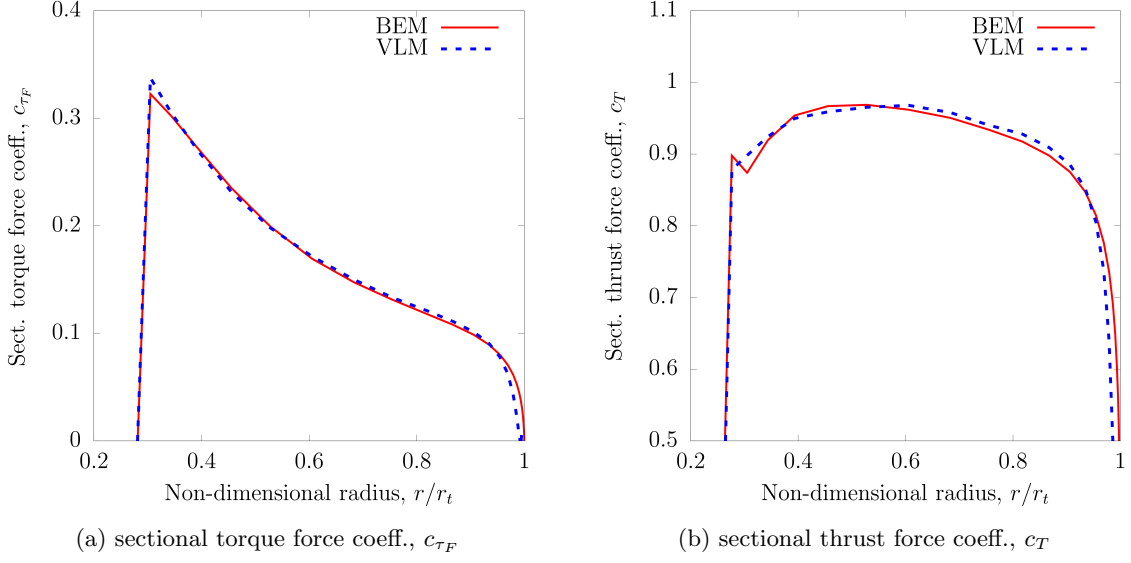


Figure 3.6: Comparisons of radial variation of force coefficients at  $\lambda = 6.0$  against BEM results for the Tellus T-1995 (Risø) turbine

To account for the mutual induction between the bound and trailing vortices of the two rotors of a DRWT, the associated vortex lattices need to be established. Figure 3.7 shows the vortex lattice structure of a DRWT. Two sets of helices are now present; one set each for the two rotors. The fact that the trailing vortices of both rotors are convected by the same flow speed is used to determine the pitches of the two helices. Equation 3.1 is used to determine the area-average induction at the rotor plane (a), and Eq. 3.2 to determine the variation of area-average induction with downstream distance ( $a_w(x)$ ). Rotor tip speed ratio and  $a_w(x)$  then determine the pitches of the wake helices. For DRWTs, an equivalent area-weighted  $C_{T,eq}$  is used in place of  $C_T$  in Eqs. 3.1 and 3.2, where

$$C_{T,eq} = C_{T,m} + \frac{A_s}{A_m} C_{T,s}, \quad (3.3)$$

and subscripts ‘ $m$ ’ and ‘ $s$ ’ refer to the main rotor and the secondary rotor respectively; ‘ $A$ ’ is area of rotor disk. Similarly, aerodynamic power coefficient of a DRWT is defined as  $C_{P,eq} = C_{P,m} + A_s/A_m C_{P,s}$ , which is the ratio of power extracted by the turbine to the power in the air stream flowing through the turbine rotors. Once the vorticity structure is set, the computation of induction coefficients using the Biot-Savart law is straightforward. It should be emphasized

again that the induction from blade bound vorticity of both the rotors has to be computed and added to the induction computed using the trailing vorticity. Another complexity can arise

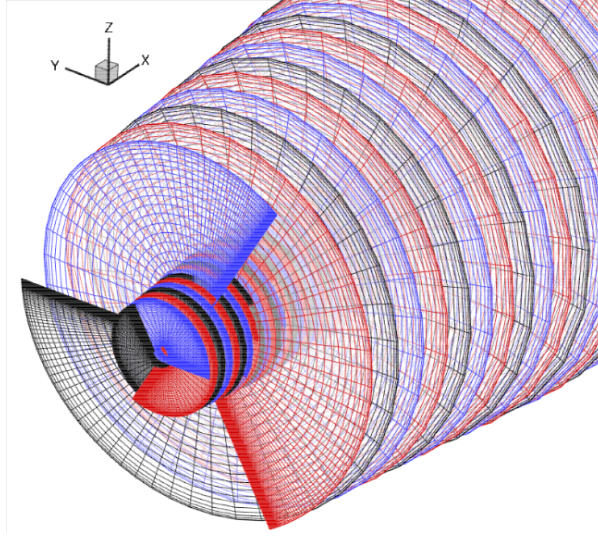


Figure 3.7: Trailing wake vorticity behind the two rotors of a dual-rotor wind turbine. Each rotor is three bladed. The three colors: red, blue, and black denote the trailing vorticity from each blade of the two rotors.

in computing induction. A singularity arises if any point on the trailing vortex structure of the upstream rotor coincides with a point on a blade of the downstream rotor where induction is computed. This singularity is averted by imposing a minimum threshold on the distance between two such points - avoiding division by zero when applying the Biot-Savart law.

If the two rotors rotate independently, the problem becomes unsteady even if uniform inflow is assumed. This is because of the relative rotation of the two rotors and the resulting temporal variation of blade aerodynamics. Unsteady computations, even with a vortex lattice method are expensive and not very suitable for preliminary design. We therefore use a pseudo-steady approximation, wherein we compute turbine performance for different relative clock (angular) positions of the two rotors. Averaging over such steady solutions gives the net performance of a DRWT. Figure 3.8 plots the variation in  $\%C_P$  of a DRWT for twelve relative rotor clock positions. The pattern repeats after  $120^\circ$  due to the periodicity in the problem; both rotors are three bladed. The maximum variation is observed to be less than 0.5%. For production runs, averaging is performed over five clock positions.

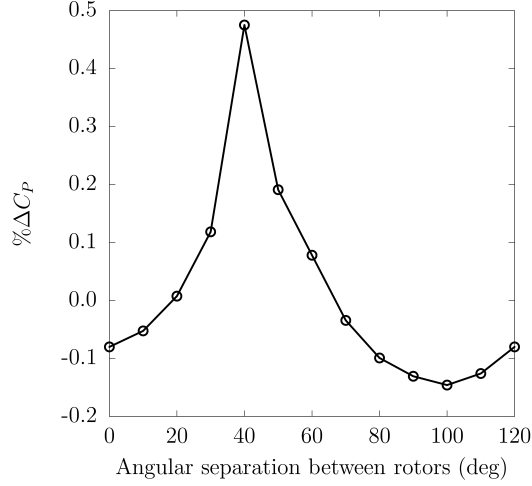


Figure 3.8: Predicted variation in %  $C_P$  of a DRWT with relative angular position between the primary and the secondary rotors.

Potential effects due to blade thickness decay exponentially away from the blade surfaces. To illustrate this, Fig. 3.9 presents potential flow results using a vortex panel code for the NACA 0030 airfoil. NACA 0030 is a 30% thick airfoil, which is representative of the thickness of airfoils used in the blade root region of utility scale wind turbines. The flow Mach number is 0.2 and the angle of attack is 0 degrees. The contour plot in Fig. 3.9 (a) shows rapid convergence to freestream pressure away from the airfoil. Percentage difference between local and freestream values of flow speed and pressure are plotted with distance away from the airfoil in the upstream direction in Fig. 3.9 (b). The differences between local and freestream flow speed and pressure are less than 1.5% and 0.08% respectively. In the present approach, we neglect potential interaction between the rotors due to blade thickness by assuming that the axial separation between the rotors is greater than the rotor blade chord. Rosenberg *et al.* [2] suggests that the optimum axial separation for enhanced isolated rotor aerodynamic performance is about  $0.2 \times$  the main rotor diameter, which is much greater than the maximum blade chord of the main rotor. Thus, the approximation to neglect potential effects due to blade thickness should be valid for such turbines.

The assumptions made in the proposed vortex lattice method for analysis of DRWTs are summarized below:



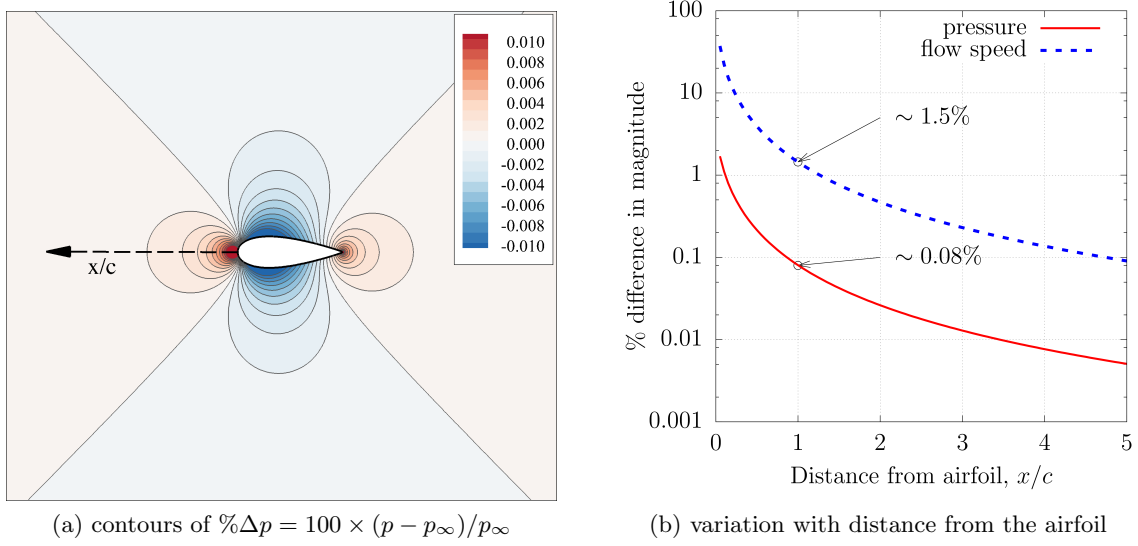


Figure 3.9: Panel code results for the NACA 0030 airfoil at freestream Mach number of 0.2 and zero angle of attack: (a) contours of percentage difference between local and freestream pressure, and (b) magnitude of difference between local and freestream pressure and flow speed along the dashed line in (a).

1. Potential interaction between the rotors due to blade thickness is neglected. This is justified for DRWTs where rotor-rotor separation is greater than blade chord.
2. Unsteadiness due to relative motion between the two rotors is not modeled. To get the net (time-averaged) effect, pseudo-steady, prescribed-wake VLM calculations are performed for multiple relative rotor clock positions and averaged. This assumption is verified in Section 3.3.1.3 by comparing VLM predictions against results from time-resolved CFD computations.

### 3.3.1 Verification with CFD

The proposed extended vortex lattice method to analyze dual-rotor wind turbines is verified against results obtained using two CFD methods: (1) the Reynolds Averaged Navier-Stokes + actuator disk (RANS/AD) method described in Selvaraj [1], and (2) the large eddy simulation + actuator line method (LES/ALM) method described in Ref. [18]. Subtle aspects of these two methods are summarized here for completeness.

### 3.3.1.1 RANS/AD Method

The RANS/AD method [2, 1] solves the incompressible RANS equations (Eq. 3.4) with the rotor blades modeled as body forces (actuator disk). The governing equations are

$$\begin{aligned} \frac{\partial \bar{u}_i}{\partial x_i} &= 0, \text{ and,} \\ \bar{u}_j \frac{\partial \bar{u}_i}{\partial x_j} &= -\frac{1}{\rho_0} \frac{\partial \bar{p}}{\partial x_i} + \nu \frac{\partial^2 \bar{u}_i}{\partial x_j^2} - \frac{\partial \overline{u'_i u'_j}}{\partial x_j} + \frac{f_i}{\rho_0}. \end{aligned} \quad (3.4)$$

In the above, the overbar denotes time averaging. The Reynolds stress tensor,  $\overline{u'_i u'_j}$  is modeled using the standard two equation,  $k - \epsilon$  turbulence model [67]. The term  $f_i$  represents the body force per unit volume and is computed using the user-prescribed airfoil polars, and the local flow velocity. The body force,  $f_i$  is spatially distributed - the distribution takes a Gaussian shape along the flow direction and uniform along the radial direction. Linear interpolation is used to compute  $f_i$  at the computational grid points. Axisymmetric flow assumption is made to reduce the problem to two dimensions.

This RANS/AD model is implemented in OpenFOAM and has been validated against experimental data as well as Blade Element Momentum (BEM) theory solutions for single-rotor turbines [2, 1, 68]. Recently, we have improved this methodology by incorporating Prandtl's tip loss correction following Mikkelsen [12]. The RANS/AD results presented in this paper use this improved model and are therefore slightly different from those in Refs. [1, 68].

The use of the RANS/AD CFD method to analyze DRWTs is described in Ref. [2]. Figure 3.10 shows an example computational grid and a CFD solution for flow over a DRWT. In this example the secondary rotor tip radius is 0.4 times that of the main rotor, and the main and secondary rotors are placed at  $x = +0.1$  and  $x = -0.1$  respectively. The physical coordinates are nondimensionalized by the rotor tip radius,  $r_t$ .

### 3.3.1.2 LES/ALM Method

The LES/ALM model implementation in the Simulator fOr Wind Farm Application (SOWFA) [18] software is used here. In this model, spatially filtered, incompressible forms of continuity and Navier-Stokes equations are solved using spatial and temporal discretization, and the actuator

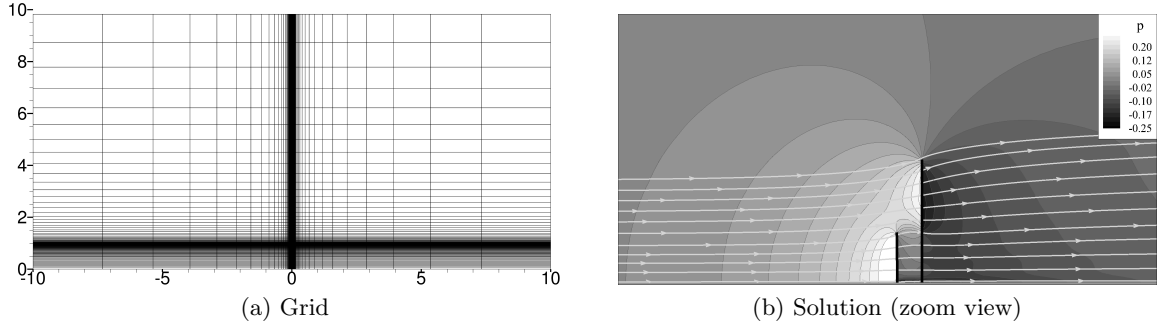


Figure 3.10: Computational grid and result of the RANS/AD method applied to a DRWT: (a) axisymmetric grid (every fifth point shown for clarity), and (b) pressure contours and streamlines (zoomed in near the DRWT).

line model (ALM) is used for rotor parameterization. Spatial filtering introduces unresolved, sub-grid scale (SGS) stresses, which have to be modeled. The width of the spatial filter is taken to be the grid-filter width given by  $\Delta = (\Delta_x \Delta_y \Delta_z)^{1/3}$ . Denoting spatially-filtered quantities by  $(\tilde{\cdot})$ , the governing fluid flow equations are

$$\begin{aligned}
 \frac{\partial \tilde{u}_i}{\partial x_i} &= 0, \\
 \frac{\partial \tilde{u}_i}{\partial t} + \tilde{u}_j \left( \frac{\partial \tilde{u}_i}{\partial x_j} - \frac{\partial \tilde{u}_j}{\partial x_i} \right) &= -\frac{\partial \tilde{p}^*}{\partial x_i} - \frac{\partial \tau_{ij}}{\partial x_j} + \nu \frac{\partial^2 \tilde{u}_i}{\partial x_j^2} - \underbrace{f_i / \rho_0}_{\text{blade force}} + \underbrace{\delta_{i3} g_0 (\tilde{\theta} - \langle \tilde{\theta} \rangle) / \theta_0}_{\text{buoyancy force}}, \\
 \frac{\partial \tilde{\theta}}{\partial t} + \tilde{u}_j \frac{\partial \tilde{\theta}}{\partial x_j} &= -\frac{\partial q_j}{\partial x_j} + \alpha \frac{\partial^2 \tilde{\theta}}{\partial x_j^2},
 \end{aligned} \tag{3.5}$$

where,  $\tilde{p}^* = \tilde{p} / \rho_0 + \tilde{u}_j \tilde{u}_j / 2$  is the modified kinematic pressure,  $\tau_{ij} = \widetilde{u_i u_j} - \tilde{u}_i \tilde{u}_j$ , is sub-grid scale (SGS) stress tensor, and  $q_j = \widetilde{u_j \theta} - \tilde{u}_j \tilde{\theta}$  is SGS heat flux.  $\theta$  is potential temperature,  $\alpha$  is thermal diffusivity of the fluid, and  $f_i$  is a momentum source term that models the force exerted by turbine rotor blades. The DRWT is modeled in SOWFA by simulating the two rotors of the DRWT as two separate single-rotor turbines placed in tandem without the towers. The use of SOWFA to model DRWTs is described in Ref. [49]. Figure 3.11 shows a sample results from a DRWT simulation using SOWFA.

### 3.3.1.3 Code-to-Code Comparisons

Two DRWT configurations are chosen for code-to-code comparisons between results from the proposed VLM and the two CFD methods. The radius of the secondary rotor is selected

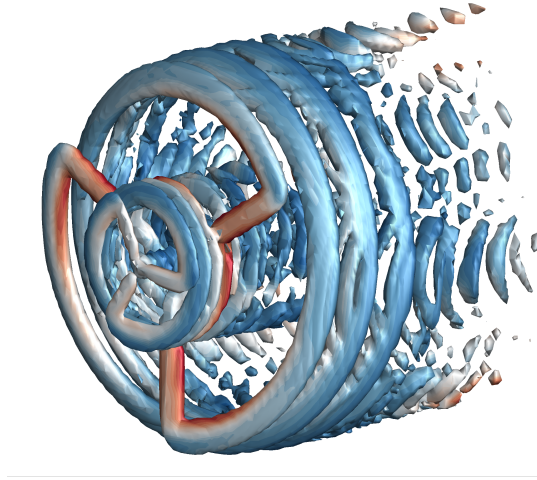


Figure 3.11: Iso-surfaces of Q-criterion ( $Q = 0.05$ ) computed using the LES/ALM method. The surfaces show the bound and trailing vortices and are colored with the r.m.s. of axial velocity.

to be 25% and 40% of the main rotor radius for the two designs, i.e.,  $r_{t,s}/r_{t,m} = 0.25$  and 0.4. However, both the DRWT configurations use the same *non-dimensional* rotors for the main rotor as well as the secondary rotor.

Figures 3.12 and 3.13 compare spanwise variations of local angle of attack and sectional torque force coefficients. The LES/ALM results are averaged over time and over the three blades of each rotor to generate the profiles; VLM results are phase averaged as described in Sec. 3.3. Good agreement between the results from the proposed VLM and the two CFD methods is observed for both the primary and the secondary rotors for the two DRWTs. The differences are largest at the radial location corresponding to the tip radius of the secondary rotor. This is expected for two reasons: (1) the turbulence in the CFD simulations (both RANS and LES) will diffuse the trailing vortex sheet of the secondary rotor while the VLM has no such mechanism, and (2) the RANS/AD model smears the effect of individual blades over the entire disk, whereas the VLM models each individual blade trailing vorticity independently. Even though VLM results are averaged over multiple relative clock positions of the two rotors in the proposed algorithm, it should be realized that this averaging is not the same as azimuthally averaging the trailing vortices, which is what happens in the RANS/AD method.

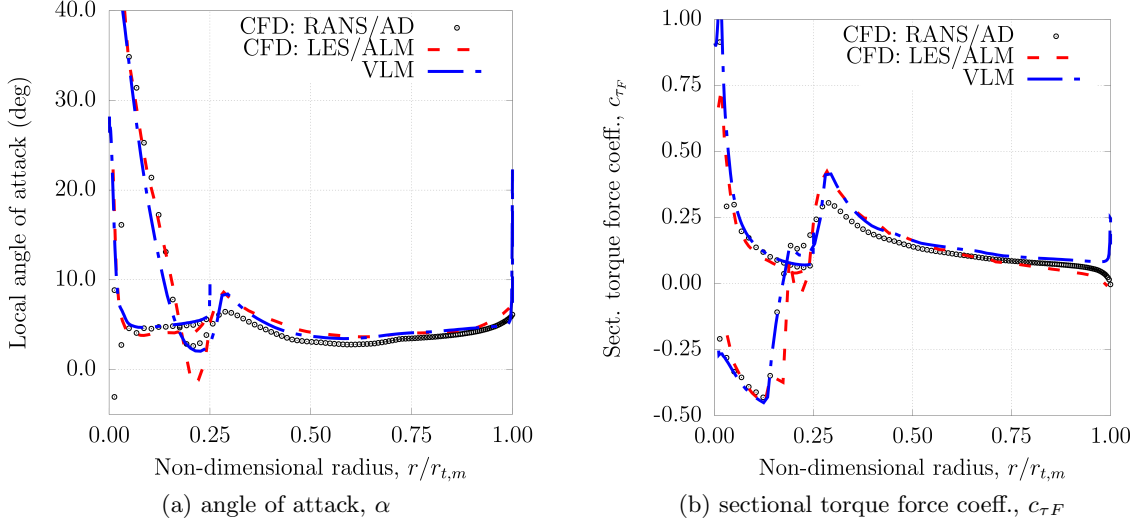


Figure 3.12: Comparisons between CFD and VLM of spanwise variations of angle of attack and torque force coefficient for the following parameters of the secondary rotor:  $r_{t,s}/r_{t,m} = 0.25$  and  $\lambda_s = 8.0$ .

### 3.4 Preliminary Design of a Dual-Rotor Wind Turbine

The proposed vortex lattice method is used to perform parametric sweeps for a DRWT design. One such study using the RANS/AD method was presented in Ref. [2] where the secondary rotor diameter, tip speed ratio, and rotor-rotor separation were varied. In this paper, we focus on varying only two parameters: rotor-rotor separation and secondary rotor tip speed ratio.

Figure 3.14 compares the results of parametric sweeps performed using the RANS/AD method and the vortex lattice method described in the previous sections. While the overall magnitudes are not predicted exactly, a good qualitative agreement is observed between the RANS/AD predictions and the VLM predictions of  $C_P$  enhancement with DRWTs. Both the methods suggest maximum gains for a DRWT design with  $r/r_t$  between 0.3 and 0.4 and secondary rotor tip speed ratio between 6 – 10. This verifies the ability of the proposed prescribed wake vortex lattice method to carry out preliminary design/analysis of dual-rotor wind turbines. The vortex lattice method is significantly inexpensive compared to the RANS/AD method; its computational cost is two orders of magnitude less than that of the RANS/AD

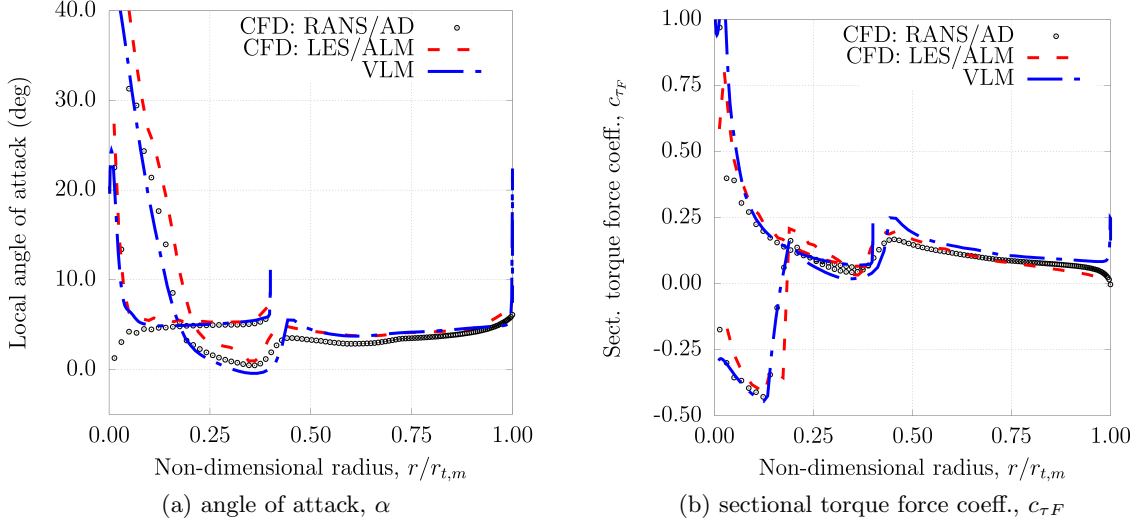


Figure 3.13: Comparisons between CFD and VLM of spanwise variations of angle of attack and torque force coefficient for the following parameters of the secondary rotor:  $r_{t,s}/r_{t,m} = 0.40$  and  $\lambda_s = 8.0$ .

method making it a good choice for preliminary design.

To estimate the aerodynamic performance improvement offered by the DRWT concept over a range of turbine operating conditions, a secondary rotor design with rotor-rotor separation of  $0.25 \times r_{t,m}$ ,  $r_{t,s}/r_{t,m} = 0.4$  and  $\lambda_s = 8$  is selected. A sweep of main rotor tip speed ratio is performed (while keeping  $\lambda_s$  fixed) with the proposed VLM and the results are compared against SRWT in Fig. 3.15. The DRWT offers enhanced energy capture for  $\lambda_m \leq 7.5$ . At higher  $\lambda_m$ , the secondary rotor gives a performance penalty. This performance penalty is due to non-optimal choice of  $\lambda_s$ , which can be avoided by identifying the right combinations of  $\lambda_m$  and  $\lambda_s$  to use during turbine operation. Similarly, the enhanced performance of the DRWT for  $\lambda_m \leq 7.5$  may further improve by varying  $\lambda_s$  with  $\lambda_m$ .

### 3.5 Conclusion

A prescribed wake vortex lattice method (VLM) to perform preliminary aerodynamic analysis of dual-rotor wind turbines is proposed. Modifications from previous works in the description of the trailing vortex helix are described. The method is validated against experimental data and blade element momentum (BEM) theory results for a conventional, single-rotor wind

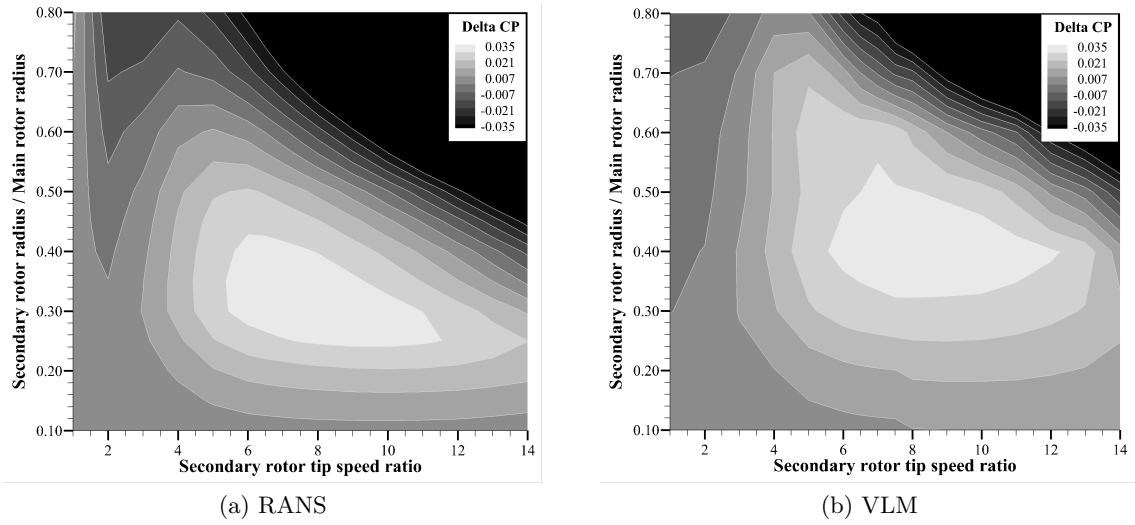


Figure 3.14: Parametric sweep results - contours of difference in aerodynamic power coefficient,  $\Delta C_P = C_{PDRWT} - C_{PSRWT}$  as predicted by (a) RANS and (b) VLM are shown. The parameters are tip radius and tip speed ratio of the secondary rotor.

turbine. The agreement between the measured and predicted power curves is good away from stall. The agreement between the VLM and BEM predictions for sectional torque and thrust force distributions is very good. The method is extended to analyze dual-rotor wind turbines by assuming pseudo-steady flow and averaging results over multiple relative rotor clock positions. The trailing wake structure of a DRWT is determined by recognizing that the trailing vortices of both rotors of a DRWT convect with the same flow velocity. Singularities in Biot-Savart's formula are avoided by enforcing a minimum threshold on spacing between vortex element center and the point where induction is calculated. Comparisons made with RANS/AD CFD simulations (where the turbine rotors are modeled as actuator disks) and with LES/ALM simulations (where the actuator line model is used to represent rotor blades) show good agreement in predicted spanwise profiles of torque force coefficient and angle of attack.

Parametric sweeps, varying the secondary rotor radius and tip speed ratio are carried out using the proposed VLM and compared with RANS/AD predictions. Both solvers provide similar design guidance (pointing to similar optimal configuration), proving that the proposed prescribed-wake vortex lattice method can be used as an alternative, inexpensive method to perform preliminary design of DRWTs. Two directions of future research will be explored:

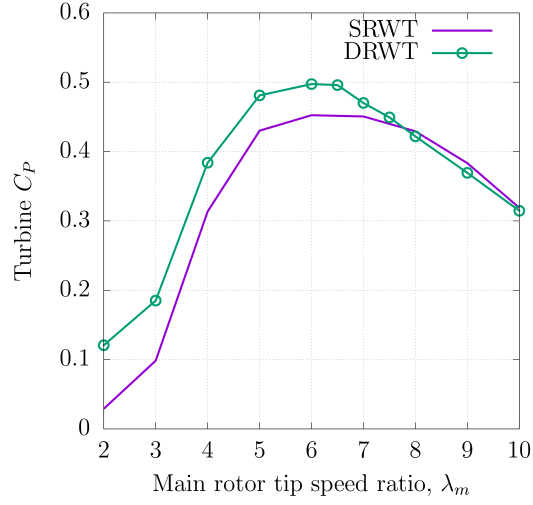


Figure 3.15: VLM predictions of aerodynamic power coefficients of a DRWT and the corresponding SRWT as a function of the man rotor tip speed ratio,  $\lambda_m$ .

- (1) develop an inverse design methodology for DRWTs using the VLM developed here, and
- (2) a full optimization study to explore DRWT designs that minimize wake loss in addition to enhancing isolated turbine performance.



## **CHAPTER 4. EXPLORING SURFACE FLOW CONVERGENCE INDUCED BY TIGHTLY-SPACED WIND TURBINES USING LARGE-EDDY SIMULATION**

**A version of this chapter was accepted as an extended abstract to the AIAA SciTech conference to take place in January 2017.**

### **Abstract**

Aerodynamic interaction between turbines in wind plants leads to surface flow convergence in addition to wake losses. This phenomenon has been observed in field tests with surface flux stations. A hypothesis is proposed to explain this surface flow convergence phenomenon - incomplete pressure recovery behind a turbine leading to successive pressure drops in tightly-spaced turbine arrays leads to drop in overall pressure deep inside a wind plant; this low-pressure acts as an attractor leading to flow convergence. Numerical investigations of the phenomenon of surface flow convergence are carried out that support this hypothesis. An actuator disk model to represent wind turbines in RANS and LES CFD solvers is used to simulate hypothetical wind plants. The flow convergence phenomenon reflects as a change in flow velocity direction and is more prominent near the ground than at turbine hub height. Numerical simulations of wind plant aerodynamics are conducted with various approximations to investigate and explain the flow convergence phenomenon.

## 4.1 Introduction

Aerodynamic interaction between turbines is known to cause significant losses in annual energy production in wind plants [32]. These losses arise in a turbine from ingestion of low-momentum fluid in wakes of upstream turbines. This mechanism of aerodynamic loss is therefore termed ‘wake loss’. Laboratory scale experiments [71, 72], field measurements [73], and numerical simulations [43, 18] have now significantly improved our understanding of how wake losses vary with wind plant layout, atmospheric stability, and turbine operation. A few novel wind turbine concepts [2, 49, 56], operation procedures [74], and turbine micro-siting designs [75] have also been proposed to mitigate wake losses in wind plants.

Another aerodynamic phenomenon - *surface flow convergence* - occurs in wind plants due to aerodynamic interaction between turbines. Recent experiments [7] in wind plants that use surface flux stations have reported surface flow angle deviations as large as 10 degrees due to wind turbines (see Figs. 4.1 and 4.2 ). With the current trend of building large wind plants with hundreds of turbines, such surface flow convergence can cause important microscale meteorological phenomena. Surface convergence leads to positive vertical velocity (to satisfy mass conservation), and such vertical motion can create preferential conditions for cloud formation and trigger local rainfall.

It is hypothesized that this convergence occurs due to a pressure gradient caused by compounding pressure drops as wind travels through the farm. Pressure drops sharply behind a wind turbine rotor and recovers slowly downstream. In wind farms, however, there might not be enough distance between rotors for pressure in the wake to fully recover before it experiences another pressure drop from a downstream turbine (see Fig 4.3). In large wind farms, the downwind side of the wind farm would experience an area of relatively low pressure, causing flow to converge.

This hypothesis has been tested computationally using Reynold’s Averaged Navier-Stokes (RANS) simulations [1, 4] with a large degree of success. This paper extends the investigation using Large-Eddy Simulation (LES) to determine the roles of inflow turbulence and atmospheric stability in surface flow convergence. A hypothetical wind farm is simulated using the actuator

disk model. Different atmospheric conditions are prescribed to see how they might effect the pressure gradient of the wind farm. These simulations are compared with experimental field data from Takle *et al.* [7] as well as RANS results from Selvaraj *et al.* [4].

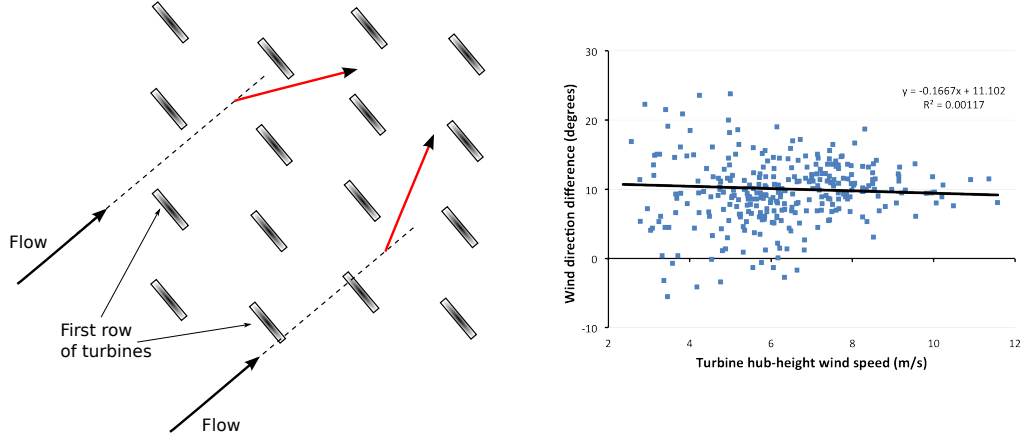


Figure 4.1: A schematic showing flow direction change.

Figure 4.2: Experimental data showing flow angle change in a neutrally stratified atmosphere. Courtesy Takle [7].

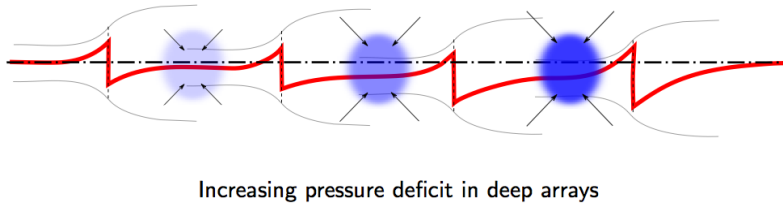


Figure 4.3: Subsequent pressure drops from multiple wind turbines.

## 4.2 Computational Model

Large Eddy Simulation (LES) has been used in recent years to simulate wind farm and wind turbine aerodynamics [15, 76]. The Simulator fOr Wind Farm Applications (SOWFA) is used to implement an actuator disk model into the LES equations[18, 3]. SOWFA is a utility built for use in the opensource CFD software, OpenFOAM. The incompressible form of the

governing LES equations are as follows, where  $(\sim)$  denotes the spatial filter:

$$\begin{aligned}
\frac{\partial \tilde{u}_i}{\partial x_i} &= 0, \\
\frac{\partial \tilde{u}_i}{\partial t} + \tilde{u}_j \left( \frac{\partial \tilde{u}_i}{\partial x_j} - \frac{\partial \tilde{u}_j}{\partial x_i} \right) &= -\frac{\partial \tilde{p}^*}{\partial x_i} - \frac{\partial \tau_{ij}}{\partial x_j} + \nu \frac{\partial^2 \tilde{u}_i}{\partial x_j^2} \\
&\quad - \underbrace{\frac{f_i}{\rho_0}}_{\text{turbine force}} + \underbrace{\frac{\delta_{i1} F_P}{\rho_0}}_{\text{driving pressure}} + \underbrace{\frac{\delta_{i3} g_0 (\tilde{\theta} - \langle \tilde{\theta} \rangle)}{\theta_0}}_{\text{buoyancy force}} + \underbrace{\frac{F_c \epsilon_{ij3} \tilde{u}_j}{\rho_0}}_{\text{coriolis force}}, \\
\frac{\partial \tilde{\theta}}{\partial t} + \tilde{u}_j \frac{\partial \tilde{\theta}}{\partial x_j} &= -\frac{\partial q_j}{\partial x_j} + \alpha \frac{\partial^2 \tilde{\theta}}{\partial x_j^2},
\end{aligned}$$

where,  $\tilde{p}^* = \tilde{p}/\rho_0 + \tilde{u}_i \tilde{u}_j / 2$  is the modified kinematic pressure,  $\tau_{ij} = \widetilde{u_i u_j} - \tilde{u}_i \tilde{u}_j$ , is sub-grid scale (SGS) stress tensor, and  $q_j = \widetilde{u_j \theta} - \tilde{u}_j \tilde{\theta}$  is SGS heat flux.  $f_i$  is a momentum source to model forces exerted by the actuator disk,  $\delta_{i1} F_P$  is pressure gradient to drive flow,  $\theta$  is potential temperature and  $\alpha$  is thermal diffusivity of the fluid. The deviatoric part of the SGS stress tensor,  $\tau_{ij}$  is typically modeled using an eddy-viscosity model,  $\tau_{ij} - 1/3 \delta_{ij} \tau_{kk} = -2\nu_{sgs} \widetilde{S}_{ij}$  and the SGS heat flux with an eddy-diffusivity model  $q_j = \widetilde{u_j \theta} - \tilde{u}_j \tilde{\theta} = -(\nu_{sgs}/Pr_{sgs}) \partial \tilde{\theta} / \partial x_j$ , where,  $\widetilde{S}_{ij} = 1/2 (\partial \tilde{u}_i / \partial x_j + \partial \tilde{u}_j / \partial x_i)$  is the resolved strain-rate tensor and  $Pr_{sgs}$  is the SGS Prandtl number. The mixing-length model by Smagorinsky [45],  $\nu_{sgs} = (C_S \Delta)^2 |\tilde{S}|$  is used to model  $\nu_{sgs}$ .

The actuator disk model is used as a cheaper alternative to resolving the wind turbine blade geometry. The force term in the momentum equation,  $f_i$ , is used to model the forces that the turbine blades exert on the flow and is determined using blade element theory and user-prescribed 2-D airfoil polars. Using the local inflow velocity and angle of attack, airfoil polars are used to determine the sectional lift ( $dL$ ) and drag ( $dD$ ) (see Fig. 4.4). These forces can be decomposed into in-plane ( $d\tau_F$ ) and out-of-plane ( $dT$ ) forces. Once the forces are determined at a given radius, they are distributed uniformly in the circumferential direction and as a Gaussian distribution along the axial direction, such that the integrated forces match the computed  $d\tau_F$  and  $dT$ .

#### 4.2.1 Validation of Actuator Disk Model

The implementation of the actuator disk model within LES is validated against the Tellus T-1995 experimental (Risø) wind turbine [6]. It is a three bladed, stall regulated 95 kW turbine

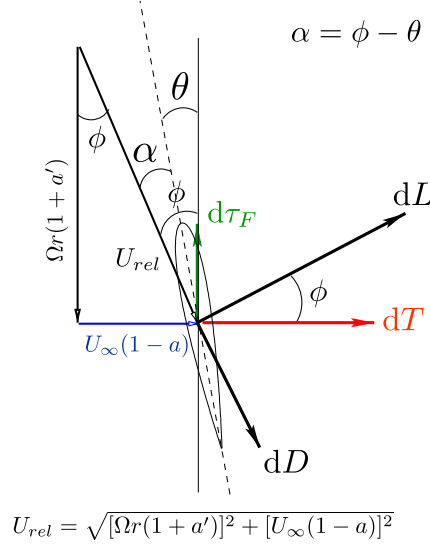


Figure 4.4: Flow vectors and aerodynamic forces on a rotor blade section.

with a rotor diameter of 19 meters. The chord and twist distributions are plotted in Fig. 4.5.

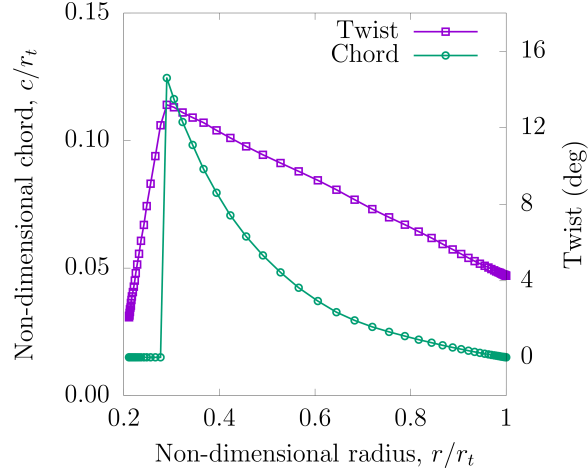


Figure 4.5: Non-dimensional chord and twist distributions for the model Tellus T-1995 (Risø) turbine used for validation [6].

Figure 4.6 plots power coefficient LES+AD results compared with experimental results. A reasonable match is found for the turbine operating near the design point ( $\lambda \approx 7$ ). Code-to-code comparisons are used to determine how well the AD model captures radial force profiles. Figures 4.7 and 4.8 plot the thrust and torque force coefficient as a function of radial location. Results from the actuator disk model are compared with results from an actuator line model

(ALM) [77] implemented in an LES computation as well as results from a vortex lattice method (VLM) [55] and blade element momentum theory [9].

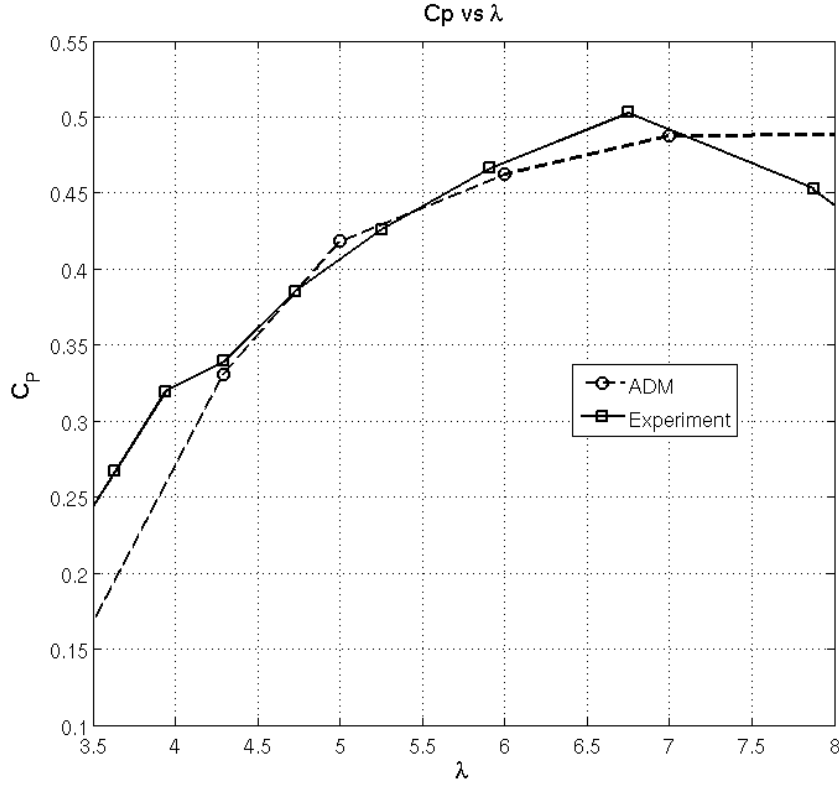


Figure 4.6:  $C_P$ - $\lambda$  curve for Risø turbine.

### 4.3 Wind Farm Simulations

Two hypothetical wind farms are evaluated. The layouts of the wind farms are described below and the results are presented in the following section.

#### 4.3.1 Finite Wind Farm in Uniform Flow

A simplified simulation is carried out to test the hypothesis that a pressure gradient forms over large wind farms due to compounding pressure drops. The wind farm consists of 41 NREL 5MW reference turbines [48] running at a tip-speed ratio of  $\lambda = 10$ . This tip-speed ratio is chosen to achieve a high thrust coefficient ( $C_T$ ); as per the hypothesis, high turbine thrust

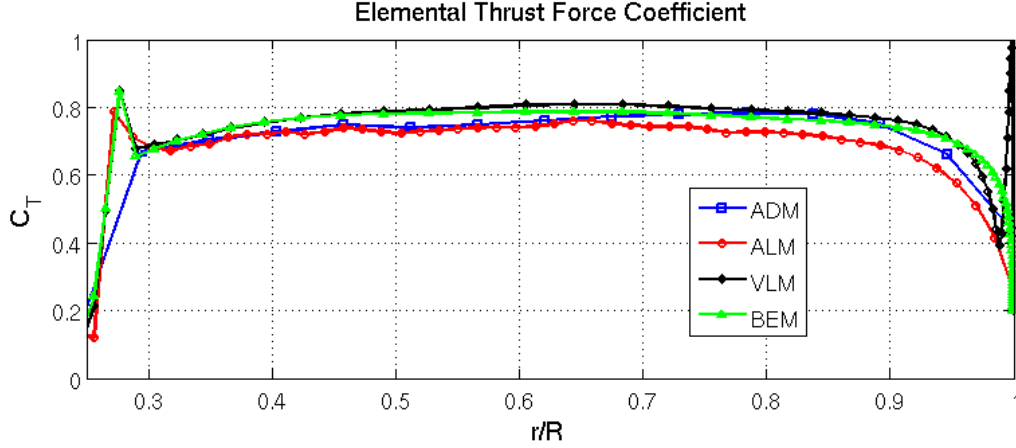


Figure 4.7: Radial thrust force coefficient for Risø turbine at  $\lambda = 7$ .

should result in large flow convergence. Turbines are spaced within the rows and columns at a distance of 5 rotor diameters apart in both the North-South and East-West directions. Rows and columns are staggered and spaced at 2.5 rotor diameters apart. The layout is shown in Fig. 4.9. The domain is a square with sides 70 rotor diameters in length. The authors acknowledge that this spacing is too tight and not realistic; the purpose here is solely to test the hypothesis behind flow convergence and hence hypothetical conditions are selected that would result in maximum flow convergence. The turbines operate in the center of the domain in the vertical direction with a distance of 4 rotor diameters above and below hub height. Slip boundary conditions are used for the upper and lower boundaries while zero gradient is prescribed for the North and East boundaries. Uniform inflow at a  $45^\circ$  is prescribed at the South and West boundaries.

#### 4.3.2 Semi-infinite Wind Farm

The wind farm domain used in the LES simulations is shown in Fig. 4.10. It includes 10 Risø wind turbines spaced 5 rotor diameters ( $D = 17$  m) apart at a yaw angle of  $45^\circ$  with respect to the inlet. Periodic boundary conditions are used to simulate an infinite wind farm in the North-South direction. The flow at hub height is at  $45^\circ$ . The flow is uniform and does not include any thermal stratifications effects. The width of the domain in the North-South

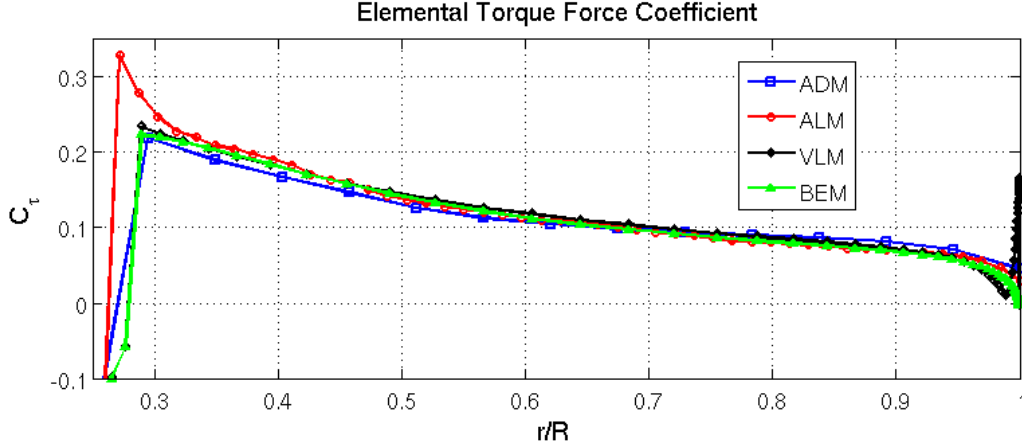


Figure 4.8: Radial torque force coefficient for Risø turbine at  $\lambda = 7$ .

direction is 5 rotor diameters.

## 4.4 Results

### 4.4.1 Finite Wind Farm

Pressure contours at hub height from the finite wind farm clearly show a decrease in pressure over the array resulting in the expected pressure gradient (Fig. 4.11a). This pressure gradient is seemingly responsible for the deflection in the mean wind speed as shown in Fig. 4.11b.

### 4.4.2 Semi-infinite Wind Farm

The LES results show reasonable qualitative agreement with experimental data as well as RANS simulations. Figure 4.12 shows the mean wind direction at different points in the domain for a uniform boundary layer. No turbulence was included in this run. The freestream has a wind direction of  $45^\circ$  at 8 m/s. As the wind travels through the array, the wind direction turns clockwise. By the last turbine, the mean wind direction had changed by roughly  $6^\circ$  at hub height. Figure 4.14 shows a continual decrease in gauge pressure as the wind flows through the array. This supports the hypothesis that a compounding pressure drop is responsible for the flow angle changes observed in field experiments.



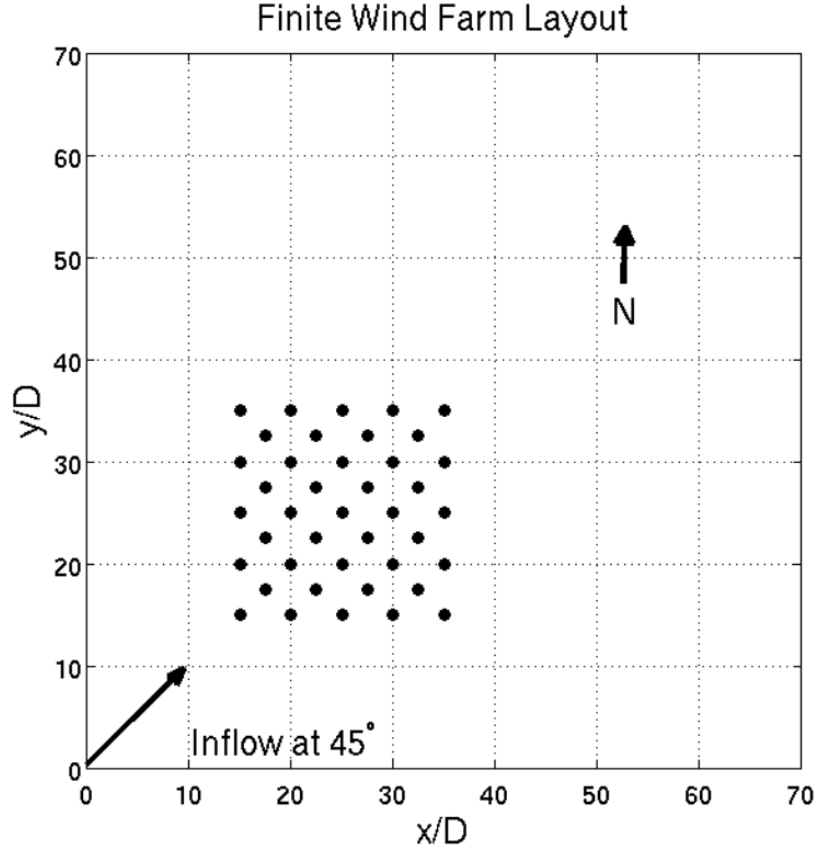


Figure 4.9: Finite wind farm domain.

## 4.5 Conclusion

Results from uniform flow simulations support the hypothesis that compounding pressure drops are responsible for the flow angle changes observed in Takle *et al.* [7]. Future work should include more realistic atmospheric conditions. These simulations will give insight into how inflow turbulence and atmospheric stability might influence the phenomenon of flow convergence. It is expected that the more stable a boundary layer is, the larger the observed flow angle changes will be due to longer wake recovery periods.

Furthermore, the future work will investigate how the pressure and wind direction are affected near the surface. It is expected that the flow angle change will increase at lower altitudes. The pressure gradient will have more influence because the dynamic pressure is lower near the ground where wind speeds are lower.

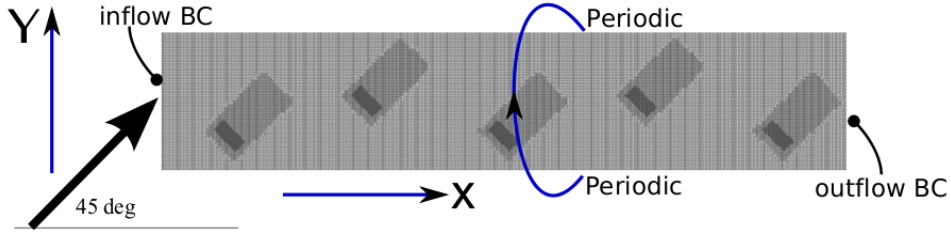
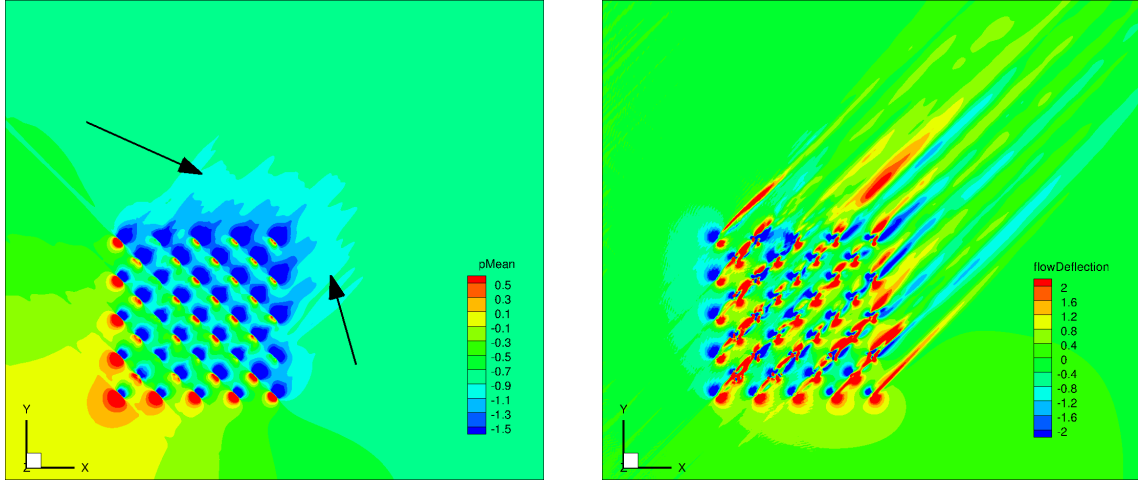


Figure 4.10: Periodic wind farm domain.



(a) Mean pressure contours at hub height from finite wind farm LES simulation. The arrows indicate the direction of the pressure gradient that is responsible for the flow deflection.

(b) Flow deflection (clockwise positive) contours at hub height from finite wind farm LES simulation

Figure 4.11: Mean flow contours from a tightly spaced wind farm simulated using LES+ADM.

## 4.6 Acknowledgements

The first author is supported under the U.S. National Science Foundation Grant No. 1069283 which supports the activities of the Integrative Graduate Education and Research Traineeship (IGERT) in Wind Energy Science, Engineering and Policy (WESEP) at Iowa State University. Computational resources are provided by NSF XSEDE (Grant #TG-CTS130004). The authors would like to thank Prof. Eugene Takle and Dr. Daniel Rajewski for providing experimental data on flow convergence and for several technical discussions on modeling efforts.

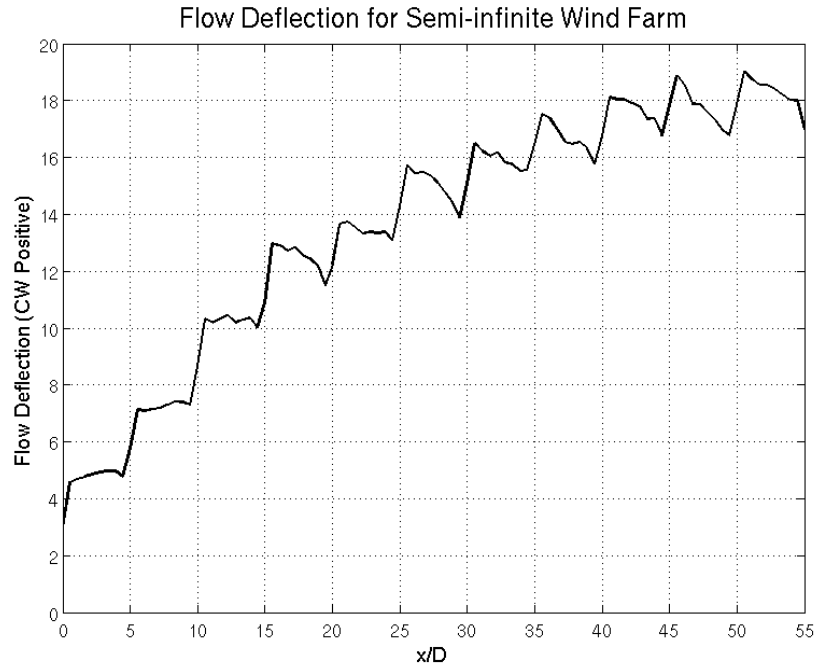


Figure 4.12: Flow angle change from uniform LES simulation of semi-infinite wind farm.

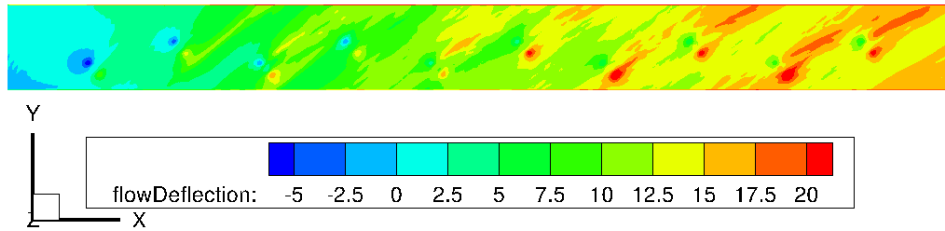


Figure 4.13: Contour of mean flow deflection from uniform LES simulation of semi-infinite wind farm.

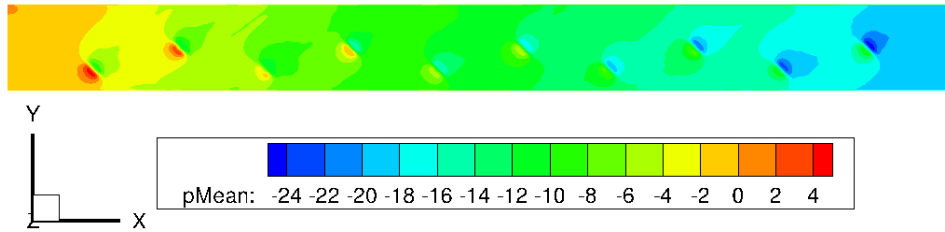


Figure 4.14: Contour of mean pressure from uniform LES simulation of semi-infinite wind farm.

## CHAPTER 5. CONCLUSION

This thesis provides the motivational framework as well as methods for the analysis and design of DRWTs. The motivation, as described in Chapter 1, is to increase power extraction from wind turbines and wind farms by mitigating losses. These losses are described in section 1.5. The two forms of loss that are specifically targeted are root loss due to poor root section aerodynamics and wake loss due to turbines operating in the wake of other turbines.

Chapter 2 introduces the dual rotor wind turbine. The secondary rotor is smaller, axially aligned with the main rotor, and designed with high lift-to-drag ratio airfoils. A DRWT is designed using the NREL 5 MW turbine as the main rotor and the secondary rotor made out of the DU96 airfoil. Parametric sweeps using RANS simulations show that secondary rotor turbine size should be 25% of the main rotor and it should be axially separated from the main rotor by a distance of 0.2 times the main rotor radius. A net benefit of 7% in  $C_P$  is predicted by RANS calculations for the optimized DRWT design. Large eddy simulations for the optimized DRWT operating in uniform flow show a net increase in power generation of about 4.6%. Wake comparisons confirm efficient extraction of energy in the root region by the DRWT. However, increase in vertical entrainment of energy, which would reduce turbine wake losses, is not clearly observed in the simulations.

Chapter 3 extends the commonly used vortex lattice method for use in analysis of multi-rotor wind turbines. Modifications from previous works in the description of the trailing vortex helix are described. The method is validated against experimental data and blade element momentum (BEM) theory results for a conventional, single-rotor wind turbine. The agreement between the measured and predicted power curves is good away from stall. The agreement between the VLM and BEM predictions for sectional torque and thrust force distributions is very good. The method is extended to analyze dual-rotor wind turbines by assuming pseudo-

steady flow and averaging results over multiple relative rotor clock positions. The trailing wake structure of a DRWT is determined by recognizing that the trailing vortices of both rotors of a DRWT convect with the same flow velocity. Singularities in Biot-Savart’s formula are avoided by enforcing a minimum threshold on spacing between vortex element center and the point where induction is calculated. Comparisons made with RANS/AD CFD simulations (where the turbine rotors are modeled as actuator disks) and with LES/ALM simulations (where the actuator line model is used to represent rotor blades) show good agreement in predicted spanwise profiles of torque force coefficient and angle of attack.

Parametric sweeps, varying the secondary rotor radius and tip speed ratio are carried out using the proposed VLM and compared with RANS/AD predictions. Both solvers provide similar design guidance (pointing to similar optimal configuration), proving that the proposed prescribed-wake vortex lattice method can be used as an alternative, inexpensive method to perform preliminary design of DRWTs. Two directions of future research will be explored: (1) develop an inverse design methodology for DRWTs using the VLM developed here, and (2) a full optimization study to explore DRWT designs that minimize wake loss in addition to enhancing isolated turbine performance.

Finally, Chapter 4 explores the phenomenon of surface flow convergence through LES and an actuator disk model. Results from simulations suggest that pressure gradients over large portions of wind farms might be responsible for a change in flow direction seen in field data. This flow deflection might result in flow convergence that could have microclimatological consequences. Further investigation is required to determine how atmospheric stability and wind farm operation might affect this phenomenon. Future LES simulations should include fully turbulent boundary layers with different thermal stratifications.

Comprehensive investigation is still required to determine if a DRWT is feasible at the utility scale. Methods and designs developed in this thesis are useful only for aerodynamic entitlement purposes. This work has shown that adding a second rotor increases aerodynamic power extraction. However, further work is required to determine if the DRWT configuration is cost effective. To be feasible, the increased revenue due to increased power extraction must be greater than the increased cost associated with the addition of a second rotor.

## APPENDIX A. COORDINATE SYSTEMS

Three coordinate systems are used: (1) attached to the ground in which the CFD simulations are performed, which is specified by the unit vectors  $(\hat{e}_{\tilde{x}}, \hat{e}_{\tilde{y}}, \hat{e}_z)$ ;  $\hat{e}_{\tilde{x}}$  points East,  $\hat{e}_{\tilde{y}}$  points North, and  $\hat{e}_z$  points up and away from the ground (Earth), (2) the coordinate system aligned with the freestream flow direction given by the unit vectors  $(\hat{e}_x, \hat{e}_y, \hat{e}_z)$ , where  $\hat{e}_x$  makes an angle  $\phi$  with  $\hat{e}_{\tilde{x}}$ , and (3) a cylindrical coordinate system given by  $(\hat{e}_r, \hat{e}_\theta, \hat{e}_z)$  is used to compute turbulent momentum and energy flux into a cylindrical region behind the turbine rotor. These coordinates and their inter-relationships are shown in Fig. A.1.

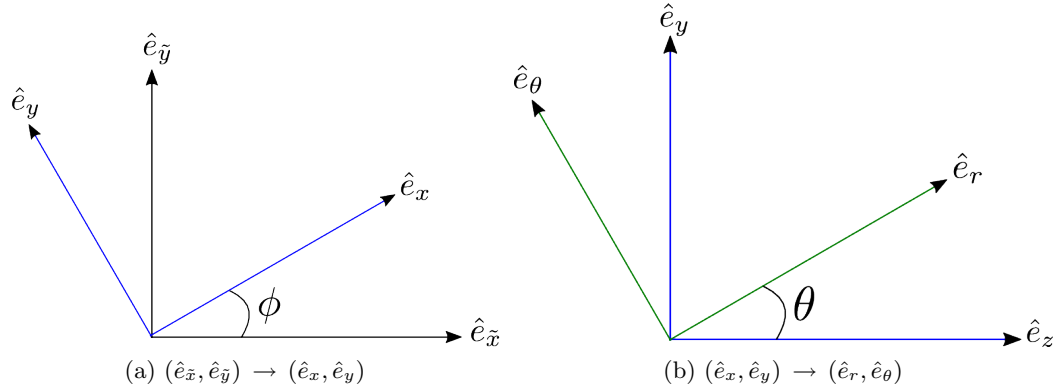


Figure A.1: The three coordinate systems used and their interrelationships. The CFD simulations are performed in  $(\hat{e}_{\tilde{x}}, \hat{e}_{\tilde{y}}, \hat{e}_z)$ ; meanflow is along the  $\hat{e}_x$  direction.

## APPENDIX B. STREAMWISE TURBULENT MOMENTUM AND ENERGY FLUX

Streamwise turbulent momentum flux through the circular cylinder in Fig. 2.13 is determined by integrating the Reynolds stress term  $\overline{u'_r u'_x}$  over the cylinder surface.  $\overline{u'_r u'_x}$  is related to the Reynolds stress defined in the  $(\hat{e}_{\tilde{x}}, \hat{e}_{\tilde{y}}, \hat{e}_z)$  coordinate system as follows:

$$\begin{aligned}\overline{u'_r u'_x} &= \overline{(u'_z \cos \theta + u'_y \sin \theta) \times (u'_{\tilde{x}} \cos \phi + u'_{\tilde{y}} \sin \phi)} \\ &= \left( \overline{u'_{\tilde{x}} u'_z} \cos \phi + \overline{u'_{\tilde{y}} u'_z} \sin \phi \right) \cos \theta + \left( \overline{u'_{\tilde{x}} u'_y} \cos \phi + \overline{u'_{\tilde{y}} u'_y} \sin \phi \right) \sin \theta,\end{aligned}\quad (\text{B.1})$$

where,

$$\begin{aligned}\overline{u'_{\tilde{x}} u'_y} &= \overline{u'_{\tilde{x}} u'_{\tilde{y}}} \cos \phi - \overline{u'^2_{\tilde{x}}} \sin \phi, \text{ and} \\ \overline{u'_{\tilde{y}} u'_y} &= \overline{u'^2_{\tilde{y}}} \cos \phi - \overline{u'_{\tilde{x}} u'_{\tilde{y}}} \sin \phi.\end{aligned}$$

Using these in Eq. B.1 gives

$$\begin{aligned}\overline{u'_r u'_x} &= \left( \overline{u'_{\tilde{x}} u'_z} \cos \phi + \overline{u'_{\tilde{y}} u'_z} \sin \phi \right) \cos \theta \\ &\quad + \left( \overline{u'_{\tilde{x}} u'_{\tilde{y}}} \cos^2 \phi - \overline{u'_{\tilde{x}} u'_{\tilde{y}}} \sin^2 \phi + \overline{u'^2_{\tilde{y}}} \frac{\sin(2\phi)}{2} - \overline{u'^2_{\tilde{x}}} \frac{\sin(2\phi)}{2} \right) \sin \theta, \\ \text{or, } \overline{u'_r u'_x} &= \left( \overline{u'_{\tilde{x}} u'_z} \cos \phi + \overline{u'_{\tilde{y}} u'_z} \sin \phi \right) \cos \theta \\ &\quad + \left( \overline{u'_{\tilde{x}} u'_{\tilde{y}}} \cos(2\phi) + (\overline{u'^2_{\tilde{y}}} - \overline{u'^2_{\tilde{x}}}) \frac{\sin(2\phi)}{2} \right) \sin \theta.\end{aligned}\quad (\text{B.2})$$

The turbulent energy flux is obtained by integrating the following over the surface.

$$\overline{u_x} \times \overline{u'_r u'_x} = \overline{u'_{\tilde{x}} \cos \phi + u'_{\tilde{y}} \sin \phi} \times \overline{u'_r u'_x} \quad (\text{B.3})$$

## BIBLIOGRAPHY

- [1] Suganthi Selvaraj. Numerical investigation of wind turbine and wind farm aerodynamics. 2014.
- [2] A Rosenberg, S Selvaraj, and A Sharma. A novel dual-rotor turbine for increased wind energy capture. In *Journal of Physics: Conference Series*, volume 524, page 012078. IOP Publishing, 2014.
- [3] Matthew J Churchfield, Sang Lee, Patrick J Moriarty, Luis A Martinez, Stefano Leonardi, Ganesh Vijayakumar, and James G Brasseur. A large-eddy simulation of wind-plant aerodynamics. *AIAA paper*, (2012-0537), 2012.
- [4] S. Selvaraj, A. Chaves, E. Takle, and A. Sharma. Numerical prediction of surface flow convergence phenomenon in windfarms. In *Proceedings of the Conference on Wind Energy Science and Technology*, METU, Ankara, Turkey, 2013. RUZGEM, Middle Eastern Technical University.
- [5] B.G. Newman. Multiple actuator-disc theory for wind turbines. *Journal of Wind Engineering and Industrial Aerodynamics*, 24:215–225, 1986.
- [6] JG Schepers, AJ Brand, A Bruining, JMR Graham, MM Hand, DG Infield, HA Madsen, RJH Paynter, and DA Simms. Final report of IEA Annex XIV: Field rotor aerodynamics. 1997.
- [7] E. S. Takle, D. A. Rajewski, J. K. Lundquist, W. A. Gallus, and A Sharma. Measurements in support of wind farm simulations and power forecasts: The crop/wind-energy experiments (cwex). *Journal of Physics: Conference Series*, 524, 2014.



- [8] Seungmin Lee, Hogeon Kim, and Soogab Lee. Analysis of aerodynamic characteristics on a counter-rotating wind turbine. *Current Applied Physics*, 10(2):S339–S342, 2010.
- [9] Albert Betz. Schraubenpropeller mit geringstem energieverlust. mit einem zusatz von l. prandtl. *Nachrichten von der Gesellschaft der Wissenschaften zu Göttingen, Mathematisch-Physikalische Klasse*, 1919:193–217, 1919.
- [10] LJ Vermeer, Jens Nørkær Sørensen, and A Crespo. Wind turbine wake aerodynamics. *Progress in aerospace sciences*, 39(6):467–510, 2003.
- [11] B Sanderse, SP Pijl, and B Koren. Review of computational fluid dynamics for wind turbine wake aerodynamics. *Wind Energy*, 14(7):799–819, 2011.
- [12] Robert Mikkelsen. *Actuator disc methods applied to wind turbines*. PhD thesis, Technical University of Denmark, 2003.
- [13] A Jimenez, A Crespo, E Migoya, and J Garcia. Advances in large-eddy simulation of a wind turbine wake. In *Journal of Physics: Conference Series*, volume 75, page 012041. IOP Publishing, 2007.
- [14] A Jimenez, A Crespo, E Migoya, and J Garcia. Large-eddy simulation of spectral coherence in a wind turbine wake. *Environmental Research Letters*, 3(1):015004, 2008.
- [15] Fernando Porté-Agel, Yu-Ting Wu, Hao Lu, and Robert J Conzemius. Large-eddy simulation of atmospheric boundary layer flow through wind turbines and wind farms. *Journal of Wind Engineering and Industrial Aerodynamics*, 99(4):154–168, 2011.
- [16] Niels Troldborg, Gunner C Larsen, Helge A Madsen, Kurt S Hansen, Jens N Sørensen, and Robert Mikkelsen. Numerical simulations of wake interaction between two wind turbines at various inflow conditions. *Wind Energy*, 14(7):859–876, 2011.
- [17] Yu-Ting Wu and Fernando Porté-Agel. Simulation of turbulent flow inside and above wind farms: Model validation and layout effects. *Boundary-layer meteorology*, 146(2):181–205, 2013.

- [18] Matthew J Churchfield, Sang Lee, John Michalakes, and Patrick J Moriarty. A numerical study of the effects of atmospheric and wake turbulence on wind turbine dynamics. *Journal of turbulence*, (13), 2012.
- [19] Ganesh Vijayakumar, Adam W Lively, Balaji Jayaraman, Brent C Craven, and James G Brasseur. Blade boundary layer response to atmospheric boundary layer turbulence on a nrel 5mw wind turbine blade with hybrid urans-les. 2014.
- [20] Adam W Lively, Ganesh Vijayakumar, Brent Craven, Balaji Jayaraman, Tarak N Nandi, Eric G Paterson, and James G Brasseur. Towards a blade-resolved hybrid urans-les of the nrel 5-mw wind turbine rotor within large eddy simulation of the atmospheric boundary layer. 2014.
- [21] Wei Yuan, Ahmet Ozbay, Wei Tian, and Hui Hu. An experimental investigation on the effects of turbine rotation directions on the wake interference of wind turbines. 2013.
- [22] Hui Hu, Ahmet Ozbay, Wei Tian, and Zifeng Yang. An experimental study on the effects of wake interference on the performances of wind turbines over complex terrains. In *ASME 2012 Fluids Engineering Division Summer Meeting collocated with the ASME 2012 Heat Transfer Summer Conference and the ASME 2012 10th International Conference on Nanochannels, Microchannels, and Minichannels*, pages 1197–1203. American Society of Mechanical Engineers, 2012.
- [23] Leonardo P Chamorro and Fernando Porté-Agel. Turbulent flow inside and above a wind farm: a wind-tunnel study. *Energies*, 4(11):1916–1936, 2011.
- [24] Leonardo P Chamorro and Fernando Porté-Agel. Effects of thermal stability and incoming boundary-layer flow characteristics on wind-turbine wakes: a wind-tunnel study. *Boundary-layer meteorology*, 136(3):515–533, 2010.
- [25] Giacomo Valerio Iungo, Yu-Ting Wu, and Fernando Porté-Agel. Field measurements of wind turbine wakes with lidars. *Journal of Atmospheric and Oceanic Technology*, 30(2):274–287, 2013.

- [26] ES Takle, JH Prueger, DA Rajewski, JK Lundquist, M Aitken, ME Rhodes, AJ Deppe, FE Goodman, KC Carter, L Mattison, et al. Wind and flux measurements in a windfarm co-located with agricultural production. In *AGU Fall Meeting Abstracts*, volume 1, page 05, 2010.
- [27] Rebecca Jane Barthelmie, Sten Tronæs Frandsen, MN Nielsen, SC Pryor, P-E Rethore, and HE Jørgensen. Modelling and measurements of power losses and turbulence intensity in wind turbine wakes at middelgrunden offshore wind farm. *Wind Energy*, 10(6):517–528, 2007.
- [28] Kurt S Hansen, Rebecca J Barthelmie, Leo E Jensen, and Anders Sommer. The impact of turbulence intensity and atmospheric stability on power deficits due to wind turbine wakes at horns rev wind farm. *Wind Energy*, 15(1):183–196, 2012.
- [29] Rebecca Jane Barthelmie and LE Jensen. Evaluation of wind farm efficiency and wind turbine wakes at the nysted offshore wind farm. *Wind Energy*, 13(6):573–586, 2010.
- [30] Corten G P and Lindenburg P S. Assembly of energy flow collectors, such as windpark, and method of operation, 2007.
- [31] A. Sharma, F. Taghaddosi, and A. Gupta. Diagnosis of aerodynamic losses in the root region of a horizontal axis wind turbine. Niskayuna, New York, 2010. General Electric Internal Report.
- [32] R J Barthelmie, O Rathmann, S T Frandsen, K S Hansen, E Politis, J Prospathopoulos, K Rados, D Cabezn, W Schlez, J Phillips, A Neubert, J G Schepers, and S P van der Pijl. Modelling and measurements of wakes in large wind farms. *Journal of Physics: Conference Series*, 75(1), 2007.
- [33] D. Mackay. *Sustainable Energy without the hot air*. UIT Cambridge Ltd., 2008.
- [34] S. N. Jung, T. S. No, and K. W. Ryu. Aerodynamic performance prediction of a 30kw counter-rotating wind turbine system. *Renewable Energy*, 30(5):631–644, 2005.

- [35] S. Lee, H. Kim, and S. Lee. Analysis of aerodynamic characteristics on a counter-rotating wind turbine. *Current Applied Physics*, 10:339–342, 2010.
- [36] S. Lee, E. Kim, H. Son, and S. Lee. Effects of design parameters on aerodynamic performance of a counter-rotating wind turbine. *Renewable Energy*, 42:140–144, 2012.
- [37] P. S. Kumar, A. Abraham, R. J. Bensingh, and S. Ilangovan. Computational and experimental analysis of a counter-rotating wind turbine system. *Journal of Scientific & Industrial Research*, 72(5):300–306, 2013.
- [38] A. Wobben. Wind power installation with two rotors in tandem, 2006. US Patent 7,074,011 B1.
- [39] S. Goldstein. On the Vortex Theory of Screw Propellers. *Proceedings of the Royal Society A: Mathematical, Physical and Engineering Sciences*, 123(792):440–465, April 1929.
- [40] T. Burton, D. Sharpe, N. Jenkins, and E. Bossanyi. *Wind Energy Handbook*. John Wiley & Sons Ltd., 2002.
- [41] J. F. Ainslie. Calculating the flow field in the wake of wind turbines. *Journal of Wind Engineering and Industrial Aerodynamics*, 27:213–224, 1988.
- [42] H. Snel. Review of Aerodynamics for Wind Turbines. *Wind Energy*, 6:203–211, 2003.
- [43] Jens Norkær Sorensen and Wen Zhong Shen. Numerical modeling of wind turbine wakes. *Journal of fluids engineering*, 124(2):393–399, 2002.
- [44] Y. Wu and F. Porté-Agel. Large-eddy simulation of wind-turbine wakes: Evaluation of turbine parametrisations. *Boundary-Layer Meteorology*, 138(3), 2011.
- [45] J. Smagorinsky. General circulation experiments with the primitive equations i. the basic experiment. *Monthly Weather Review*, 91, 1963.
- [46] M. Selig. Propid user manual, 2012.
- [47] M. Selig and J. L. Tangler. Development and application of a multipoint inverse design method for horizontal axis wind turbines. *Wind Engineering*, 19(2), 1995.

- [48] Jason Mark Jonkman, Sandy Butterfield, Walter Musial, and G Scott. *Definition of a 5-MW reference wind turbine for offshore system development*. National Renewable Energy Laboratory Golden, CO, 2009.
- [49] Behnam Moghadassian, Aaron Rosenberg, and Anupam Sharma. Numerical investigation of aerodynamic performance and loads of a novel dual rotor wind turbine. *Energies*, 9(7):571, 2016.
- [50] Chin-Hoh Moeng. A large-eddy-simulation model for the study of planetary boundary-layer turbulence. *Journal of the Atmospheric Sciences*, 41(13):2052–2062, 1984.
- [51] World Meteorological Organization. *Guide to meteorological instruments and methods of observation*. Secretariat of the World Meteorological Organization, 1983.
- [52] Lars Davidson. Hybrid les-rans: Inlet boundary conditions for flows with recirculation. In *Advances in Hybrid RANS-LES Modelling*, pages 55–66. Springer, 2008.
- [53] Raúl Bayoán Cal, José Lebrón, Luciano Castillo, Hyung Suk Kang, and Charles Meneveau. Experimental study of the horizontally averaged flow structure in a model wind-turbine array boundary layer. *Journal of Renewable and Sustainable Energy*, 2(1):013106, 2010.
- [54] Yu-Ting Wu and Fernando Porté-Agel. Large-eddy simulation of wind-turbine wakes: evaluation of turbine parametrisations. *Boundary-layer meteorology*, 138(3):345–366, 2011.
- [55] Aaron Rosenberg and Anupam Sharma. A prescribed-wake vortex lattice method for preliminary design of co-axial, dual-rotor wind turbines. *Journal of Solar Energy Engineering*, 138(6):061002, 2016.
- [56] Zhenyu Wang, Ahmet Ozbay, Wei Tian, Anupam Sharma, and Hui Hu. An experimental investigation on the wake characteristics behind a novel twin-rotor wind turbine. 2015.
- [57] Ahmet Ozbay, Wei Tian, and Hui Hu. An experimental investigation on the aeromechanics and near wake characteristics of dual-rotor wind turbines (drwts). In *32nd ASME wind energy symposium, AIAA SciTech, National Harbor, Maryland*, pages 13–17, 2014.

- [58] Seungmin Lee, Hogeon Kim, Eunkuk Son, and Soogab Lee. Effects of design parameters on aerodynamic performance of a counter-rotating wind turbine. *Renewable Energy*, 42:140–144, 2012.
- [59] Seungmin Lee, Eunkuk Son, and Soogab Lee. Velocity interference in the rear rotor of a counter-rotating wind turbine. *Renewable energy*, 54:235–240, 2013.
- [60] D Kocurek. Lifting surface performance analysis for horizontal wind axis turbines. *Solar Energy Research Institute, SERI/STR-217-3163*, 1987.
- [61] Jean-Jacques Chattot. Design and analysis of wind turbines using helicoidal vortex model. *Computational Fluid Dynamics Journal*, 11(1):50–54, 2002.
- [62] J Gordon Leishman. Aerodynamics of horizontal axis wind turbines. In *Advances in Wind Energy Conversion Technology*, pages 1–69. Springer, 2011.
- [63] Jean-Jacques Chattot. Optimization of propellers using helicoidal vortex model. *Computational Fluid Dynamics Journal*, 10(4):429–438, 2002.
- [64] Jean-Jacques Chattot. Wind turbine aerodynamics: analysis and design. *International Journal of Aerodynamics*, 1(3-4):404–444, 2011.
- [65] Marshall L Buhl et al. *A new empirical relationship between thrust coefficient and induction factor for the turbulent windmill state*. National Renewable Energy Laboratory Golden, CO, 2005.
- [66] Andrew Thelen, Leifur Leifsson, Anupam Sharma, and Slawomir Koziel. Direct and surrogate-based optimization of dual-rotor wind turbines. In *34th Wind Energy Symposium*, page 1265, 2016.
- [67] BE Launder and BI Sharma. Application of the energy-dissipation model of turbulence to the calculation of flow near a spinning disc. *Letters in heat and mass transfer*, 1(2):131–137, 1974.

- [68] Suganthi Selvaraj and Anupam Sharma. On predicting the phenomenon of surface flow convergence in wind farms. In *ASME Turbo Expo 2014: Turbine Technical Conference and Exposition*, pages V03BT46A004–V03BT46A004. American Society of Mechanical Engineers, 2014.
- [69] Ahmet Ozbay, Wei Tian, and Hui Hu. Experimental investigation on the wake characteristics and aeromechanics of dual-rotor wind turbines. *Journal of Engineering for Gas Turbines and Power*, 138(4):042602, 2016.
- [70] Seongkyu Lee. Inverse design of horizontal axis wind turbine blades using a vortex line method. *Wind Energy*, 18(2):253–266, 2015.
- [71] Leonardo P Chamorro and Fernando Porté-Agel. A wind-tunnel investigation of wind-turbine wakes: boundary-layer turbulence effects. *Boundary-layer meteorology*, 132(1):129–149, 2009.
- [72] H. Hu, Z. F. Yang, and P. Sarkar. Dynamic wind loads and wake characteristics of a wind turbine model in an atmospheric boundary layer wind. *Experiments in Fluids*, 52(5):1277–1294, 2012.
- [73] Rebecca Jane Barthelmie, SC Pryor, Sten Tronæs Frandsen, Kurt Schaldemose Hansen, JG Schepers, K Rados, W Schlez, A Neubert, LE Jensen, and S Neckelmann. Quantifying the impact of wind turbine wakes on power output at offshore wind farms. *Journal of Atmospheric and Oceanic Technology*, 27(8):1302–1317, 2010.
- [74] G. P. Corten and P. S. Lindenburg. Assembly of energy flow collectors, such as windpark, and method of operation, 2007. US Patent 7299627 B2.
- [75] Andrew Kusiak and Zhe Song. Design of wind farm layout for maximum wind energy capture. *Renewable Energy*, 35(3):685–694, 2010.
- [76] F. Wan and F. Porté-Agel. Large-eddy simulation of stably-stratified flow over a steep hill. *Boundary-Layer Meteorology*, 138(3):367–384, 2011.

- [77] Luis A Martinez, Stefano Leonardi, Matthew J Churchfield, and Patrick J Moriarty. A comparison of actuator disk and actuator line wind turbine models and best practices for their use. *AIAA Paper*, (2012-0900), 2012.